UNDERSTANDING CONSTRAINTS ON GEOTHERMAL SUSTAINABILITY THROUGH RESERVOIR CHARACTERIZATION AT BRADY GEOTHERMAL FIELD, NEVADA

by

Jeremy R. Patterson

A thesis submitted in partial fulfillment of

the requirements for the degree of

Master of Science

(Geoscience)

at the

UNIVERSITY OF WISCONSIN - MADISON

2018

ABSTRACT

The vast supply of geothermal energy stored throughout the Earth and the exceedingly long time required to dissipate that energy makes the world's geothermal energy supply nearly limitless. As such, this resource holds the potential to provide a large supply of the world's energy demands; however, like all natural resources, it must be utilized in an appropriate manner if it is to be sustainable. Understanding sustainable use of geothermal resources requires thorough characterization efforts aimed at better understanding subsurface properties. The goal of this work is to understand which critical subsurface properties exert the most influence on sustainable geothermal production as a means to provide targeted future resource characterization strategies.

Borehole temperature and reservoir pressure data were analyzed to estimate reservoir thermal and hydraulic properties at an active geothermal site. These reservoir properties then served as inputs for an analytical model which simulated net power production over a 30-year period. The analytical model was used to conduct a sensitivity analysis to determine which parameters were most critical in constraining the sustainability of a geothermal reservoir. Modeling results reveal that the number of preferential flow pathways (i.e. fractures) used for heat transport provides the greatest impact on geothermal reservoir sustainability. These results suggest that early and pre-production geothermal reservoir exploration would achieve the greatest benefit from characterization strategies which seek to delineate the number of active flow pathways present in the system.

ACKNOWLEDGEMENTS

I would like to start by thanking my advisor, Dr. Michael Cardiff, for his continuous support throughout the completion of this project. I owe the success of this project to his guidance, patience, and thoughtful detailed feedback. I also owe a debt of gratitude to the other members of my guidance and evaluation committee, Dr. Jean Bahr and Dr. Cliff Thurber. Both have been very unselfish with their time and advice, and as such were critical to the successful completion of this project.

I would like to express my gratitude to Dr. Kurt Feigl for welcoming me into the PoroTomo research group here at UW-Madison and giving me the opportunity to participate in this very interesting research. I would also like to thank the entire PoroTomo team for engaging and informative conversations during my time here. This research project would not be possible without the extensive field effort put forth by this team in 2016, and for that I am grateful.

I would like to express my thanks to the University of Wisconsin – Madison Department of Geosciences, and National Science Foundation for providing the funding which has allowed me to participate in this research. The Department of Geoscience funded my first two semesters and the last two semesters were funded by the National Science Foundation.

Finally, I would like to thank my friends and family who have without fail supported my ongoing educational pursuits. My parents have constantly encouraged and inspired me to achieve bigger and better pursuits, for which I am grateful. My dear friend Nikki has been an unwavering pillar of support and has provided constant encouragement to achieve greatness. Lastly, to Laura, Catherine, and the rest of the hydrogeology

research group I say thank you for listening to multiple iterations of rehearsal talks and putting up with my random mid-morning office rambling sessions.

TABLE OF CONTENTS

Page

LIST OF TABLES

Table Page

LIST OF FIGURES

Figure Page

CHAPTER 1

INTRODUCTION

1.1. Purpose and Scope

One estimate of heat content within the Earth due to decay of radioactive isotopes is 10^{13} EJ (1 EJ = 10^{18} J), an amount that would require approximately 10^{9} years to dissipate purely through ground heat flux [*Rybach and Mongillo*, 2006]. Given the vast quantity of heat energy stored within the Earth and the time frame required to dissipate that energy, geothermal energy is essentially unlimited in supply. Current predictions estimate that geothermal energy production has the potential to reach 100 GW with improvements in subsurface exploration and production technologies [*GTO*, 2016].

Despite the widespread nature of thermal energy throughout the Earth, geothermal energy production is limited to locations where geologic settings favor a steep geothermal gradient such as Iceland, the Basin and Range Province of the western U.S., and New Zealand just to name a few. Construction of geothermal power plants is a high-risk financial endeavor whose success relies heavily on understanding local subsurface energy and materials prior to well siting and plant construction.

Geothermal energy has the capacity to provide an important contribution to meeting worldwide energy needs; however, as described above resource development is an inherently high-risk endeavor requiring large capital investment and possibility of substantial capital loss. Given these factors, multiple research efforts are being conducted aimed at improving subsurface characterization prior to geothermal development. The

work presented in this thesis seeks to address improved subsurface characterization during early production time frames by evaluating data from an active geothermal field and conducting a sensitivity analysis to understand which reservoir properties exert the greatest influence on reservoir sustainability on multi-decadal time scales.

1.2. Thesis Objectives and Organization

The objectives of this thesis are to use borehole temperature data to characterize reservoir thermal properties and borehole pressure data to characterize reservoir hydraulic properties at an active geothermal field and illustrate how these characterization efforts can be used to constrain future reservoir performance using simple analytical modeling techniques.

The remainder of this thesis is organized as follows. Chapter 2 discusses geothermal operations and the geologic setting at the Brady geothermal field (henceforth "Brady") and the integrated PoroTomo field experiment conducted during March, 2016. Chapter 3 investigates thermal properties of the Brady reservoir by using transient borehole temperatures (following injection of a cold water "slug") to estimate reservoir thermal diffusivity with depth along the borehole. Chapter 4 analyzes reservoir pressure measurements obtained during changes in site operations at Brady and uses hydrologic modeling to estimate the hydraulic conductivity within different geologic units, applying multiple conceptual models. Chapters 3 and 4 represent practical efforts to constrain reservoir properties at a geothermal site that has been operating for several decades where thermal sustainability is becoming a relevant question. That said, geothermal

sustainability is a practical consideration at many geothermal reservoirs where limited characterization data availability is common. In Chapter 5, I discuss a simple approach using analytical models to examine the likely thermal, and thus financial, sustainability of a geothermal reservoir given limited characterization information.

1.3. Geothermal Sustainability

An important distinction to make when discussing renewable energy is the difference between renewability and sustainability. In a general sense renewability refers to the nature of a resource, whereas sustainability refers to the way in which a resource is utilized. Geothermal systems are renewable resources provided that water extracted for energy production is returned to the subsurface through injection wells to be reheated. In contrast, fluid, and thus heat, extraction rates dictate the sustainability of geothermal systems. Sustainable energy production requires that heat extraction be no greater than the local geothermal heat flux or the reservoir will cool over time and eventually reduce the amount of energy available for extraction.

Sustainability as a term within the context of renewable energy development first evolved in 1987, defined as energy development that meets present energy needs without compromising future energy needs [*Gro Harlem Brundtland et al.*, 1987]. *Axelsson et al.* [2005] offers an updated sustainability definition with respect to geothermal systems, equating sustainability as an energy production level at which the reservoir is able to replenish itself and a constant rate of production can be maintained for 100 – 300 years. As geothermal heat flux varies widely across continents, this sustainable rate is not

generalizable, requiring initial characterization efforts and early production data [*Axelsson*, 2010].

The above definition proposed by *Axelsson* [2010] is useful in that it provides a quantifiable metric on a timescale that is relatable to society; however, it is limited in that it considers only the thermal sustainability of a geothermal reservoir and does not imply economic sustainability, which is typically considered on much shorter scales of 20 – 30 years.

When simultaneously considering the economic and thermal sustainability of geothermal reservoirs, it is generally accepted that geothermal development benefits from economies of scale. *Lovekin* [2000] demonstrated that when considering differing production strategies, a sustainable low production rate provides a smaller discounted return on investment when compared with a more aggressive high production rate, diminishing with time in response to reservoir cooling and depressurization. In essence, this suggests that the most profitable production strategy likely could be the least sustainable.

This thesis seeks to understand the effects thermal and hydraulic properties have on controlling reservoir thermal sustainability on the time scales considered from an economic perspective. This work also seeks to address larger sustainability modeling questions, such as identifying the most important factors controlling long-term reservoir behavior, and the most important information to be collected during early development stages to help reduce long term prediction uncertainty [*Axelsson*, 2010; *Rybach and Mongillo*, 2006].

1.4. Modeling Geothermal Systems

Current geothermal plant design relies heavily on the use of numerical simulations to understand groundwater flow and heat transport behavior in a reservoir under certain production conditions [*Franco and Vaccaro*, 2014]. However, numerical simulations are a recent development in modeling practices as improvement in computer technology has decreased the computation time of these highly complex numerical models.

Initial geothermal modeling efforts focused on analytical solutions, requiring significantly less computational power. One such early solution developed by *Bodvarsson* [1972] arose in response to the beginning of geothermal water re-injection after heat removal in the late 1960's. This solution determines the radius of influence surrounding injection wells, providing plant operators with a tool to help determine the minimum safe distance at which production wells should be placed to minimize thermal "contamination" by cooled water re-injection [*Bodvarsson*, 1972]. While this analytical expression proved useful for understanding the effects of re-injection in a geothermal setting, like all analytical solutions it is subject to limitations. The main limitation suffered by this solution is that it was developed for intragranular (i.e. porous media) groundwater flow systems, which is an uncommon flow regime in geothermal settings as many deep geothermal reservoirs are dominated by flow through fractured media. Another limitation is that the expression yields a symmetric radius of influence and does not account for preferential flow that would enhance the radius of influence along a

specific direction allowing “thermal contamination” in areas where it was not predicted to occur.

While the *Bodvarsson* [1972] solution proved useful for geothermal reservoirs dominated by porous media flow, groundwater flow – and thus heat transport – in most deep geothermal systems is likely dominated by fractures. To account for this limitation, *Bödvarsson and Tsang* [1982] developed an analytical solution that simulates thermal front movement in a radial direction away from an injection well through horizontal fractures. In contrast to the *Bodvarsson* [1972] solution, this analytical expression provided a tool allowing plant operators to determine if a particular reservoir geometry would experience thermal breakthrough of injection waters at production wells in a given time period under specified operating conditions.

In contrast to the *Bödvarsson and Tsang* [1982] solution, *Gringarten et al.* [1975] developed an analytical solution simulating thermal front movement through vertically oriented fractures in a geothermal system that formed in response to reservoir enhancement techniques (i.e., hydraulic fracturing). The two solutions are similar in that they both consider infinitely extending fractures and treat the reservoir as impermeable, allowing water to move only through fractures. Both solutions also prevent heat conduction parallel to fracture orientation so that heat conduction occurs along a thermal gradient from the reservoir orthogonally into the cold water-bearing fractures. The solution developed by *Gringarten et al.* [1975] differs in that it conceptualizes planar flow along individual fractures between well doublets, whereas the *Bödvarsson and Tsang* [1982] conceptualizes flow in a purely radial manner away from an injection well.

As analytical solutions require a number of assumptions and physical simplifications, the three solutions discussed above represent end member conceptualizations of groundwater flow in geothermal systems. *Bodvarsson* [1972] considers flow to be occurring through a porous media with no preferential flow paths while *Bödvarsson and Tsang* [1982] and *Gringarten et al.* [1975] allow flow to occur only in fractures, neglecting porous media flow throughout the reservoir. The physical reality in real-world geothermal reservoirs exists on a continuum between these end member simplifications. Unfortunately, deriving simplified analytical solutions for conditions that exist at other points along this continuum is not a trivial task.

Numerical modeling addresses many limitations suffered by analytical solutions designed to model geothermal systems. First, numerical codes address the points along the continuum that exist between pure porous media and pure fracture flow by allowing dual continuum domains that include both fracture and porous media flow. Numerical methods also allow for greater complexity in production and injection wells, both with the number and geometry of wells, compared with their analytical counterparts and can, in principle, implement arbitrarily complex geometries for subsurface geologic units and fracture networks.

Like analytical models, numerical models are also subject to limitations. Numerical models are subject to a concept commonly known as garbage in – garbage out, meaning that predictive simulations are only as good as the input used to inform them [*Franco and Vaccaro*, 2014]. Avoiding garbage in – garbage out requires a thorough understanding of the system when building numerical models, as predictive simulations can produce results that appear numerically stable but are not physically realistic or

consistent with the system being represented. As numerical models are tools built to address specific questions or test hypotheses, they are also subject to interpretation if the modeler asks questions that a specific model is not designed to answer.

The most common approach to numerically modeling geothermal systems relies on software packages and/or codes that couple groundwater and heat flow, such as the TOUGH family of software. *Franco and Vaccaro* [2014] present a thorough review of geothermal simulations conducted using current modeling software. Reviewed modeling efforts are predominantly conducted using TOUGH to simulate temperature and pressure changes in large geothermal systems throughout the world.

While numerical modeling with TOUGH or other software is perhaps more physically accurate and dominates geothermal systems modeling efforts, multiple studies illustrate the utility of the simpler analytical solutions. Iceland hosts the Hamar geothermal system, which is a low temperature geothermal system used for heat production in a nearby town since 1969. *Axelsson et al.* [2005] used a lumped parameter model to study the sustainability of this system and used the analytical solution developed *Bodvarsson* [1972] to simulate thermal breakthrough of injected water. Using this simple analytical model, the study found that the sustainable energy production at this particular field was controlled by total energy content of the resource as well as the areal extent of the reservoir.

With increasing interest in enhanced geothermal systems (EGS), *Li et al.* [2016] conducted a sensitivity analysis to understand how multi-stage EGS design affects the financial performance of a synthetic geothermal reservoir over a set period of 30 years. The investigators used the analytical solution for vertically fractured systems developed

by *Gringarten et al.* [1975] to simulate thermal breakthrough at production wells due to cold water injection, which is used to determine power production and income potential. Using this analytical modeling approach, they reported that the number of stages had the largest effects on net present value, and closer well bore spacings allowed for greater transmissivity and maximum mass flow rates through stimulated fractures.

This thesis seeks to use a mix of analytical and numerical modeling approaches to understand reservoir properties and sustainability. I will use numerical modeling approaches to estimate thermal and hydraulic properties of the geothermal reservoir at Brady and explore their uncertainty. Estimated properties will be used as inputs for a simple analytical model designed to simulate geothermal power production through time. These power production simulations, which use basic characterization data to understand the thermal and financial sustainability of a geothermal reservoir under specified production conditions, are then examined to prioritize data collection efforts in pre-production and/or early production geothermal investigations.

CHAPTER 2

STUDY AREA

The Basin and Range province of the western United States contains a large number of geothermal fields, many of which lie along normal fault zones showing evidence of recent activity [*Faulds et al.*, 2010a]. Temperatures throughout these geothermal fields are often observed to be as high as 200°C, which accounts for the 290 MWe installed capacity across fifteen power plants in this region [*Faulds et al.*, 2010b]. Recent research cites ongoing regional extension and structural controls allowing for high heat and fluid flows to the surface in the absence of recent volcanism. Given the high temperatures observed throughout the region and structural controls channeling hot fluids into bounded regions, the Basin and Range province is the focus of ongoing geothermal development and research improving geothermal technologies.

This chapter discusses geothermal power production at an active geothermal power plant in this region, the geologic and structural setting, and an extensive field experiment conducted during March 2016 with the goal of testing an integrated technology to improve reservoir property characterization.

2.1. Brady Geothermal Power Plant

The Brady geothermal field – henceforth referred to as Brady – is located approximately 75 km NE of Reno, NV along the northern edge of the Hot Springs Mountains [*Faulds et al.*, 2010a]. Exploration and assessment for geothermal energy

potential at Brady dates back as early as the 1950's. Geothermal production at Brady first began in the late 1970's when the field powered an onion dehydration plant, the world's first geothermal food processing plant. However, commercial geothermal production at Brady did not begin until 1991 when a dual flash power plant was installed with a 21 MWe production capacity [*Ettinger and Brugman*, 1992]. Early production at Brady saw premature breakthrough of re-injected water and decreasing production potential. In response, a binary energy extraction unit was added in 2002, increasing total installed capacity to 26.1 MWe, which is the current operating configuration [*Faulds et al.*, 2010a; *Krieger and Sponsler*, 2002].

Figure 1 shows an overhead map of the Brady geothermal field, with an inset map provided to locate the geothermal field within Nevada. Production wells, represented as red discs, located in the SW portion of Brady, pump hot water from depths of 1000 – 1500 m below land surface (bls) for energy production (Figure 1). Injection wells, represented as blue discs, located in the NE portion of Brady, re-inject cold water, following heat removal, at depths of 150 – 200 m bls (Figure 1). Not all water removed for production is re-injected at the NE portion of the field. A very small portion of the water is sent off-site to a nearby onion dehydration planted while a separate portion is re-injected about 2 km SE of the power plant. Abandoned production and injection wells throughout the field now function as observation wells. The yellow circle represents an observation well used to collect borehole temperature data, and the purple circles represent observation wells used to collect reservoir pressure throughout the PoroTomo field experiment.

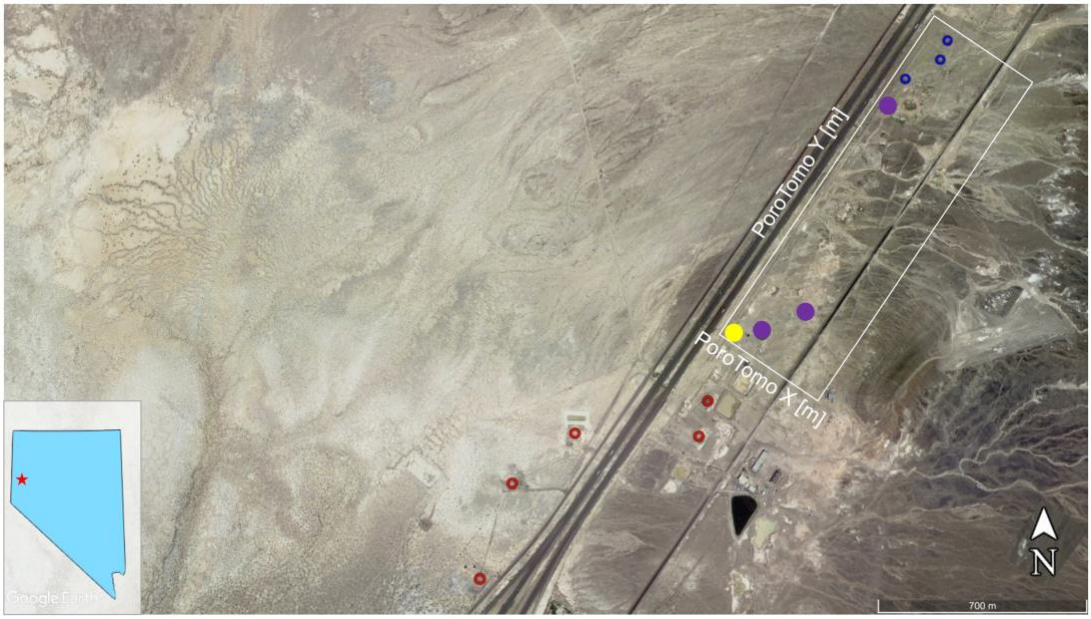

Figure 1:Satellite imagery showing Brady Geothermal Fieldnear Reno, NV. The white box indicates the study area, red discs represents production wells, blue discs represent injection wells.

2.2. Geologic Setting

The geologic setting at Brady is highly complex, with multiple faults trending primarily NE – SW throughout the reservoir, offsetting identified geologic units. Figure 2 shows a cross-section through the Brady reservoir orthogonal to dominant fault trends showing the complex fault geometry. The remainder of this section will focus on describing the lithologic setting, structural setting, and hydrologic interpretation at Brady.

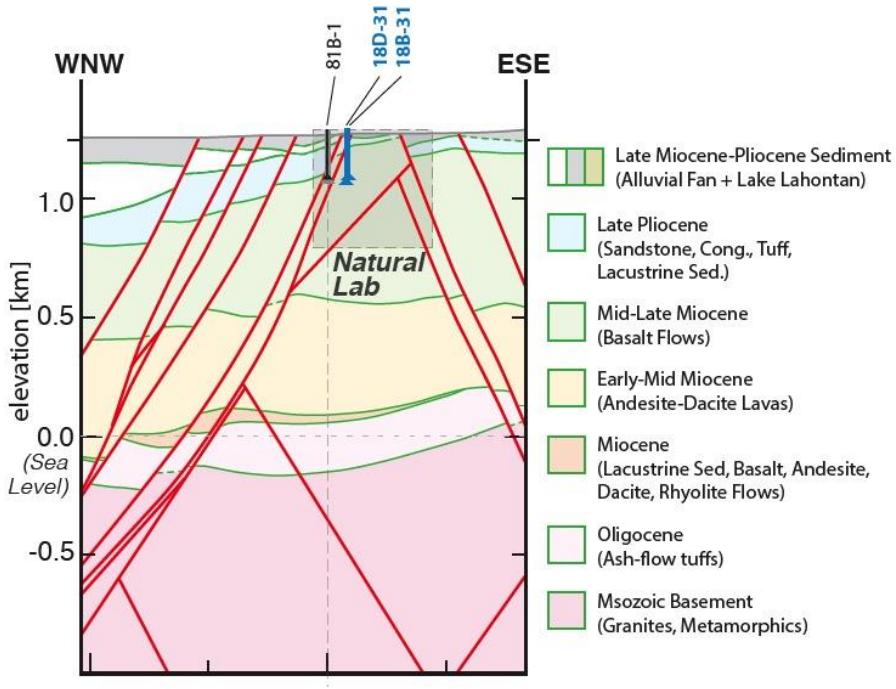

Figure 2: Strike-normal cross-section through Brady showing identified lithologic units and faults. Figure created by Nick Davatzes and S. Tabrez Ali based on geologic model by Jolie et al. [2015].

2.2.1. Lithologic Setting

Alluvial fan deposits in the western area at Brady dominate the Quaternary unconsolidated sediments with a maximum thickness of 75 m. Silicified sands, sinter pots, and colluvium comprise smaller Quaternary unconsolidated sediments in the eastern area of Brady. Quaternary sediments are underlain by Late Miocene tuffaceous deposits, sandstones, and conglomerates with a maximum thickness of 350 m. These units lie in contact with Late Miocene aged interbedded lacustrine sedimentary deposits and limestones with a maximum thickness of 400 m. Lacustrine deposits represent lumped lithologies including siltstones, sandstones, and diatomite [*Jolie et al.*, 2015].

Middle to Late Miocene interlayered aphanitic basalt flows, rhyolite lava flows, and porphyritic dacites to rhyodacite flows with maximum thickness of 800 m underlie

interbedded lacustrine and limestone deposits. Brecciation, believed to be the result of hydrothermal alteration, is noted throughout these lithologies. Early to Middle Miocene andesite to dacite lavas with a maximum thickness of 600 m underlie interlayered Middle Miocene lava flows, representing the transition from clastic sedimentary lithologies to volcanic lithologies. Oligocene ash-flow tuffs with a maximum thickness of 650 m underlie andesite – dacite lavas and lie unconformably on top of undifferentiated Mesozoic crystalline basement rocks [*Jolie et al.,* 2015].

2.2.2. Structural Setting

The Basin and Range Province of the western United States is characterized by W-NW extensional stress, which field evidence suggests is still ongoing. Trending NE-SW through central Nevada is the Humboldt Structural Zone, one of many groups of NE trending fault belts hosting a concentration of geothermal activity within the Basin and Range Province, primarily along major fault zones [*Faulds et al.*, 2010a].

Brady is located at the edge of the Humboldt Structural Zone with an orientation orthogonal to regional extension. The major structural feature within Brady geothermal field is the Brady Fault Zone, a NNE trending fault zone approximately 10 km in length that dips steeply to the NW [*Faulds et al.*, 2010c; *Jolie et al.*, 2015]. The Brady power plant is located within a prominent fault step over within the Brady Fault Zone. The step over is characterized by a series of en échelon faults connecting the larger fault step. These en échelon faults follow the NNE trend of the Brady fault zone, and are dominantly steeply dipping to the NW; however as seen in Figure 2 a subset of these faults dip to the SE. The high concentration of faults in this area concentrates the

geothermal activity within the fault step and serves as the target for installed production wells at Brady power plant [*Faulds et al.*, 2010c; *Jolie et al.*, 2015].

2.2.3. Hydrogeologic Interpretation

Unconsolidated sediments and clastic sedimentary units represent potential major water bearing units containing primary porosity and secondary porosity features (i.e., faults and fractures). Well 81B-1 indicates water levels are located approximately 100 ft below land surface, which corresponds with late sandstone and lacustrine units, though it is unclear if these units are the primary source of water for this well as the screened interval also encompasses faulted basalt units below. It is unclear if aquifer conditions at this location are confined or confined, as interlayered lacustrine and limestone deposits could serve as local confining units (Figure 2).

Field observations at Brady indicate that hot water at depth within faults and fractures of deeper volcanic units is being channeled to the surface along prominent faults. Faults at Brady oriented orthogonal to regional extension are subject to dilation, potentially enhancing fault-parallel fluid flow. The presence of fumaroles, sinter pots, and warm ground along a 4 km NNE trending zone supports the interpretation of fault-controlled groundwater flow parallel to faults in the reservoir [*Faulds et al.*, 2010b].

While field evidence suggests that major faults act as conduits to flow parallel to the fault surface, it is unclear whether the same holds for flow normal to the fault surface as the necessary water level data are not available. As discussed in *Bense et al.* [2013], if faults are acting as conduits normal to the fault surfaces, consistent water levels would be observed on either side of the fault; however, if faults are acting as barriers to flow

normal to the fault surface, a precipitous drop in water levels would be seen on the down gradient side of the fault [*Bense et al.*, 2013]. Groundwater flow along and across faults remains an open question at Brady.

2.3. PoroTomo Integrated Experiment

During an 18-day period in March 2016, an extensive field experiment was conducted to assess the ability of an integrated technology (using datasets from hydrology, geodesy, and seismology) to characterize the mechanical properties at an active geothermal reservoir. The volume of reservoir to be characterized – referred to as Brady Natural Lab – is 500 m in the NW-SE direction, 1500 m in the NE-SW direction, and 400 m in depth. The white rectangle seen in Figure 1 represents the footprint of the Brady Natural Lab, indicating the surface expression of the volume of interest.

The PoroTomo experiment was conducted in four stages designed to monitor reservoir response to changing hydrologic stresses. Figure 3 shows the stages of the field experiment as well as the timing and duration of each experimental stage. Each stage stressed the reservoir in a different way and assessed reservoir response by monitoring borehole pressure in three observation wells, borehole and ground surface temperatures, ambient seismic noise, high accuracy GPS elevations, and by conducting active seismic surveys. This field effort resulted in the most comprehensive pressure, temperature, and seismic datasets available at an active geothermal field that the PoroTomo team is aware of.

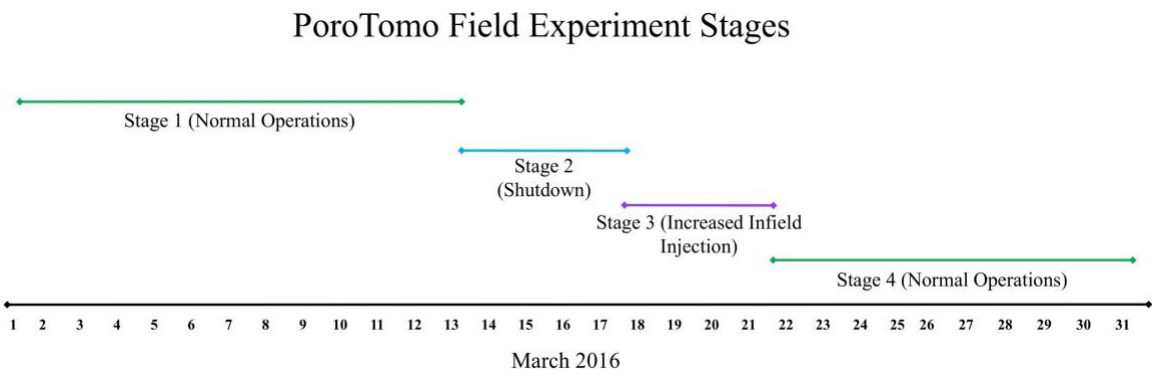

Figure 3: Gantt diagram showing experiment stages, timing, and duration of the PoroTomo field experiment.

Stage one collected data under normal operating conditions. This dataset provides an understanding of reservoir response under steady state hydrologic conditions. Similar to stage one, stage four collected under normal operating conditions; however, unlike stage one, stage four recorded the reservoir response as it returned to steady state after various applied hydrologic stresses.

Stage two of the field experiment collected data during power plant shutdown. In coordination with plant operators, all energy production was ceased at Brady, which included the cessation of pumping and injecting water. Data collected during this stage monitors reservoir response as fluid pressures dissipate in the northern portion of Brady as fluid injection ceases and fluid pressures increase in the southern portion of Brady as fluid extraction ceases.

Under normal operating conditions, a portion of the water used for energy production is sent approximately two kilometers offsite for subsurface re-injection. Stage three of the PoroTomo field experiment changes this water diversion and re-injects all water removed from the reservoir back into the injection wells at the northern portion of the geothermal field. Stage three also differs from normal operating conditions in that

injection rates are not constant with time. During this stage, fluid injection rates are systematically increased and decreased in a periodic manner.

CHAPTER 3

THERMAL CHARACTERIZATION

The text that follows is presented as published in *The Leading Edge* copyright owned by Society of Exploration Geophysics (SEG) [*Patterson et al.*, 2017].

Abstract

Distributed temperature sensing (DTS) systems provide near real-time data collection that captures borehole spatiotemporal temperature dynamics. Temperature data were collected in an observation well at an active geothermal site for a period of 8 days under geothermal production conditions. Collected temperature data showcases the ability of DTS systems to detect changes to the location of steam-water interface, visualize borehole temperature recovery – following injection of a cold water "slug" – and identify anomalously warm and/or cool zones. The high sampling rate and spatial resolution of DTS data also shows borehole temperature dynamics that are not captured by traditional pressure-temperature survey tools. Inversion of thermal recovery data using a finite-difference heat transfer model produces a thermal diffusivity profile that is consistent with laboratory measured values and correlates with identified lithologic changes within the borehole. Used alone or in conjunction with complementary data sets, DTS systems are a useful tool for developing a better understanding of both reservoir rock thermal properties as well as within and near-borehole fluid movement.

3.1. Introduction

Understanding the temperature profile in geothermal boreholes is a first step in determining thermal properties immediately surrounding the borehole. Thermal characterization of geothermal reservoirs is a critical component of decision making and predictive modeling of reservoir production potential. Temperature is considered one of the most critical state variables of a reservoir as it directly influences production potential and informs decisions regarding well installation depth, casing length, and other operational considerations . In addition, understanding changes to pressures or water levels in wells over time can help to assess hydraulic connectivity between different reservoir intervals.

Plant managers commonly monitor average temperature of pumped water at production and injection wellheads. In addition, vertical logs of temperature variability are commonly collected by pressure-temperature (P-T) survey, which involves lowering and raising a temperature probe through the borehole and recording temperature and pressure at specified depth intervals. Temperature logs provide power plant operators with a snapshot of the temperature profile at discrete times, requiring multiple P-T surveys be conducted at regular intervals in an effort to understand reservoir temperature evolution under normal operating conditions.

Fiber-optic distributed temperature sensing (DTS) is a well-established monitoring technology in the hydrologic sciences. Following successful studies demonstrating the use of DTS in identifying and/or quantifying groundwater-surface water exchanges, researchers have adopted this tool to gain a better understanding of

borehole hydrogeology. *Bense et al.* [2016] conducted a thorough review of shallow borehole studies using DTS systems to better understand borehole groundwater dynamics. *Read et al.* [2013] and *Leaf et al.* [2012] used DTS in open boreholes to determine areas of fracture flow by using heat as a tracer through thermal dilution testing. *Read et al.* [2015] and *Sellwood et al.* [2015] used DTS in conjunction with a point heating element to determine vertical velocities within open boreholes. While previous studies have focused on flow within open boreholes, *Coleman et al.* [2015] used DTS to determine fracture flow within lined boreholes under natural-gradient conditions. *Freifeld et al.* [2008] illustrated the use of borehole DTS to determine thermal conductivity of permafrost immediately surrounding the borehole. They utilized an electrical heating element in the borehole to create a temperature transient which was analyzed during inversion to determine thermal conductivity.

Despite the numerous studies illustrating the use of DTS in open boreholes, there is limited literature surrounding its use in a geothermal setting. As an example, *Sakaguchi and Matsushima* [2000] demonstrated the use of DTS to determine the location of fractures within boreholes using cold water injection at an active geothermal site. *Ikeda et al.* [2000] used DTS during well completion at a geothermal site to monitor borehole temperature recovery after drilling completion and vertical flow profiling. These prior two studies limited data analysis to qualitative interpretations of individual snapshots from borehole temperature profiles. We are unaware of any existing peer-reviewed studies in the literature that illustrate the capability of DTS to show natural borehole dynamics or investigate its usage in a geothermal setting in a quantitative manner.

In this study, we demonstrate the utility of installing fiber-optic DTS systems in an observation borehole at an active geothermal power plant. We illustrate the ability of DTS to capture spatiotemporal dynamics during borehole temperature recovery following injection of a cold-water slug. Last, we develop a numerical heat transfer model which is used to estimate variability in reservoir thermal diffusivity (i.e., the ratio of thermal conductivity to volumetric heat capacity) of reservoir rock near the observation well using a simple parameter estimation approach. Our inversion strategy is a modified version of the methodology employed by *Freifeld et al.* [2008], where the temperature within the borehole is perturbed from equilibrium. We then use the temperature recovery to estimate a depth profile of thermal diffusivity in 1 m increments throughout the cased and fluid-filled portion of the borehole. Our methodology differs in that we do not use electrical current to initiate the temperature change. Instead, we use a cold-water slug to decrease the borehole temperature and prompt heat diffusion from the reservoir into the borehole.

3.1.1. Study Area

Brady Geothermal Field – henceforth referred to simply as "Brady" – is a geothermal field located near Fernley, Nevada, US, within the Basin and Range Province. It is located on the Brady fault zone which is a prominent NNE-striking normal fault system approximately 4 km in length. Production wells access the reservoir up to depths of approximately 2 km in a prominent fault step-over with a high density of faulting, as seen in Figure 4. Re-injection wells access the subsurface at much shallower depths of 100 – 200 m, and are separated from production wells by approximately 2 km across the

land surface [*Feigl and PoroTomo Team*, 2017; *Siler et al.*, 2016]. During the PoroTomo field experiment in March 2016, several wells that were no longer used for production were used as observation wells to record borehole pressures and temperatures [*Feigl and PoroTomo Team*, 2017].

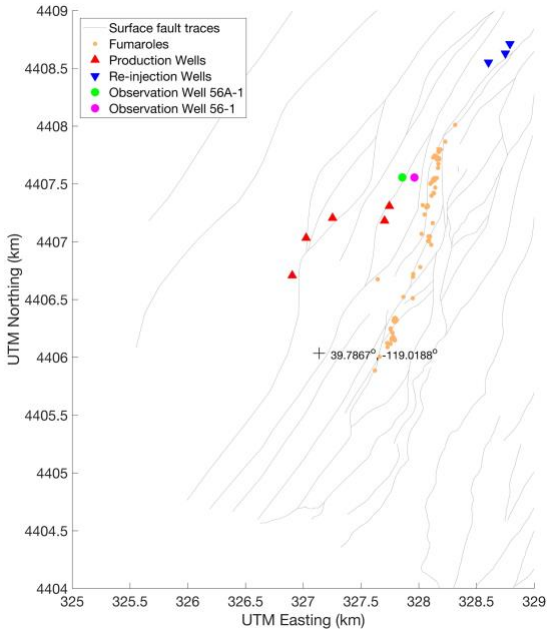

Figure 4: Plan view map of Brady Geothermal Field near Fernley, Nevada. Identified fiducial point represents location of site well 15-12.

A well schematic for Brady observation well 56-1, the primary well examined in this study, shows lithology with depth, casing diameter, screened interval, water level, temperature depth profile, and prominent faults detected during drilling (Figure 5). This schematic is based on a compilation of well construction reports, lithology maps from current geologic models for Brady, and measurements obtained during P-T surveys of the well. The lithologic profile is based on current 3D geologic and structural modeling and is representative of the lithology seen throughout the geothermal field [*Siler et al.*, 2016]. The surficial geology is dominated by alluvial fans composed primarily of volcanic

sediments. Deeper lithologies are composed of undifferentiated lacustrine units, limestones, and crystalline basement rocks composed of basalts and andesites [*Siler et al.*, 2016]. Fluid flow through the reservoir is assumed to be-fault-dominated since these rocks have low permeability and several fumaroles are oriented parallel to the Brady fault system [*Feigl and PoroTomo Team*, 2017; *Siler et al.*, 2016]. The fault system channels fluids from the shallow aquifer to the deeper reservoir [*Ali et al.*, 2016].

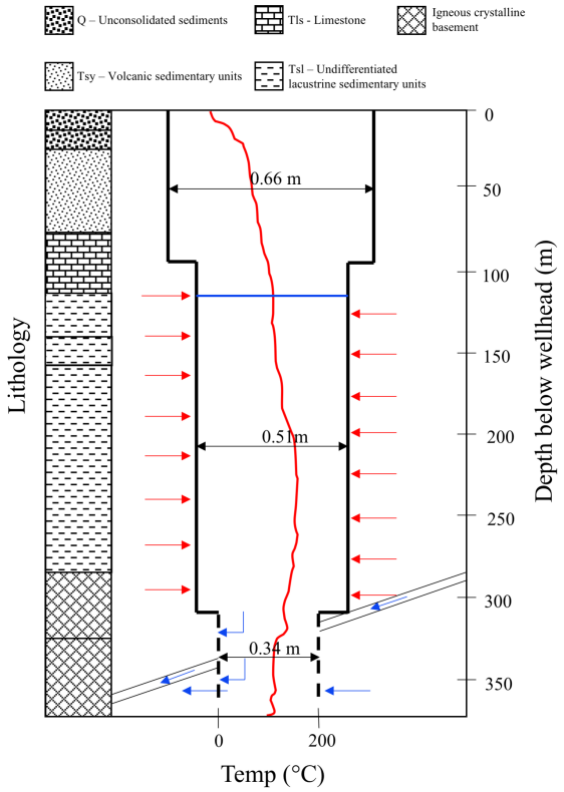

Figure 5: Brady observation well 56-1 construction, lithology, and pre-DTS installation observations. Well construction information provided by ORMAT, Inc. Lithology based on a current geologic model [Siler et al., 2016]. Temperature profile (red line) based on initial P-T survey. Arrows indicate conceptual model for heat diffusion (red arrows) and water movement (blue arrows). Water level in well is approximately 120 m below wellhead (blue line).

3.2. Methods

The DTS data described in this work is one portion of data collected during the DOE-funded "PoroTomo" field experiment, a collaborative effort between UW-Madison and several other institutions, designed to test integrated technologies for characterizing critical properties of geothermal reservoirs [*Feigl and PoroTomo Team*, 2017]. The PoroTomo integrated field experiment follows from earlier observations of subsidence and surface deformation at Brady [*Ali et al.,* 2016] and was conducted over a period of 4 weeks during March 2016. The PoroTomo team collected geophysical and hydrologic data to characterize rock properties in a 500m x 1500m x 400m volume at a 50 m resolution at Brady [*Feigl and PoroTomo Team*, 2017]. The field experiment consists of four stages based on plant operations: (1) Normal plant operations; (2) Full plant shutdown; (3) Increased infield injection; and (4) Resumption of normal plant operations (Figure 6). During each stage of the experiment, the reservoir was monitored by a combination of active and ambient seismic instrumentation (nodal seismometers and distributed acoustic sensing), InSAR satellite passes, dynamic GPS measurements, surface and borehole DTS, and pressure sensors installed in observation wells. This combined instrumentation strategy was designed to monitor the thermal, pressure, and deformation response of the reservoir during changes to site operations. In this paper, we focus solely on individual analysis of the borehole DTS data, which is available at the Geothermal Data Repository [*Coleman*, 2016].

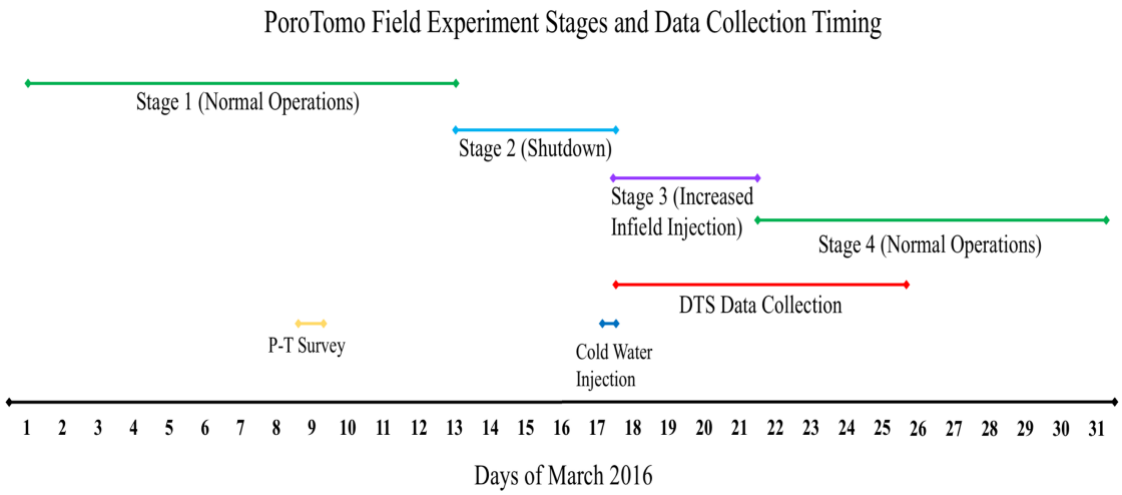

Figure 6: Gantt chart showing stages and timing of the integrated PoroTomo field experiment, period of DTS data collection, date of cold-water slug injection, and date of previous P-T survey.

3.2.1. DTS Installation

We used fiber-optic DTS to monitor temperature changes in observation well 56-1 for a period of 8 days during Stages 3 and 4 of the PoroTomo field experiment. The DTS system deployed at Brady uses Raman optical backscatter technology and the Stokes / Anti-Stokes ratio, which is based on photon excitation, to determine distance and temperature, respectively, along the cable. [*Bense et al.*, 2016]. This study used a high-resolution ULTIMA-S^{TM} DTS (Silixa Ltd., Elstree, United Kingdom) with temperature determined using a double-ended calibration configuration. We use an external calibration bath to further refine temperature offset effects. A full discussion of the Raman backscatter theory and DTS configuration is well documented in the literature and is beyond the scope of this study [*Bense et al.*, 2016].

We used the following process to install the DTS cable. First, for safety reasons, the well was cooled by injection of a 15 m^3 slug of cold water into well 56-1. This cold-water slug was injected into well 56-1 on March 17, 2016 at approximately 16:00 UTC.

Following this, the DTS cable was immediately inserted into the well, to a depth of 372 m below the wellhead. We then connected the cable to a DTS interrogator at the land surface, and began monitoring shortly thereafter. DTS cable installation required approximately 3 hours, and data collection in well 56-1 began on March 17, 2016 23:25 UTC. Borehole temperature recovery was recorded in near-real-time with a temporal sampling interval of 60 s. The DTS system collected data every 0.126 m along the cable with an instrument resolution of 0.29 m. We averaged the collected temperature data to 1 m bins for data analysis and inversion.

3.2.2. Data Quality Verification

The DTS cable installed in this work used a double-ended configuration, which allowed two measurements of temperature to be collected at each observation location. Co-located measurements of temperature by DTS showed little variability with an average difference of less than 0.5 ˚C, suggesting high accuracy. As another measure of data quality, Figure 7 shows temperature logs for well 56-1 as measured by P-T survey prior to DTS installation and a temperature profile measured by DTS during the final day of site monitoring. DTS and P-T survey data show very similar trends in the temperature with depth but, there is a noticeable difference in the recorded temperatures. Since the DTS data shows somewhat cooler temperatures than the P-T survey, we infer that the borehole had not yet achieved equilibrium following cold-water slug injection. We also note the effect of thermal inertia on the P-T survey tool, with the up-going measurements showing consistently higher temperatures than the down-going measurements, suggesting a high degree of uncertainty in the measurements collected with this tool.

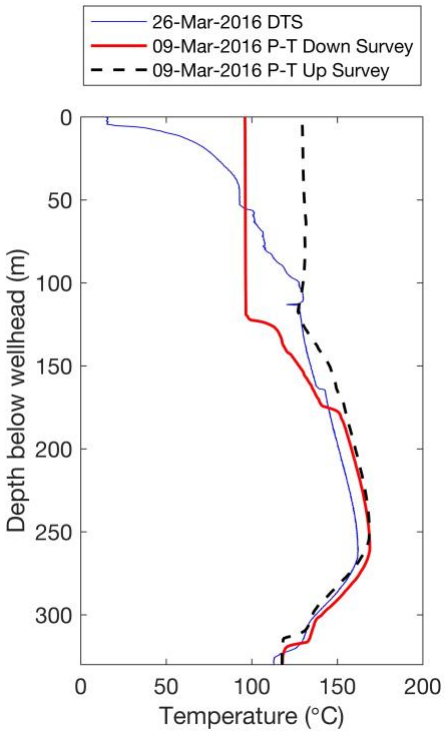

Figure 7: Temperature log in observation well 56-1 at Brady comparing the data provided by traditional logging tools (P-T survey) and DTS systems. The temperature log given by the DTS shows identical temperature trends when compared to traditional logging method methods. Difference between down-going and up-going P-T survey illustrates the effect of thermal inertia on this tool.

3.3. Data Analysis / Interpretation

3.3.1. Borehole / Reservoir Flow

DTS records the borehole temperature recovery as a function of time and depth, as seen in Figure 8, for a period of 8 days following cold-water injection. We observe maximum borehole temperatures of approximately 160˚C centered near 265 m depth, with an isothermal zone approximately 50 m in thickness (Figure 8). The average geothermal gradient through the fluid-filled portion of the borehole (starting at ~ 125 m depth) to the maximum temperature zone is 0.23 ˚C /m. Borehole cooling begins at

approximately 265 m, with an average geothermal gradient of -0.78 ˚C/m, over a thickness of approximately 60 m (i.e. ~325 m depth), where a stable cool zone exists to a depth of 372 m. The negative gradient observed below 265 m, which would not be expected under natural conditions, likely represents host rock cooling surrounding a dominant flow path, where heat is being extracted for active geothermal production within the Brady reservoir.

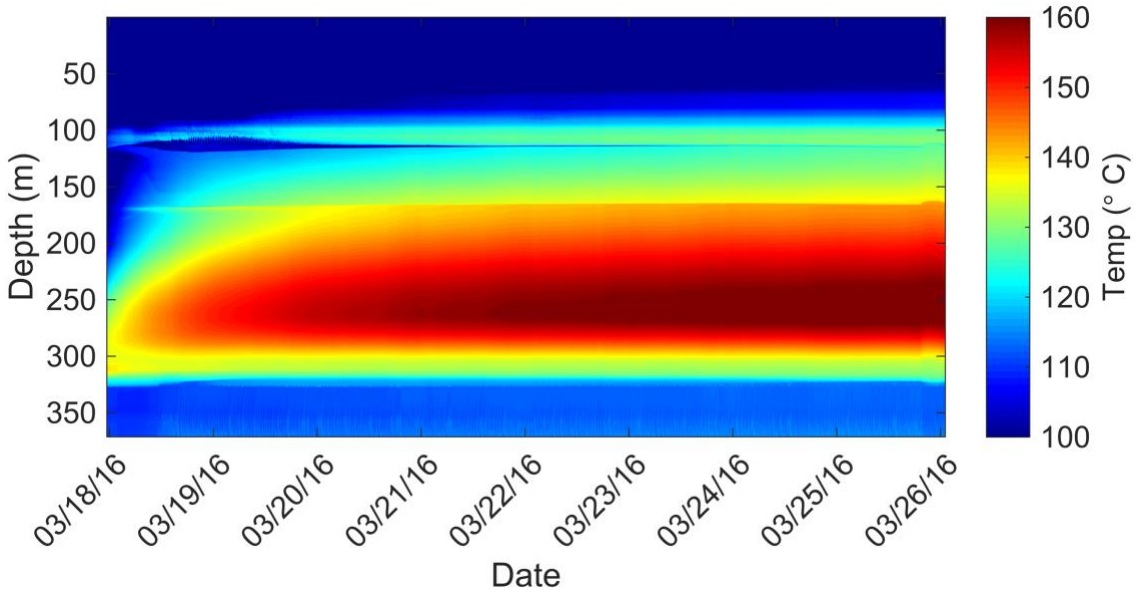

Figure 8: Depth profile temperature time series showing borehole temperature recovery following a cold-water slug injection into well 56-1. A maximum temperature zone approximately 50 m in thickness is centered at 250 m depth. An inverse temperature gradient begins at approximately 275 m terminating in a persistent cold zone below approximately 325 m depth.

The temperature data provide further evidence for a dominant flow path near the bottom of well 56-1. The P-T survey before DTS cable installation clearly shows increases in temperature and pressure gradients, associated with being below water, at about 120 m depth. Without flow into the formation, we expect a 15 m^3 slug of water into well 56-1 to produce an initial water level change of approximately 52 m in the borehole, based on casing radii from the well construction. However, DTS data collected

approximately 7 hours after slug injection show no evidence of an elevated water level. Since the well is cased down to approximately 310 m depth, we infer that most or all water added to 56-1 exited the borehole below 310 m depth over a period of 7 hours, implying a high-permeability zone (possibly associated with driller-designated fault zones) below this depth. Despite the expected change in water level, the water slug clearly cooled the borehole. We interpret temperature evolution to be thermal diffusion as heat flows from the hot rock towards the cool borehole, with temperature recovery measured by DTS (Figure 8).

DTS data clearly capture temperature variations over time scales on the order of an hour in well 56-1 during the borehole temperature recovery. We observe pulses in temperature starting at approximately 350 m depth and moving to a depth of 372 m. Figure 9b shows the increased temperature pulses which began at approximately 11:30 UTC on March 18, 2017, about 11 hours after the beginning of Stage 3 and the resumption of pumping operations at Brady. The pulses occur approximately every 30 minutes and are consistently 10 minutes in duration. Converting the temperature log time series into an animation, (supplementary material) we also note pulses of decreased temperature in the animation at a depth of 120 m moving to the top of the borehole (Figure 9a). The decreased temperature pulses are first observed at approximately 14:30 UTC roughly 14 hours after pumping resumed at Brady. DTS data also shows a sharp temperature contrast at 115 m, which is interpreted to be the water level, with the abrupt temperature change at this level being the result of latent heat effects at the steam-water interface. This temperature contrast continues to decline in elevation throughout the time series (Figure 9a). This decline mirrors water level changes measured by a pressure

sensor in monitoring well 56A-1, which is separated by a horizontal distance of 50 m and drilled to a similar depth as well 56-1; therefore, we infer that these wells are hydraulically connected.

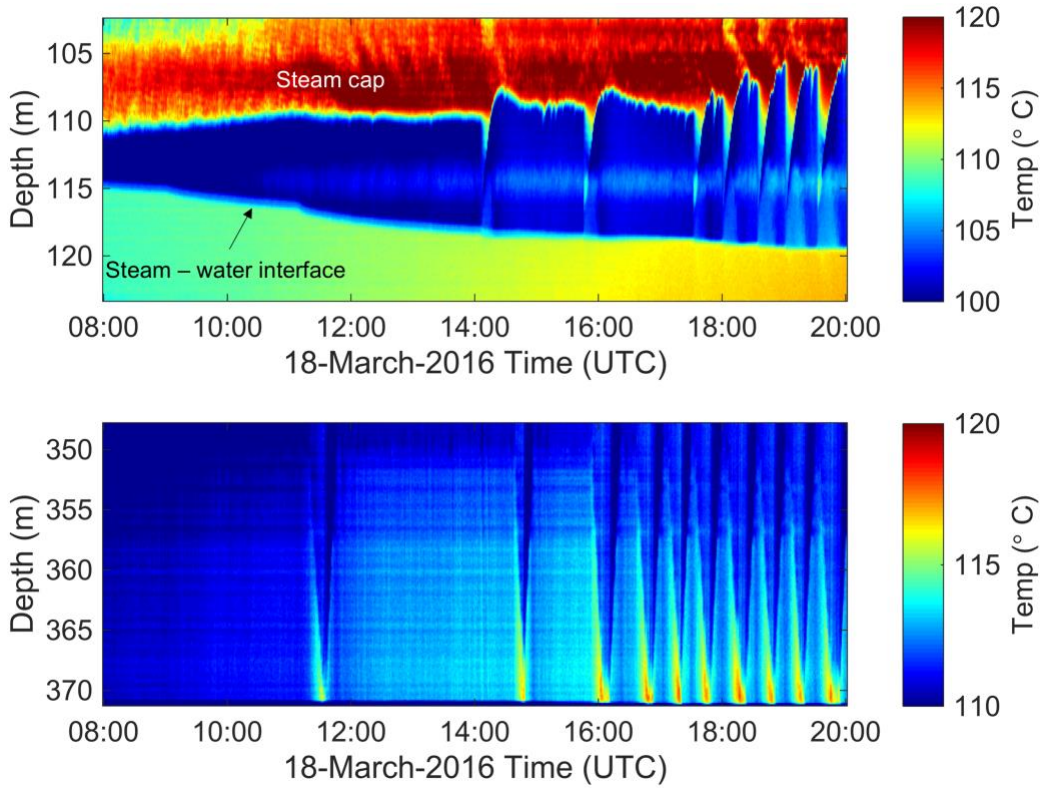

Figure 9: 12-hour time series collected March 18, 2016. (a) The steam – water interface increases in depth with increasing time. The onset of phase change at the interface occurs as water level decreases resulting in depressurization. (b) The first evidence of forced convection into the open interval below 350 m depth is seen approximately 11 hours after the onset of pumping with evolution of periodic convection pulses occurring at 30-minute intervals.

We interpret the pulsing described above through the following mechanism. After pumping resumed at Brady, the pressure at the screened end of well 56-1 dropped, resulting in flow of water out of the cased well into the formation. This loss of water resulted in a drop of the water level in the well, de-compressing the trapped steam column above 115 m and promoting further boiling. Pulses of water lost out of the bottom of the well thus may have produced pulses of pressure changes, causing further

flashing of water to steam. This decompression boiling behavior and observed oscillating temperature signal is very similar to observations of decompression-related geyser eruption as discussed in a recent review of geyser eruption mechanics [*Hurwitz and Manga*, 2017].

The outflow of water out of the bottom of the borehole represents the only apparent exchange of water with the surrounding formation. However, changes in temperature within the cased section of the borehole (from ~130 m to 300 m below the wellhead) are clearly apparent throughout the experiment. The borehole overall is heated throughout the period of March 18 – March 26 as the borehole equilibrates with the surrounding hot reservoir rock. The strong temperature gradient between the borehole itself and the surrounding reservoir rock implies that most heat transfer is in the radial direction towards the borehole due to thermal diffusion. In the next analysis, we make the simplifying assumption that thermal diffusion in the radial dimension represents the dominant process within the cased borehole interval, and we use a numerical model to analyze the amount of heat diffusion at different depths within the borehole. The assumption of limited heat movement within the borehole (as would be caused by convection and forced advection) is revisited based on the analysis results.

3.3.2. Heat Diffusion (Cased Borehole)

To interpret the DTS data, we develop a numerical heat-transfer model to simulate temperature evolution within the borehole. We then use this model during inversion to estimate the depth profile of reservoir thermal diffusivity throughout the

fluid-filled and cased portion of well 56-1 (130 – 300 m depth). The 1-D radial heat-transfer model uses a finite-difference approach – center-difference in space and implicit time-stepping – to balance heat fluxes across individual finite-difference cells. A constant-temperature boundary condition is placed 2 m from the borehole center, and a zero-flux boundary condition is placed at the center of the borehole. Initial temperature is specified for fluid within the borehole. A representative value of thermal diffusivity for water (1.45×10^{-6} m^2/s) is selected to represent borehole fluid. The model assumes that heat transfer through forced and natural convection is small relative to heat diffusion and can be ignored. The model also assumes that most heat flow is occurring in a radially symmetric manner towards the borehole walls due to the large temperature gradients between the cooled borehole and warmer surrounding host rock. Similarly, the model assumes no vertical heat flow within the borehole or the reservoir. Fourier's Law of Heat Conduction is used as the basis to build a linear system of heat flow equations. We formulate and then solve the system of equations implicitly using MATLAB's direct matrix solver.

Using the described model, we invert for host rock thermal diffusivity by minimizing misfit between modeled and observed data for each 1 m interval individually. The estimated parameters include: thermal diffusivity and initial temperature at each borehole depth independently in 1 m increments throughout the fluid-filled and cased portion of the borehole (130 m – 300 m below wellhead), with no *a priori* information or regularization applied. We use the entire time series for each depth (11,235 data points per depth) with a direct-search optimization based on the Nelder-Mead simplex algorithm

to minimize the sum of the squared residuals and determine the optimal thermal diffusivity estimates.

3.3.3. Heat Transfer Model and Parameter Estimation

We use the transient DTS data at individual depths to estimate the thermal diffusivity depth profile in well 56-1. The results of the parameter estimation are shown in Figure 10, which includes the depth profile of thermal diffusivity estimates, along with observed data and modeled data fit at the median diffusivity values for each lithology (144 m, 196 m, 293 m). There are two major changes in thermal diffusivity seen in the depth profile, at 158 m and 285 m depth. The diffusivity changes that are seen closely correlate with stratigraphic boundaries defined by geologic modeling [*Siler et al.*, 2016]. In conjunction with the large changes seen at 158 m and 285 m, we observe a trend of consistently decreasing diffusivity estimates starting at 265 m depth, which is the depth at which the inverted thermal gradient originates (Figure 8).

The median diffusivity estimates for each lithologic zone are 1.12×10^{-8} m^2/s at 143 m depth, 1.13×10^{-8} m^2/s at 196 m depth, and 4.61×10^{-9} m^2/s at 293 m depth (Figure 10). These values are lower than laboratory-measured values for lacustrine sedimentary rocks (1.3×10^{-6} m^2/s) and basalts (9×10^{-7} m^2/s); however, it is reasonable that the lacustrine sedimentary units have a higher median diffusivity value than that of the crystalline basalts. We hypothesize that the difference in lab-measured and our estimated diffusivity values is due to temperature-dependence. It has been shown that diffusivity decreases with increasing temperature in a non-linear manner, which could explain this discrepancy [*Robertson*, 1988].

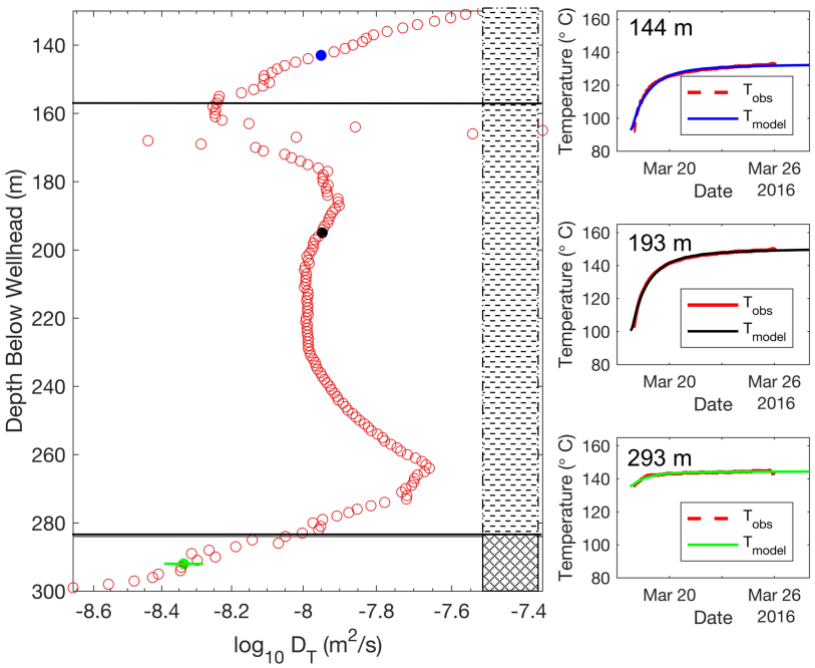

Figure 10: Vertical profile of thermal diffusivity estimates throughout the fluid-filled and cased portion of the Brady observation well. Horizontal black lines represent lithologic contacts identified in geologic modeling efforts by Siler et al. (2016). Modeled data fit shown at representative depths – (a) 144 m (b) 196 m (c) 293 m. Parameter uncertainty increases with depth. Error bars are present for all 3 representative depths but are within circle radii for the upper two locations.

The increasing variability seen at depths below 280 m we attribute to larger uncertainties in the diffusivity estimate. Although we have not conducted a rigorous uncertainty analysis, the 95% confidence interval for the median diffusivity increases with increasing depth. The increasing uncertainty is related to the decreasing temperature range of the fitted data at greater depths within the borehole (Figure 10).

Despite the temperature dynamics occurring at the top and bottom of the borehole as seen in Figure 9, we see no evidence of borehole convection upon detailed inspection of the collected data. The thermal diffusivity estimates obtained support our assertion that radial heat diffusion into the borehole as the dominant heat transfer mechanism due to temperature gradients between the borehole and surrounding reservoir rock. We expect

estimated thermal diffusivity would be higher than reported lab values if other heat transfer mechanisms (e.g. advection) were influencing borehole recovery. One example of this phenomenon occurs at approximately 165 m depth where we observe borehole temperatures recover more quickly compared to surrounding depths (Figure 8). We also note more highly variable diffusivity estimates surrounding this depth, including the highest diffusivity estimates throughout the depth profile (Figure 10). We infer that this signifies heat transfer is occurring through conduction as well as advection, meaning that our effective diffusivity estimates are biased upward. We suspect this is due to a weak section in the casing; however, borehole images are not available to confirm this. We speculate this advection imprint would be seen through a wider range of depths if convective borehole processes or advection within the reservoir was a prominent heat transfer process.

3.4. Conclusion

We have demonstrated the ability of DTS in a geothermal setting to provide data that captures spatiotemporal temperature dynamics in boreholes that are not seen with the more commonly used P-T surveys through the implementation of a thermal response test. As seen in previous studies, this high spatiotemporal resolution can show dynamics that are difficult to capture with other methods, such as the pulsing seen in our study and the associated interesting borehole dynamics related to decreased pressures and steam flashing.

The thermal response test conducted at Brady is different from other thermal response testing in that the temperature perturbation is induced through a cold-water slug

injection to cool the borehole as opposed to using electrical current to warm the borehole. The ability of DTS systems to capture the temperature transients in near real-time allows us to estimate thermal diffusivity throughout the cased and fluid-filled portion of the borehole. Thermal characterization allows us to identify regions in the borehole that are warming more quickly, likely due to advection, which could indicate a weak section in the casing. By comparing thermal diffusivity estimates to established lab values, we conclude that heat conduction is the dominant heat transfer process during borehole recovery at Brady. This information provides useful evidence to site operators, demonstrating that flow and advection within the reservoir appears to be minimal outside of the faulted zones

The information provided by our DTS survey provides a series of conclusions that would be valuable to site operators at geothermal sites, including: (1) geothermal pumping produces water level changes and steam flashing, demonstrating that this well is hydraulically connected to pumping wells; (2) throughout the majority of the borehole, heat appears to be transported only via conduction, suggesting that the sole hydraulic connection between this well and production wells is along faulted intervals; and (3) application of a heat transfer model provides estimates of thermal diffusivity throughout the reservoir, which could be useful for follow-on modeling of reservoir sustainability. This better understanding of both flow pathways and the distribution of thermal diffusivity throughout the reservoir allows plant operators to determine areas of the reservoir which will be the most thermally productive, as well as develop a sense of long term thermal drawdown and financial sustainability of the reservoir.

3.5. Ackowledgements

The authors wish to acknowledge the generous contributions of ORMAT Technologies who provided site access for installation of fiber-optic DTS systems at the Brady Geothermal Field. The authors also acknowledge expertise and thought-provoking questions provided by Doug Miller of Silixa Ltd. Finally, the authors would like to thank Dr. Baishali Roy, Dr. Jonathan Ajo-Franklin, and one anonymous reviewer for thoughtful feedback which greatly improved the quality of this manuscript. This research was supported by grants DE-EE0005510 and DE-EE0006760 from the U.S. Department of Energy Geothermal Technologies Office.

3.6. Addendum

The following sections were not included in *[Patterson et al., 2017]* due to publishing constraints. They are added as an addendum here in the interest of completeness, and to provide a more in-depth description of the heat transfer model and parameter estimation algorithm.

3.6.1. Heat Transfer Model

To conduct the reservoir thermal characterization, I develop a numerical heat transfer model which solves the following boundary value problem:

$$\rho C_p \frac{\partial T}{\partial t} = \frac{1}{r}\frac{\partial}{\partial r}\left(\kappa r \frac{\partial T}{\partial r}\right) \tag{3.1}$$

$$\left.\frac{\partial T}{\partial r}\right|_{r=0} = 0 \tag{3.2}$$

$$T(R,t) = T_{max} \tag{3.3}$$

$$T(r < r_{bore}, 0) = T_{init} \tag{3.4}$$

$$T(r > r_{bore}, 0) = T_{max} \tag{3.5}$$

where

ρ is density [kg / m^3]

C_p is specific heat [J / (kg ℃)]

κ is thermal conductivity [W / (m ℃)]

T is temperature [℃]

r is radial distance [m]

R is the distance to the model boundary [m]

$r_{bore} = 0.255$ m is borehole radius

t is time [s]

I take an energy balance approach to solve the boundary value problem by developing a finite-difference expression that is center-difference in space with implicit time stepping. Using this approach, the temperature flux is determined at each cell-center node using Fourier's Law of Heat Conduction:

$$Q = -\kappa A \frac{\Delta T}{\Delta r} \tag{3.6}$$

Figure 11 shows a typical finite-difference wedge used to develop the heat transfer model. Using this typical wedge, I derive the following energy conservation statement:

$$Q\left(r + \frac{\Delta r}{2}\right) - Q\left(r - \frac{\Delta r}{2}\right) = \frac{T_i^{n+1} - T_i^n}{\Delta t}\, \rho C_p 2\pi \mathrm{r}\Delta \mathrm{r}\Delta \mathrm{z} \tag{3.7}$$

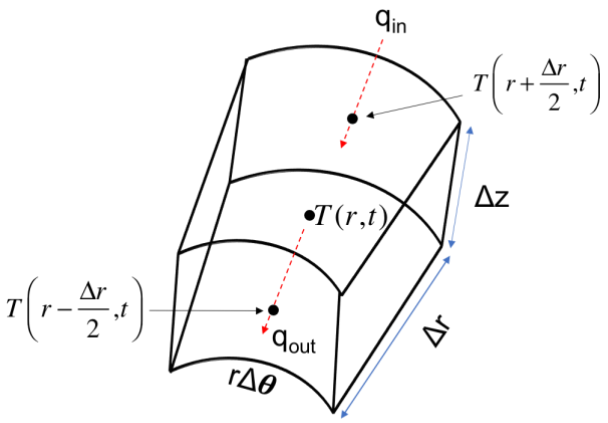

Figure 11: Conceptual diagram showing a typical finite-difference cylindrical wedge.

Substituting (3.6) into (3.7) I develop a system of equations that determines the temperature at discrete points in space and time ($T(r,t)$). Using this substitution, the temperature at any point in space and time is given by:

$$T_i^n = -\left(\alpha \frac{A_{j-1}}{\Delta r_i\, V_i}\right) T_{i-1}^{n+1} + \left(\alpha \frac{A_j}{\Delta r_{i+1} V_i} + \alpha \frac{A_{j-1}}{\Delta r_i\, V_i} + 1\right) T_i^{n+1} - \left(\alpha \frac{A_j}{\Delta r_{i+1} V_i}\right) T_{i+1}^{n+1} \quad (3.8)$$

where

$\alpha = \frac{\kappa\, \Delta t}{\rho\, C_p}$

$V_i = \pi\, (r_{i+1} - r_i)^2 \Delta z$ is finite-difference cell volume [m^3]

$A_j = 2\pi r \Delta z$ is cross-sectional area of individual cell faces [m^2]

Δr_i is the change in radial distance between adjacent cell center nodes [m]

i is finite-difference cell-center node index

j is finite-difference cell face index

Equation 3.8 represents an energy balance for the temperature in the i_{th} cell. When stated for all finite-difference cells, a system of equations is developed and solved to simulate temperature throughout the domain at future time steps using an implicit solution scheme.

The radial discretization used in the finite-difference model allows for higher accuracy near the borehole where the highest magnitude temperature gradients occur by utilizing a telescoping discretization scheme. I calculate the radial discretization as follows [*Anderson et al.*, 2015]:

$$\Delta r_1 = R\frac{\beta - 1}{\beta^n - 1} \text{ for i} = 1 \tag{3.9}$$

$$\Delta r_i = \beta \Delta r_{i-1} \text{ for i} > 1 \tag{3.10}$$

where β is a coefficient that controls the growth rate of the finite-difference cells and n is the number of finite-difference cells. By necessity, β must be greater than 1 for the finite difference cells to grow in size. As β gets large, grid cells closest to the r = 0 m grow smaller, while grid cells closer to $r = R$ grow larger. For the purposes of this thermal characterization, I chose $\beta = 1.05$, $n = 55$, and R = 2 m, which $\Delta r_{min} = 0.4$ cm and $\Delta r_{max} = 9.9$ cm

As is apparent from the governing equations, I invoke a number of reasonable simplifying assumptions to make the finite difference formulation more mathematically tractable. These simplifying assumptions are as follows:

1. Thermal properties of the reservoir rock are homogeneous.
2. There are no external heat sources (i.e. ground heat flux) and/or sinks in the system.

3. The effects of convection and radiation are negligible and can be ignored; therefore, heat transfer from the reservoir into the borehole occurs by diffusion (i.e. conduction) only.
4. Heat transfer occurs only in the radial direction. There is no angular or vertical heat diffusion within the reservoir rock.

3.6.2. Model Validation

Prior to beginning thermal characterization, I compared the finite-difference heat transfer model against a numerical heat diffusion model developed in COMSOL Multiphysics, a very robust and well-validated finite-element, multi-physics numerical modeling software package. The motivation to create a finite-difference heat transfer model as opposed to commercially available software lies in computational efficiency. Heat transfer simulations using COMSOL for this particular model geometry required an average of 90 seconds. In comparison, heat diffusion simulations using the developed finite-difference model are significantly faster requiring an average of 0.2 seconds.

Both models contained identical input parameters and model domain geometry to ensure consistency. Figure 12 compares the results of the two numerical models. The temperature time series shows temperature at r = 0.13 m within the borehole (Figure 12). This accounts for the fact that the DTS cable was not installed exactly in the center of borehole at r = 0 m. While the two models are not an identical fit, they produce very similar results with an RMSE of 0.6°C, which is comparable to the expected data

measurement error. This validation provides the confidence to move forward with thermal characterization using the developed finite-difference heat transfer model.

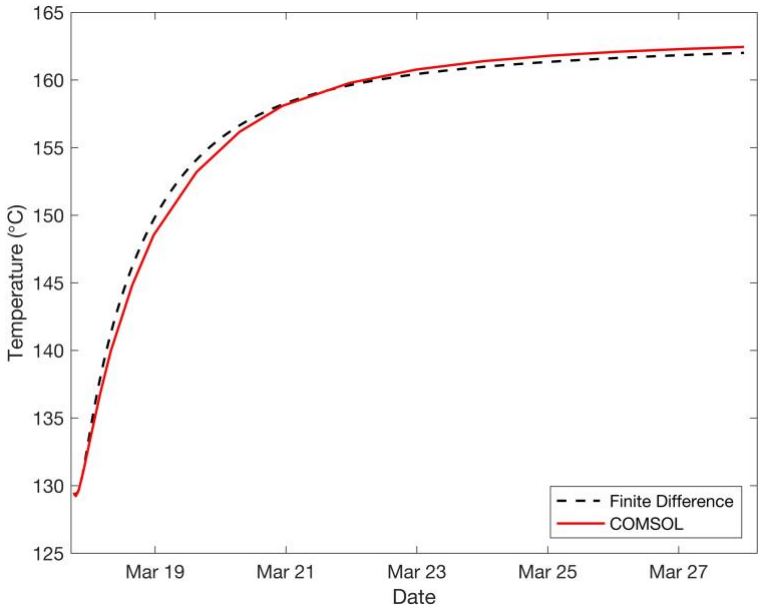

Figure 12: Modeled temperature time series using a finite-difference heat transfer model in comparison with temperature time series using COMSOL Multiphysics. COMSOL fits and the finite difference model produce very similar results, valdiating the developed finite-difference heat transfer model.

3.6.3. Parameter Estimation

Prior to parameter estimation, the data are averaged in to 1 m depth intervals using a simple arithmetic mean. The parameter estimation uses ~ 11,000 data points associated with transient temperature changes at each depth. The objective function that is used to minimize the misfit between the data and model results is [*Aster et al.*, 2011]:

$$\min_{\mathrm{m}} \left|\left|\left(\mathbf{d}-g(\mathbf{m})\right)^{T}\mathbf{R}^{-1}\left(\mathbf{d}-g(\mathbf{m})\right)\right|\right|_{2}^{2} \tag{3.11}$$

where

d is the measured temperature data vector

$g(\mathbf{m})$ is the forward modeled temperature for the vector of current parameters

$\mathbf{R}$ is the expected data collection error matrix

The optimization algorithm uses two convergence criteria to determine that the optimization has successfully converged. The first convergence criterion requires that the maximum change in consecutive natural log parameter values be less than 1×10^{-4}, and the second requires that the minimum difference in the objective function values also be less than 1×10^{-4}. The optimization terminates when both criteria are achieved.

3.6.4. Parameter Uncertainty

To estimate uncertainty bounds on thermal diffusivity estimates, I used a finite-difference linearization to estimate the Jacobian matrix. The linearization approach changes each parameter, individually, by a small amount and then determines the temperature change before and after using the following expression [*Aster et al.*, 2011]:

$$\mathbf{J}(\mathbf{m}) \approx \frac{\mathbf{T}(\mathbf{m}) - \mathbf{T}(\mathbf{m} + \Delta m)}{\Delta m} \tag{3.12}$$

where

$\mathbf{J}(\mathbf{m})$ is the Jacobian approximation with the vector of current parameters

$\mathbf{T}(\mathbf{m})$ is the modeled temperature with the vector of current parameters

$\mathbf{T}(\mathbf{m} + \Delta m)$ is the modeled temperature with one parameter changed by an amount Δm

$\mathbf{m}$ is the vector of current parameters

Δm is the magnitude of change for an individual parameter

Using the Jacobian approximation with optimal parameter estimates, the covariance matrix can be calculated with the expression [*Aster et al.*, 2011]:

$$\mathbf{C} = \left(\mathbf{J}(\mathbf{m})^T \mathbf{R}^{-1} \mathbf{J}(\mathbf{m})\right)^{-1} \tag{3.13}$$

where

$\mathbf{C}$ is the covariance matrix

$\mathbf{R}$ is the expected data measurement error variance matrix

Table 1: Thermal diffusivity 95% confidence intervals determined using linearized uncertainty analysis. Confidence interval depths correspond with highlighted depths in Figure 10.

Depth [m]	D_T Lower Bound [m^2/s]	D_T Estimated [m^2/s]	D_T Upper Bound [m^2/s]
144	1.10×10^{-8}	1.12×10^{-8}	1.15×10^{-8}
196	1.11×10^{-8}	1.13×10^{-8}	1.15×10^{-8}
293	4.05×10^{-9}	4.61×10^{-9}	5.24×10^{-9}

The diagonals of the calculated covariance matrix represent the variance of the error in the parameter estimates. Taking the square root of the diagonal elements gives the standard deviation of the parameter estimates and allows for determining 95% confidence intervals. Table 1 shows the estimated thermal diffusivities and 95% confidence intervals for 144 m, 193 m, and 293 m depth. Parameter uncertainty increases with increasing depth, which is an expected result due to a decreasing difference between T_{init} and T_{max} with increasing depth yielding a temperature recovery curve that can be adequately fit with a wider range of parameters (Figure 10).

The approximated Jacobian matrices provide sensitivity maps, which gives a sense of how each parameter affects borehole temperature through time. Figure 13 shows

the sensitivity maps for $D_T, T_{init},$ and T_{max}, with each parameter increased by 10% above the optimal value, through time. Early time sensitivity is dominated by the initial temperature, which is expected with diffusion being a relatively slow process, as indicated by thermal diffusivity estimates. Intermediate and late time sensitivity is controlled by maximum temperature as diffusion brings borehole water into equilibrium with surrounding reservoir rock. While thermal diffusivity controls the diffusion of heat through the reservoir rock, borehole temperature shows little sensitivity to this parameter when compared to T_{init} and T_{max} (Figure 13).

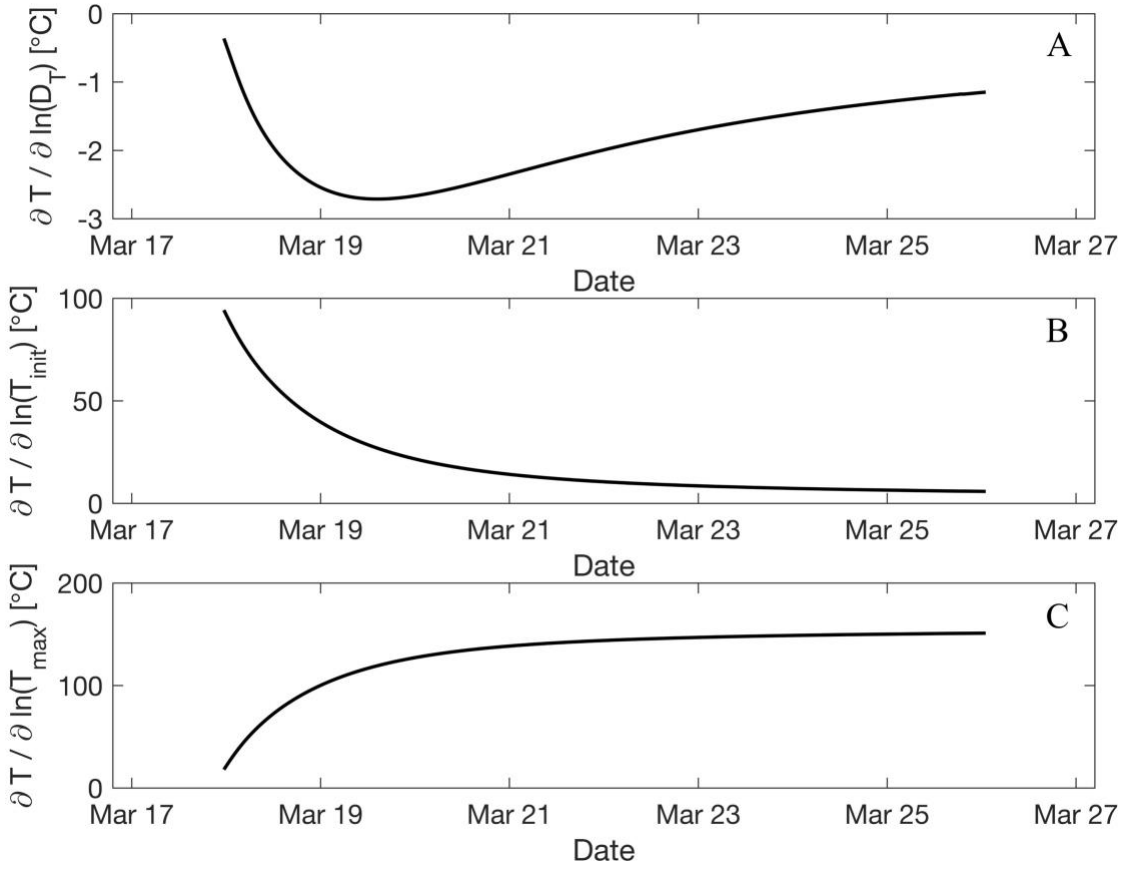

Figure 13: Parameter sensitivity for A) thermal diffusivity, B) initial temperature, and C) maximum temperature at 194 m through time using the linearized Jacobian approximation.

CHAPTER 4

HYDRAULIC CHARACTERIZATION

4.1. Background

Current conceptual understanding of groundwater flow at Brady hypothesizes that water injected at shallow depths follows preferential flow paths along a complex fault network to the deep reservoir where it is reheated and removed by production wells for energy production (Figure 14). Multiple lines of evidence support this conceptual model including observed microseismicity, ground subsidence, and hydrothermal deposits at the land surface.

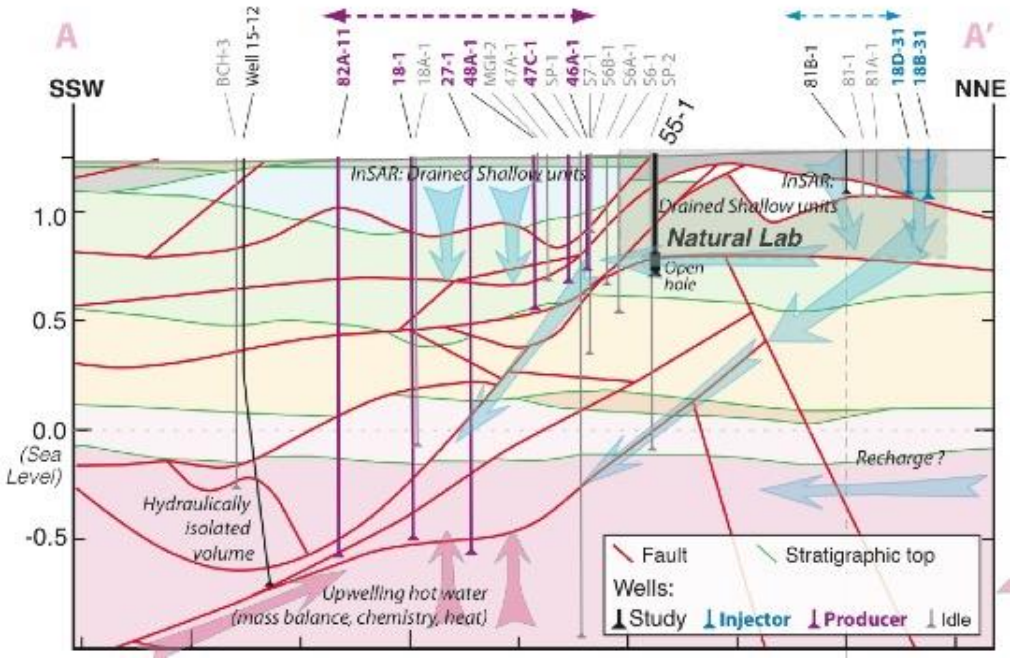

Figure 14: Current groundwater flow conceptual model. Cold water is injected into the shallow reservoir, then moves along a complex fault network to the deeper reservoir to be reheated and removed by production wells. Section line trends SW – NE, paralleling major fault trends at Brady. Adapted from Feigl and PoroTomo Team [2017].

Multiple studies have pointed to microseismic events at Brady as evidence for fault-driven flow through the reservoir [*Cardiff et al.*, 2018; *Davatzes et al.*, 2013; *Laboso and Davatzes*, 2016]. Most recently *Cardiff et al.* [2018] reviewed microseismicity at Brady in a spatial and temporal manner building off the previous work of *Davatzes et al.* [2013]. Temporal analysis indicated most microseismic events occurred during periods when the power plant is not operational and diffusive pressure increases occur in the vicinity of production wells. Spatial analysis shows that microseismic events are occurring in a planar orientation that coincides with known fault geometries throughout the reservoir, as illustrated in Figure 15 [*Cardiff et al.*, 2018]. It is worth noting that these events are all located in the deep reservoir accessed by the production wells, which is characterized by low permeability igneous and metamorphic rock. *Davatzes et al.* [2013] point to a lack of observed microseismicity near the shallower production wells, and attributes this to higher permeability sedimentary units allowing porous media flow in conjunction with preferential flow along faults.

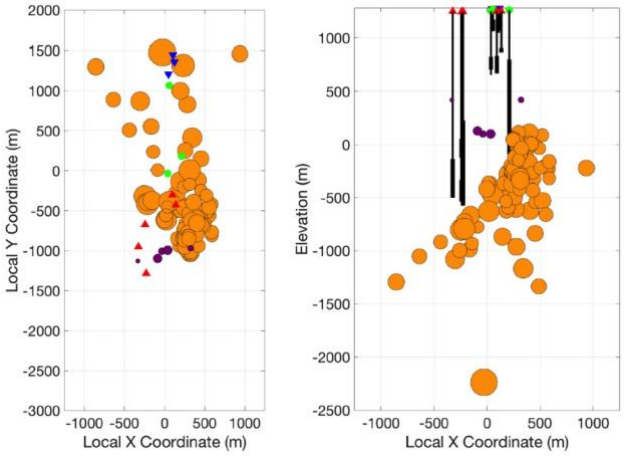

Figure 15: Plan view (left) and cross-sectional view (right) of microseismic events, with location uncertainty < 500 m, recorded at Brady through time. Events follow a planar orientation supporting the hypothesis of fault-driven groundwater flow. Orange circles represent historic seismicity from November 2010 – March 2015[Foxall, 2016], and purple circles represent hypocenters recorded March 2016 during the PoroTomo field experiment. Adapted from Cardiff et al. [2018].

Ground subsidence has been observed at many geothermal fields, including Brady. Proposed mechanisms to explain the subsidence include reservoir thermal contraction as a result of re-injecting cool water, compaction in response to declining pore pressures (or desaturation in some cases) and mineral dissolution. Ground subsidence at Brady has been observed for a period of years, and inverse modeling efforts by *Ali et al.* [2016] indicate that much of the subsidence follows surface fault expressions, with the largest amount of subsidence occurring between the observation and production wells. This subsidence is attributed to thermal contraction as injected water follows subsurface faults to the deeper reservoir [*Ali et al.*, 2016; *Feigl and PoroTomo Team*, 2017].

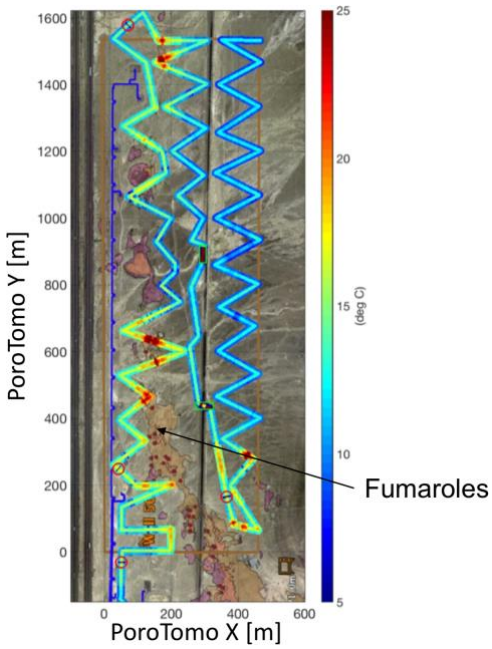

Figure 16: Ground temperature throughout Brady Natural Lab on March 5, 2016 08:32 (UTC), as collected with trenched DTS approximately 1 meter below land surface. Note the presence of increased temperature corresponding with observed hydrothermal deposits. Adapted from Miller et al. [2018].

In conjunction with the presence of observed microseismic activity and land subsidence, hydrothermal deposits are observed at the land surface throughout Brady, including hydrothermal deposits of sinter pots, carbonate tufa, and silicified sediments [*Siler et al.*, 2016]. During the PoroTomo experiment, ground surface temperature data were collected by installing a distributed temperature sensing cable trenched roughly one meter below land surface (Figure 16). The data show multiple areas of high temperature throughout Brady that correlate with observed hydrothermal deposits and surface expressions of faulting.

Despite the physical and geophysical evidence indicating the possibility of a fault-driven groundwater flow system, hydrologic information supporting these observations is limited. To address this limitation, in the remainder of this chapter, I analyze collected pressure data using analytical and numerical models to assess what information can be extracted from this data, henceforth referred to as hydraulic characterization. Hydraulic characterization seeks to use the observed borehole pressure data to estimate the hydraulic conductivity distribution of the geothermal reservoir, proceeding in stages from simpler to more complex conceptual models.

Initial hydraulic characterization efforts focused on analytical parameter estimation and modeling using the Theis solution, which predicts pumping-induced drawdown due to radial flow towards pumping wells [*Theis*, 1935] assuming an infinite 2-dimensional aquifer (e.g. a single permeable faulted zone). Next, we performed hydraulic characterization through numerical modeling using Groundwater Vistas as a graphical user interface, pre-processor, and post-processor for MODFLOW, the finite volume groundwater flow modeling code developed by the U.S. Geological Survey

(USGS). Using MODFLOW with the parameter estimation software PEST, I assessed the consistency of our data with several different conceptual models for flow at Brady.

4.2. Data Collection

Borehole pressure measurements were recorded in three observation wells during the PoroTomo field experiment. The three observation wells, 81B-1, 56A-1, and SP-2, were chosen to provide spatial coverage of the reservoir, and to ensure that collected pressure data show reservoir response to changes in injection and production rates (Figure 4). Table 2 shows observation well location, screened interval elevations, and pressure sensor elevations in the rotated PoroTomo coordinate system. Data coverage is somewhat more limited than may be desired; however, this dataset nonetheless represents to my knowledge the most complete publicly available dataset from an operating geothermal field.

Table 2: Locations, screened interval depths, and sensor elevations for wells throughout the Brady geothermal field. Locations are provided in UTM Zone 11S coordinate system and rotated PoroTomo coordinate systems. Rotated coordinates are rotated -36.4219° about the point [327850.812, 4407606.21].

Injection Wells							
Well	UTM Easting [m]	UTM Northing [m]	PoroTomo X [m]	PoroTomo Y [m]	Screen Top Depth [m]	Screen Bottom Depth [m]	Sensor Elevation [m]
18B-31	328789.55	4408711.47	99.146	1446.7	119.97	231.04	-
18D-31	328750.14	4408629.76	115.95	1357.6	97.08	200.1	-
73-25	328181.33	4401656.23	3798.6	-4591.5	119.48	186.53	-
81A-1	328604.53	4408551.68	45.138	1208.3	119.78	212.14	-
81-1	328562.04	4408507.26	37.321	1147.3	88.3	223.63	-
Production Wells							
Well	Easting [UTM]	Northing [UTM]	PoroTomo X [m]	PoroTomo Y [m]	Screen Top Depth [m]	Screen Bottom Depth [m]	Sensor Elevation [m]
18-1	327024.73	4407032.58	-324.14	-952.04	1383.04	1746.51	-
27-1	327254.25	4407205.19	-241.94	-676.88	1187.5	1777.59	-
47C-1	327745.26	4407308.58	91.773	-302.16	412.4	578.51	-
48A-1	327703.86	4407181.58	133.86	-428.93	343.21	381.61	-
82A-11	326904.91	4406708.46	-228.12	-1284	1014.98	1818.43	-
Observation Wells							
Well	Easting [UTM]	Northing [UTM]	PoroTomo X [m]	PoroTomo Y [m]	Screen Top Depth [m]	Screen Bottom Depth [m]	Sensor Elevation [m]
56A-1	327857.74	4407556.31	35.199	-36.036	422.61	543.51	1014.51
81B-1	328527.01	4408432.02	53.806	1066	99.67	204.52	1093.65
SP-2	328126.29	4407627.97	208.75	181.07	457.51	1351.79	1022.71
56-1	327961.92	4407555.35	119.6	25.046	309.07	726.03	-

4.2.1. Instrumentation and Data Processing

Well 56A-1 was instrumented with a Kuster K10 Quartz borehole temperature and pressure recorder with a reported measurement error of ±7 kPa (Figure 4). Wells 81B-1 and SP-2 utilized Madgetech Capillary Tube Level "cap tube" pressure sensors (Figure 4). These pressure sensors are installed at the land surface and record pressure by monitoring changes in a gas-filled column within a capillary tube, making the pressure measurements sensitive to land surface and atmospheric temperature fluctuations. Because the gas column can expand and contract in response to surface temperature, the instrument records pressure changes that are not indicative of actual reservoir pressure changes. I removed these temperature effects by employing a simple linear regression to determine the relationship between pressure and temperature during a time when pressure changes are not expected.

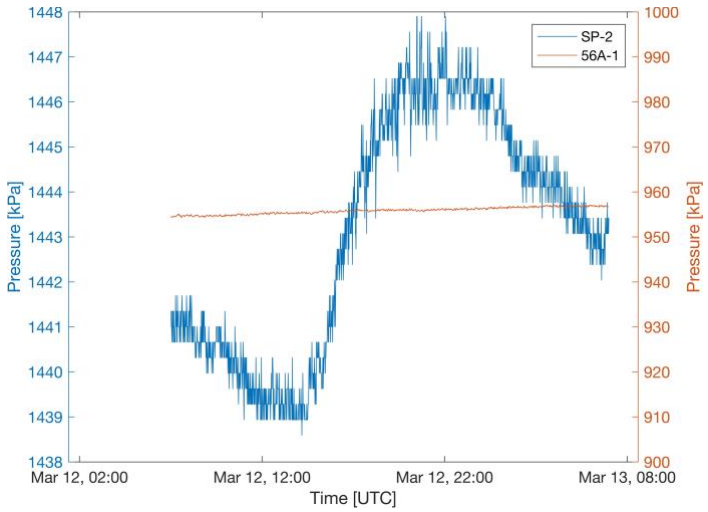

Figure 17: Observed borehole pressure in observation wells SP-2 and 56A-1 during the time frame used to de-trend SP-2 pressure data. Note that 56A-1 pressure remains stable during this period of time indicating the pressure fluctuations seen in SP-2 are likely due to changes in surface temperature fluctuations.

To perform the regression, I identified a 24-hour period of time when reservoir pressure is expected to be at a steady state. Borehole pressures in well 56A-1 during the selected time period (12-Mar-2016 0700 UTC – 13-Mar-2016 0700 UTC) show a nearly constant value, supporting the assumption that the reservoir is not experiencing any significant pressure changes; therefore, any observed pressure changes seen in SP-2 are expected to be caused by surface temperature fluctuations (Figure 17). Figure 18 shows the cross plot of temperature vs pressure for well SP-2. The cross-plot is used to minimize the squared 2-norm (i.e. regression line), which is indicated by the red line (Figure 18). The slope of the regression line is used with the mean temperature during the 24-hour period to model expected pressure deviations caused by gas temperature changes. The modeled pressure deviation is then subtracted from the collected pressure data to remove the temperature effect from the pressure time series in wells 81B-1 and SP-2. Figure 19 shows an example of the raw and temperature-corrected pressure data for SP-2.

Pressure oscillations with an average amplitude of approximately 2 kPa remain following the previously discussed data processing (Figure 19). I expect that remaining oscillations represent the portion of the temperature response not removed from the original data and does not represent pressure changes due to hydrologic stresses; therefore, it is expected that characterization efforts will fit the mean change pressure change in the signal as opposed to these daily oscillations.

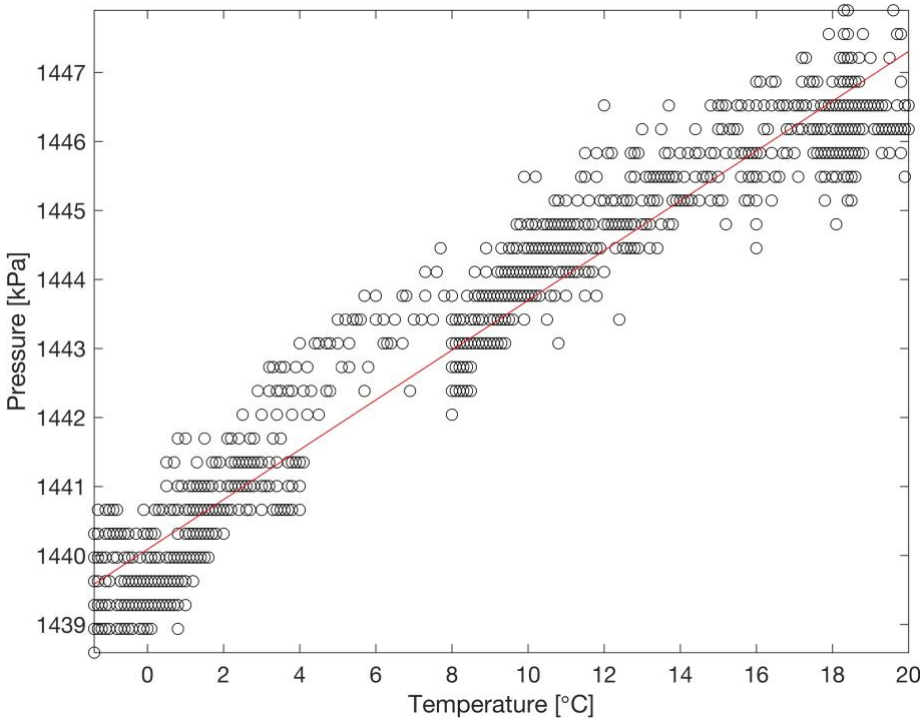

Figure 18: Observation well SP-2 pressure vs temperature cross-plot showing a clear linear relationship between the two. The red line indicates the line of best fit used to model pressure deviation as a function of temperature and de-trend observed SP-2 borehole pressures.

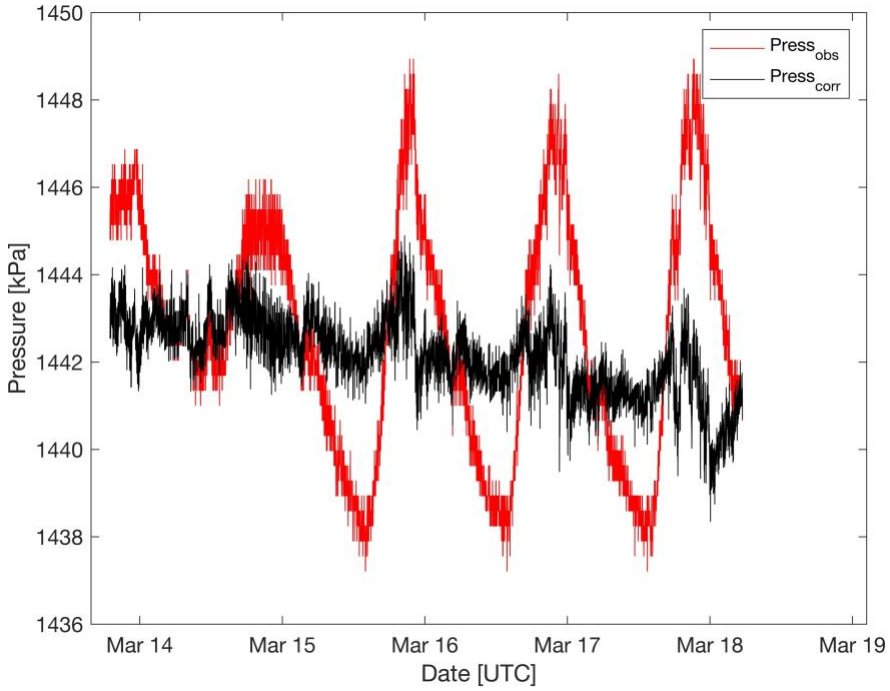

Figure 19: Uncorrected and temperature corrected borehole pressure data from observation well SP-2.

Figure 20 shows the pressure time series for well 56A-1 in addition to de-trended borehole pressure time series for wells 81B-1 and SP-2. Well 81B-1 shows rapid pressure decreases with plant shutdown, and rapid pressure increases during the return to normal plant operations (Figure 20), implying a hydraulic connection with nearby injection wells. 56A-1 also displays rapid responses to changes in power plant operations. Unlike 81B-1, 56A-1 shows rapid pressure increases during plant shutdown, and rapid pressure decreases with the resumption of normal operations (Figure 20), indicating a hydraulic connection to the nearby production wells. SP-2 shows minimal pressure decreases throughout plant shutdown and increased infield injection, at which point the pressure remains nearly constant for the remainder of the field experiment (Figure 20), implying it is located in a hydraulically isolated volume of the reservoir or that combined effects of pumping and injection are balanced at this location.

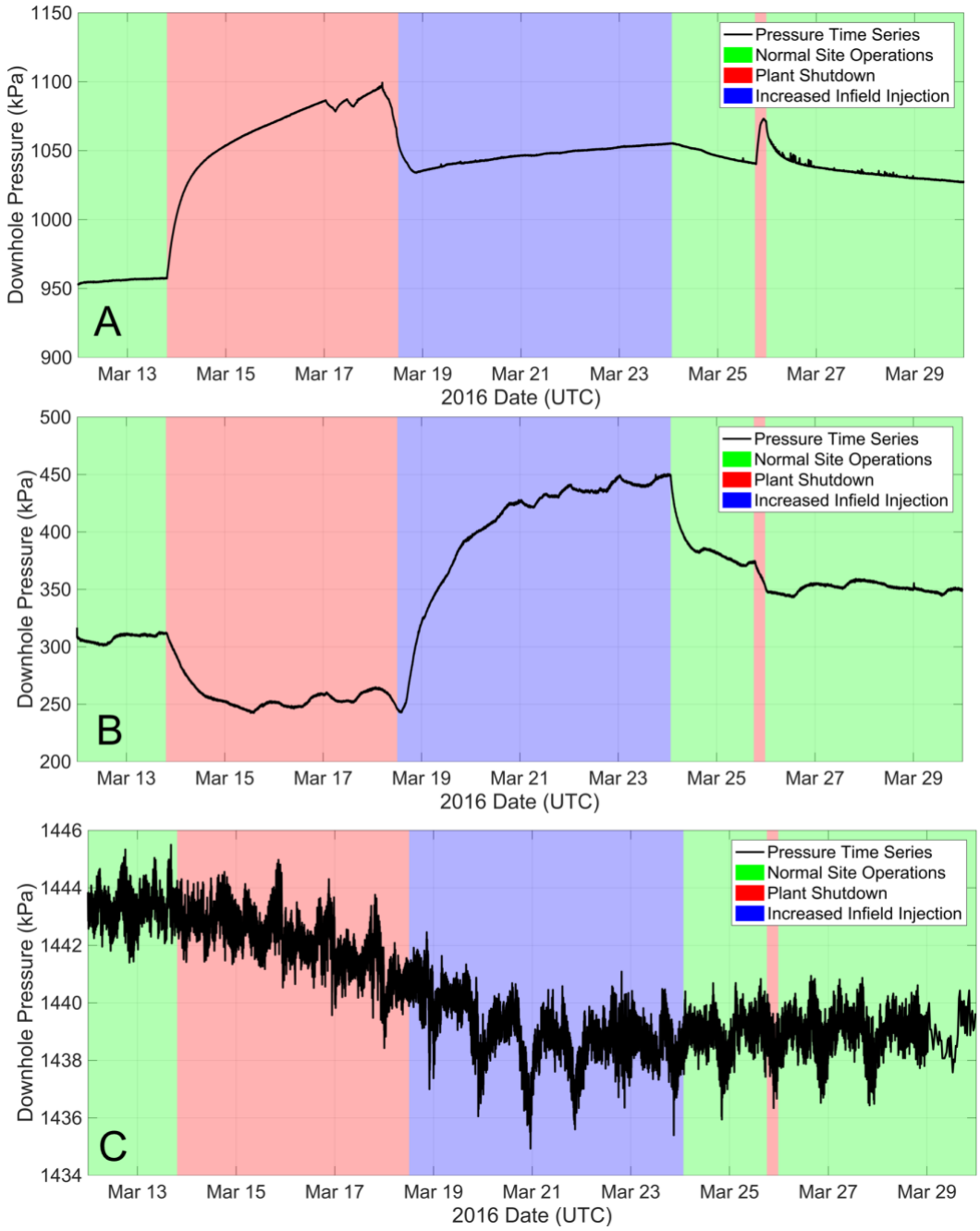

Figure 20: 16-day time series of pressure data collected in three observation wells A) 56A-1, B) 81B-1, and C) SP-2 during the PoroTomo field experiment. Colored panels represent the four stages of the PoroTomo field experiment. Note that SP-2 changes are minimal but displayed with a more refined scale to capture minor pressure changes.

4.3. Analytical Modeling

As an initial attempt at understanding reservoir pressure responses to power plant operations, I utilized an analytical model to estimate effective (i.e. averaged) homogeneous reservoir properties. The Theis solution is used as a forward model in a straightforward parameter estimation routine to determine if observed pressure data can be fit with a homogeneous hydraulic diffusivity. Analytical parameter estimation is limited to wells 56A-1 and 81B-1. SP-2 is omitted due to the minimal pressure changes observed in response to changes in power plant activities throughout the field experiment.

4.3.1. Model Description

Well discussed and used in the literature, the Theis solution predicts aquifer drawdown at any point in space and time in a homogeneous, confined and 2-dimensional aquifer of infinite lateral extent, given a constant pumping rate at a fully penetrating well [*Theis*, 1935]. For the purposes of this work, aquifer drawdown is defined as a decrease in the potentiometric surface from steady-state conditions. Mathematically, the Theis solution is given by:

$$s(r,t) = \frac{Q}{4\,\pi\,T}\,w(u) \tag{4.1}$$

$$u = \frac{r^2 S}{4\,T\,t} \tag{4.2}$$

$$w(u) = \int_u^\infty \frac{e^{-u}}{u}\,du \tag{4.3}$$

where

s is drawdown ($s < 0$ indicates water level increase) [m]

r is radial distance between pumping and observation location [m]

t is time since onset of pumping [s]

S is storativity (product of the storage coefficient and aquifer thickness) [-]

T is transmissivity (product of the hydraulic conductivity and aquifer thickness) [m^2/s]

Q is pumping rate ($Q < 0$ indicates injection) [m^3/s]

I used equation 4.1 to predict water level changes (i.e. drawdown) at wells 56A-1 and 81B-1 for the time period 13-Mar-2016 1915 UTC to 18-Mar-2016 0403 UTC. The selected time period corresponds with plant shutdown, which produces the observed pressure changes in the observation wells. This period of the PoroTomo field experiment shows characteristic diffusive pressure changes in response to the power plant shutdown with minimal data noise. Under normal operating conditions, production and injection rates are quite variable, often manually adjusted by plant operators contributing to noisy data. For these reasons, I chose to use the pressure data collected during stage 2 of the PoroTomo field experiment for the analytical hydraulic characterization.

Based on well location, depth of screened intervals, and observed pressure response (Figure 20), predicted drawdown in well 56A-1 only considers the effects of nearby production wells (Figure 4). I made the assumption that 56A-1 is located far enough away from the injection field that any diffusive pressure changes would not propagate to well 56A-1 prior to the end of plant shutdown. Likewise, well 81B-1

considers only the injection wells in the northern portion of the field area when modeling expected drawdowns.

Plant shutdown occurs in a phased manner with production wells being turned off one at a time over a period of approximately 20 minutes on 13-Mar-2016, starting at 19:18:30 UTC and completed at 19:38:06 UTC. I account for the phased shutdown by determining the drawdown response at each well using equation 4.1. The total drawdown at each observation well is calculated by summing the drawdown due to individual changes in pumping using the principle of superposition. While plant shutdown is accounted for in a phased manner, resumption of plant operations is not well documented; therefore, it is treated as an instantaneous event.

4.3.2. Parameter Estimation

I employed a non-gradient based simplex search algorithm to estimate the reservoir hydraulic diffusivity using observed pressure data collected at wells 81B-1 and 56A-1 independently. The algorithm is a built-in MATLAB library function, *fminsearch*, which is based on the Nelder-Mead simplex algorithm. I used the complete data set for the time period mentioned during inversion. This includes 6,289 data points for well 56A-1 and 6,271 data points for well 81B-1. The objective function that is used to determine the optimal parameters is:

$$\min_{m} \|d - s(m)\|_2^2 \tag{4.4}$$

where

d is a vector of observed drawdowns in the observation well over time [m]

$s(m)$ is calculated as given by equation 4.1 [m]

m is a vector of current parameter values (T, S)

As discussed in Chapter 3, the optimization algorithm uses two convergence criteria to determine that the optimal value has been achieved. The first convergence criterion requires the minimum change in consecutive parameter values to be less than 1 x 10^{-4}, and the second requires that the minimum difference in function values also be less than 1 x 10^{-4}. The objective function is determined to be minimized when the above two convergence criteria are achieved.

4.3.3 Results and Analysis

The parameter estimation obtained using data from well 56A-1 yields $T = 1.3 \times 10^{-2}$[m^2/s] and $S = 1.7 \times 10^{-4}$ [-], or a hydraulic diffusivity (i.e., T/S) of 77.5 [m^2/s]. Figure 21 shows that simulated pressure changes using optimal parameters provide adequate data fit. The data misfit has an RMSE of 2.0 kPa, which is less than the expected data uncertainty of $\pm$ 6.9 kPa. The estimated diffusivity I obtained is in close agreement with the diffusivity estimate reported by *Cardiff et al.* [2018], which they note agrees with diffusivity estimates obtained by power plant operators shortly after well completion. The slight difference between my results and those reported by *Cardiff et al.* [2018] is attributed to the fact that this work uses a longer portion of the data set for the parameter estimation, with both works using similar parameter estimation strategies.

Parameter estimation using pressure data from well 81B-1 produces individual parameter estimates $T = 3.3 \times 10^{-2}$[m^2/s] and $S = 4.5 \times 10^{-4}$ [-], which differ from the estimates obtained for well 56A-1; however, the estimated hydraulic diffusivity is 73.8 m^2/s, which is in close agreement with well 56A-1. The modeled pressure changes show a degraded fit with the observed data compared to well 56A-1 (Figure 21), and likewise has a slightly larger RMSE of 7.4 kPa which is only slightly larger than the expected data measurement error of $\pm$ 6.9 kPa.

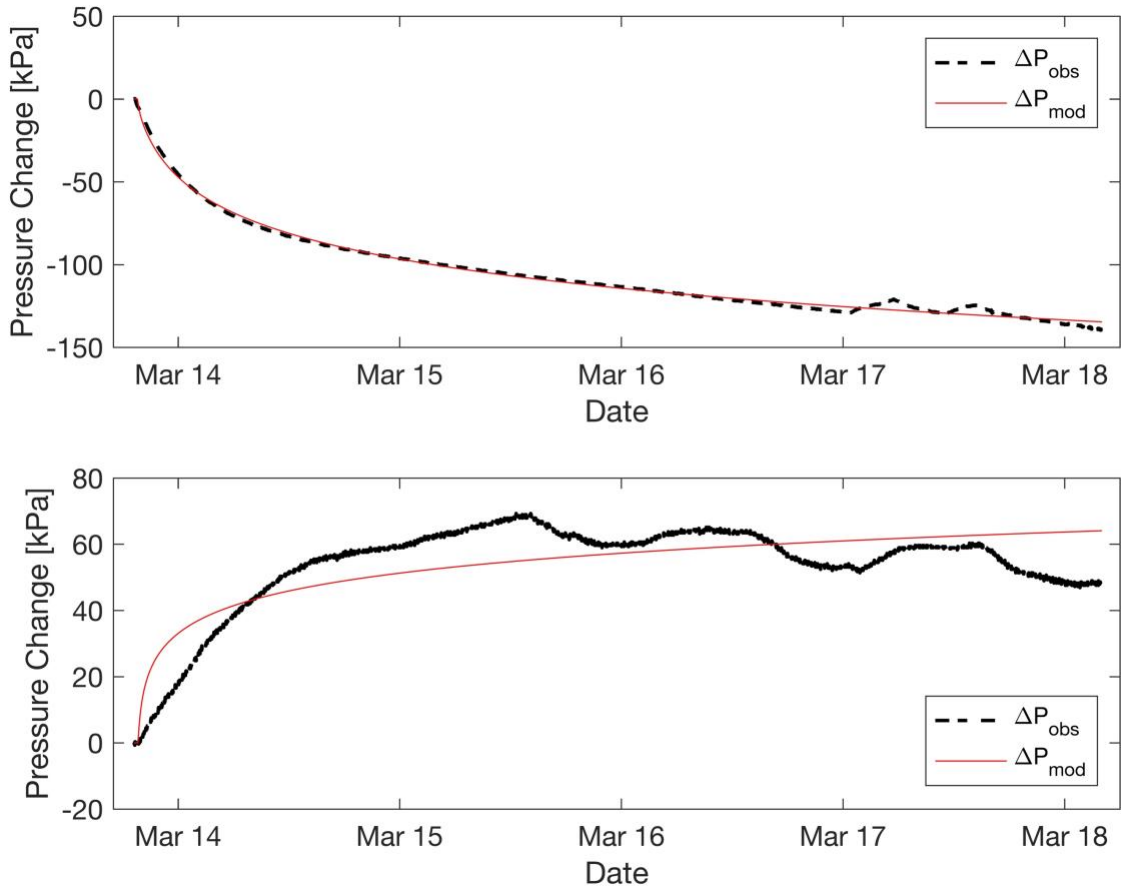

Figure 21:Observed pressure changes during plant shutdown and modeled drawdown with best fit parameters in observation wells 56A-1 (top) and 81B-1 (bottom)

Parameter estimates indicate that modeling the Brady reservoir using homogeneous hydraulic properties is not appropriate. Despite having similar hydraulic diffusivity estimates, wells 56A-1 and 81B-1 have different transmissivity and storativity estimates. Figure 21 also shows that well 81B-1 has a noticeably worse data fit and a larger RMSE of 7.4 kPa when compared to the data fit and RMSE for 56A-1. In the next stage of my modeling, I utilized zoned hydrogeologic models based on existing geological data in order to assess multiple conceptual models for the 3-D flow (and thus heat transport) at Brady.

4.4. Numerical Modeling

Analytical modeling results indicate that the Brady pressure data may not be adequately fit using a homogeneous hydraulic conductivity distribution. Also, assuming that the Brady reservoir consists of a uniform, 2-dimensional permeable region that intersects all wells is unrealistic given the site geometry and complex geologic setting. Therefore, follow-on hydraulic characterization focused on 3-D numerical modeling to allow for reservoir heterogeneity. Numerical modeling was conducted using the USGS finite-volume code MODFLOW with Groundwater Vistas operating as the pre- and post-processor, which produce inputs for, runs of, and visualizations of results from the MODFLOW code.

4.4.1. Model Domain

The numerical groundwater flow model uses the PoroTomo coordinate system, which is a Cartesian coordinate system based on rotated UTM coordinates. Table 3 shows corner coordinates for the Brady Natural Lab in the rotated PoroTomo coordinate system, which is the focus of this hydraulic characterization. Figure 22 shows a small portion of the groundwater flow model domain in the rotated PoroTomo coordinate system, which is produced by rotating UTM coordinates about the left lower corner of the Brady Natural Lab (UTM 11S 327850.8122, 4407606.205) by an angle of -36.4219° (i.e., counterclockwise rotation).

To prevent improperly placed boundaries from imposing unwanted effects on the numerical solution within the natural lab and also allow all wells to be included in the model domain, I placed the model boundaries far beyond the extent of the Brady Natural Lab. To determine the proper distance to the far field boundaries, I simulated a dipole pumping test iteratively, moving the far field boundary away from the natural lab until the total drawdown was less than 10 cm at the boundary. Based on the results of the dipole pumping simulations, I created a model domain with x, y, and z dimensions of 7000 m x 13,000 m x 6000 m in size, and uniform grid cell dimensions of 100 m x 100 m x 100 m. For comparison, a volume representing the central area of the site (i.e., containing all wells and their associated pumping intervals) covers a region approximately 1,000 m x 3,000 m x 2000 m in size.

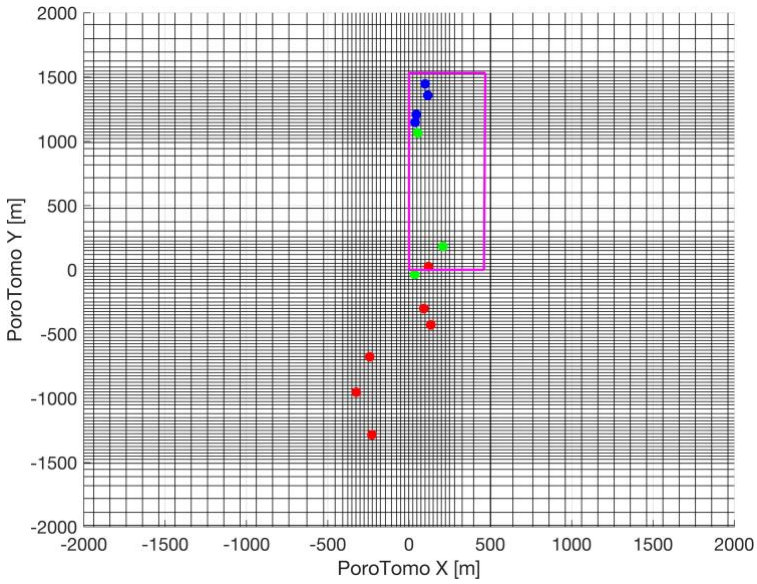

Figure 22: A portion of the groundwater flow model domain plan view in the rotated PoroTomo coordinate system showing grid refinement areas where wells are located. Brady Natural Lab is indicated by the magenta box. Injections wells are indicated by blue circles, productions wells are red circles, and observation wells are green circles.

I included the wells in the model domain as analytic elements using well locations and screened intervals seen in Table 2. Analytic element wells are grid-independent features that allow the wells to be mapped to the appropriate MODFLOW cells as a point or line within the model. Following well placement in the modeling domain, I refined the finite-difference grid to 25 m x 25 m x 25 m voxels in all grid cells containing a screened interval. This refinement serves to further increase modeled pressure change accuracy in the vicinity of active wells. Following this refinement, the non-uniform model domain contains 219 rows, 100 columns, and 119 layers, and approximately ~2.6 million active finite difference cells.

Table 3: Groundwater flow model and Brady Natural Lab corners in the rotated PoroTomo coordinate system

Brady Natural Lab Corners			**Groundwater Model Corners**	
	PoroTomo X [m]	PoroTomo Y [m]	PoroTomo X [m]	PoroTomo Y [m]
Southwest	0	0	-2889	-6438
Northwest	0	1533	-2873	6540
Southeast	461	0	4125	-6417
Northeast	470	1531	4131	6579

The average land surface elevation throughout Brady is ~ 1230 m above mean sea level (amsl). Water level elevations in 81B-1 indicate that groundwater levels are approximately 100 m below land surface; therefore, I placed the model top elevation at 1110 m amsl. This elevation allows the screened intervals of all injection wells to be incorporated into the model domain (Figure 23). It is unclear from collected data whether the Brady aquifer is confined or unconfined; therefore, I designated all model layers as confined. Treating the layers as confined is consistent with the low storativity estimates returned during analytic parameter estimation and helps to limit the numerical instability associated with cell drying and re-wetting, which can occur with unconfined layers.

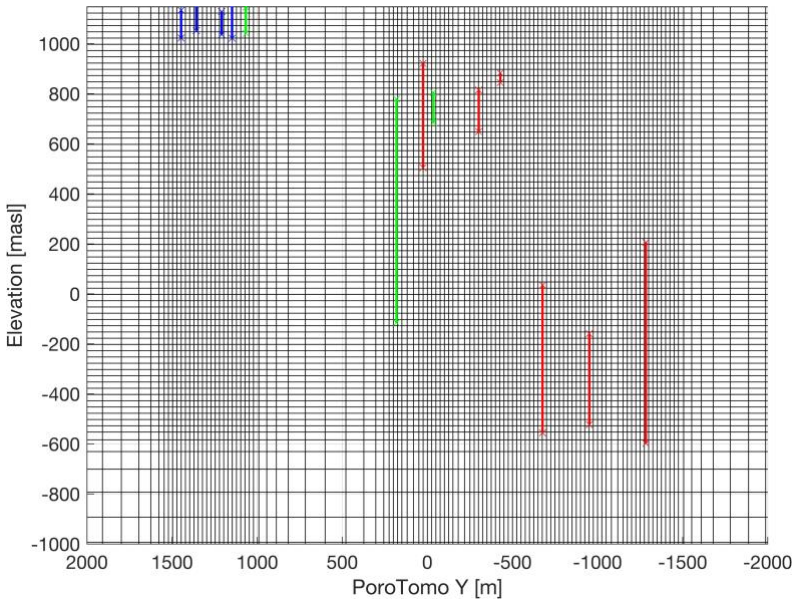

Figure 23: Vertical slice of a portion of the groundwater flow model at PoroTomo X = 500 m showing the location of screened intervals within the modeling domain. The finite-difference grid is refined to 25 m voxels in areas with well screens. Injection wells are blue, production wells are red, and observation wells are green.

4.4.2. Boundary Conditions

The topography of Brady shows a NE-SW trending basin bounded on the NW and SE boundaries by ridges forming topographic highs. I conceptualized that regional groundwater flow will be concentrated in the basin, moving generally NE to SW, while the bounding ridges will act as barriers to flow out of the basin. Given the local topography, zero-flux (i.e., no-flow) boundaries span every row of the groundwater model on both PoroTomo X edges of the groundwater model. I do not explicitly assign these boundary conditions, as MODFLOW treats unspecified model edges as no-flow boundaries by default.

To create the expected overall regional flow, I placed constant head boundaries at row 1 (NE) and row 219 (SW) of the model. The constant head boundary spans all

columns and layers along these two rows. I assume a constant pressure gradient exists between wells 56A-1 and 81B-1 to determine head values at the far-field boundaries. Under this assumption, I used observed pressure data under normal plant operating conditions to calculate the hydraulic gradient between the two wells, and then used that hydraulic gradient to determine the hydraulic head at each far-field boundary. Using this procedure, I set the constant boundary along row 1 at 1200 m, and the constant head boundary along row 219 at 1024 m.

4.4.3. Temporal Discretization

The Brady groundwater flow model contains two stress periods: a steady-state simulation and a transient simulation. I designated the steady-state simulation as stress period one and gave it a total time of 30 days (43200 minutes in MODFLOW). The time assigned to the steady state solution is for bookkeeping purposes only and does not affect the numerical solution. The steady-state solution simulates the hydraulic head distribution throughout the reservoir under normal operating conditions prior to the plant shutdown (Stage 2) portion of the PoroTomo experiment.

Again, due to poor monitoring of injection flow rates, the transient simulation during the second stress period simulates reservoir response during power plant shutdown only. As with the analytical modeling, the transient simulation covers 13-Mar-2016 19:15:00 UTC – 18 Mar-2016 04:03:00, totaling 6,287 minutes. I discretized the transient stress period into 100 time steps, using a time step multiplier (β) of 1.05. While a smaller β creates slightly larger early time steps, capturing the early transients on the order of

minutes as compared to sub-seconds is appropriate given the total duration of the stress period. Figure 24 illustrates the tradeoff of using $\beta = 1.05$ for this particular modeling scenario, specifically the unreasonably large late time steps and unnecessarily small early time steps.

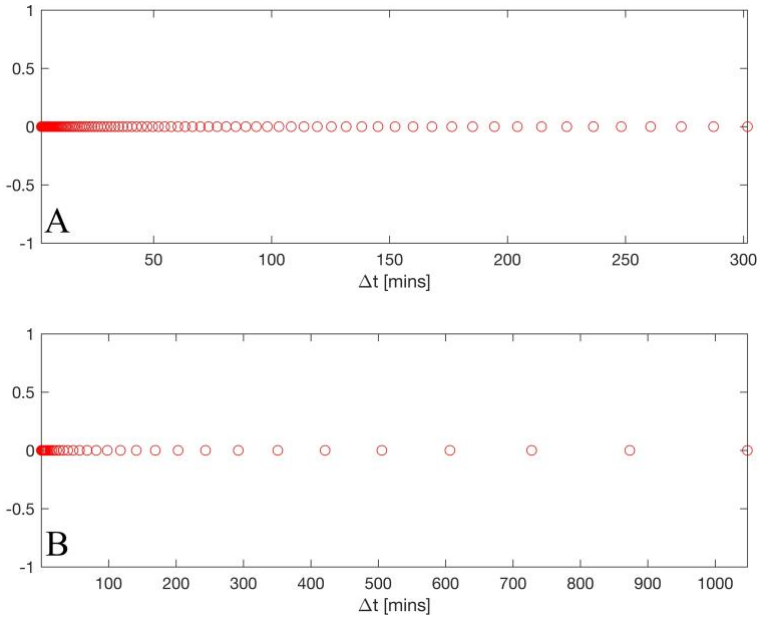

Figure 24: Individual time steps showing the effect of different time step multipliers on early and late time steps. Observe that A) $\beta = 1.05$ early time steps are small enough to provide necessary accuracy with early transience while maintaining smaller late time steps. This is in contrast to B) $\beta = 1.2$ which allows late time steps to grow unreasonably large at the sacrifice of unnecessarily small early time steps for this particular modeling scenario.

4.4.4. Conceptual Models

Given the structural and geologic complexity of the Brady reservoir, I tested a wide range of conceptual models to understand which models are consistent with the collected pressure data and field observations of hydrothermal fluids at exposed fault traces. The conceptual models tested fall into general categories as follows: zoned heterogeneous porous media, fault features within a homogeneous porous media, fault

features within a heterogeneous porous media, and fault features and associated damage zones within a homogeneous porous media. The following sections describe each conceptual model in more detail.

4.4.4.1. Zoned Heterogeneous Porous Media

The zoned heterogeneous porous media conceptual models assume that the volume of the groundwater flow model is large enough that individual faults and fractures need not be modeled explicitly, as variability in porous media properties exerts primary control on groundwater flow. Lithologic units identified by *Siler et al.* [2016] are lumped into hydrostratigraphic units based on expected hydraulic properties of each lithology. Analytical parameter estimation indicates that a homogeneous model does not adequately fit collected pressure data; therefore, the simplest numerical model consists of 2 hydrologic zones, sedimentary units in one zone and volcanic units in the second. Splitting sedimentary units into groups with expected similar hydraulic properties, I increased geologic complexity by including additional hydrologic zones incrementally to determine the least geologically complex model necessary to fit the data. Appendix A describes how geologic units were lumped into individual hydrologic zones.

After determining the minimum necessary complexity to fit the data, I investigated the presence of a point of diminishing returns where adding geologic complexity does not significantly improve data fit. Including heterogeneity into numerical models increases model run times in a non-linear manner; therefore, a common tradeoff in modeling efforts is improving model run times by decreasing model complexity while honoring the collected data.

4.4.4.2. Faults Within Homogeneous Porous Media

As discussed above, multiple lines of evidence point to groundwater flow that occurs preferentially along fault planes throughout the reservoir. To test this hypothesis, I developed a conceptual model that consists of 2 hydrologic zones: 1) fault features and 2) porous media. Fault features are placed in the groundwater flow model based on prior fault modeling efforts. *Jolie et al.* [2015] conducted a large 3-D modeling effort, based on field measurements and geologic mapping by *Faulds et al.* [2003], which identified, georeferenced, and modeled approximately 64 fault planes throughout Brady. This modeling effort provides fault locations that I used to build conceptual models that group cells containing all known fault planes into one hydrostratigraphic unit and groups the remainder of the modeling domain as homogeneous porous media.

Although a large number of faults have been identified at Brady, there is not a thorough understanding of how many are hydrologically active. Nicholas Davatzes, a researcher at Temple University, has prioritized subsets of faults based on geometry and location within the reservoir. Using this prioritization scheme, I created further conceptual models, incrementally decreasing the number of faults in the model domain from 64 to 15 to determine if observed pressure data support flow along all faults or only some critical subset.

4.4.4.3. Faults Within Heterogeneous Porous Media

Given the geologic heterogeneity at Brady, a conceptual model that treats the reservoir rock as a homogeneous unit described by one set of hydraulic parameters is likely an oversimplification. While discussing the spatial correlation of microseismic

events at Brady, *Davatzes et al.* [2013] notes a lack of these events near the injection wells, which are known to inject fluids into prominent shallow faults. They attribute the lack of microseismicity in this area to the combined effect of porous media flow and preferential flow along fault zones, enhancing injection pressure dissipation, thereby reducing the stress accumulation in shallow fault zones [*Davatzes et al.*, 2013].

To account for these field observations, I created a set of conceptual models that group the reservoir rock sedimentary units, igneous / metamorphic units, and discrete faults into separate hydrostratigraphic units. While this does not account for the detailed heterogeneity of the Brady geology, it is a more reasonable simplification than that discussed above, which considers the reservoir rock as a homogeneous porous media. This conceptualization allows for shallow porous media flow in conjunction with preferential planar flow while minimizing model run times by limiting model heterogeneity.

4.4.4.4. Faults and Damage Zone Within Homogeneous Porous Media

While faults may act as conduits or barriers to flow (making a single set of hydraulic properties reasonable), researchers on fluid-fault interaction have observed that faults can display a more interesting "conduit-barrier" behavior. *Bense et al.* [2013] discuss multiple conceptual models related to groundwater flow through faulted geologic systems. Figure 25 shows one such conceptual model. In this model, groundwater follows the planar geometry of the fault and field observations would suggest a high permeability fault; however, the fault itself is a low permeability zone – consisting primarily of low permeability fault gouge – with a highly fractured damage zone providing high

permeability flow pathways allowing for planar flow paralleling the fault zone [*Bense et al.*, 2013].

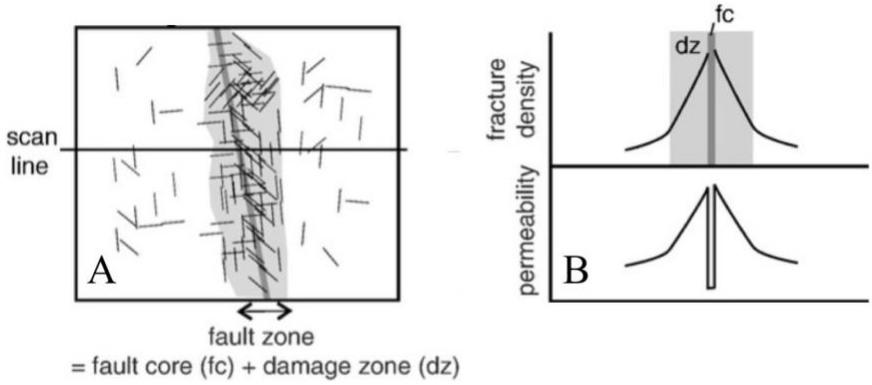

Figure 25: A) Plan view of a fault zone showing a distinctive fault core centered on a damage zone with decreasing fracture density moving away from the fault zone. B) Qualitative interpretation of permeability and fracture density moving along the scan line in (A). Note increasing fracture density and permeability in the damage zone and significantly lower permeability in the damage zone. Adapted from Bense et al. [2013].

To determine if this conceptual model fits the observed pressure data at Brady, I modified the discrete fault conceptual models above. These conceptual models contain three hydrostratigraphic units, as opposed to two as discussed above. The reservoir rock is again treated as a homogeneous porous medium; the faults are imported as discussed above and treated as a second hydrostratigraphic unit. Then, a third unit was created that surrounds each imported fault and allows differentiation between fault cores and damage zones.

4.4.5. Parameter Estimation

I used a zoned parameter estimation approach to estimate the hydraulic conductivity and specific storage distribution throughout Brady. Within each conceptual model described above, I treat each hydrostratigraphic unit as a zone of homogeneous

hydraulic properties. Each hydrostratigraphic unit contains three properties to be estimated: horizontal and vertical hydraulic conductivity (K_x, K_z) and specific storage (S_s); therefore, the total number of model parameters is a factor of three larger than the number of hydrostratigraphic units in the model. I assume isotropic aquifer conditions, which allowed me to make K_z a non-adjustable parameter by tying it to K_x; therefore, during the inversion changes in K_x will be mirrored by K_z. Assigning K_z as a non-adjustable parameter also decreases inversion run times by reducing the number of model calls necessary to calculate model sensitivities (i.e., Jacobians) and complete each inversion iteration.

To conduct the inversion I used PEST, a commercially available software code, which integrates seamlessly with MODFLOW through Groundwater Vistas. PEST utilizes a gradient-based inversion approach with the Levenberg-Marquardt algorithm. The numerical parameter estimation uses data from 13-Mar-2016 19:15:00 UTC – 18 Mar-2016 04:03:00, which is consistent with the time period used for the analytical inversion, to estimate the hydraulic parameters. Unlike the analytical inversion, data from all three observation wells are fit simultaneously. To reduce the volume of data that must be fit, I selected a subset of the data from the pressure change curves for use in inversion. I chose five data points per pressure change curve so that they capture the overall shape of the observed pressure change curves, ensuring that selected points cover early, intermediate, and late times. This data reduction strategy also helps to reduce inversion run times. Figure 26 shows the full drawdown time series for wells 56A-1, 81B-1, and SP-2, with the five selected data points used during inversion.

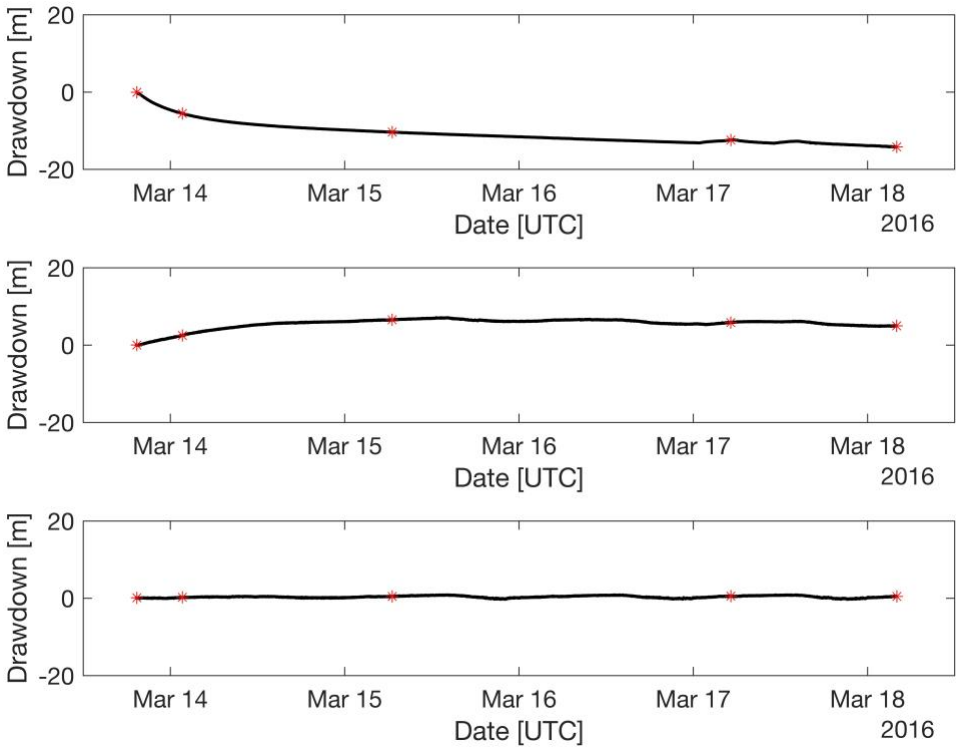

Figure 26: Observed drawdown in wells A) 56A-1, B) 81B-1, and C) SP-2 during Brady plant shutdown. The black line represents the full time series during plant shutdown. Red asterisks denote the data points selected to form a characteristic drawdown curve for data fitting during parameter estimation.

The objective function PEST minimizes is the sum of the squared weighted model residuals (Φ ($\mathbf{K}, \mathbf{S_s}$)) [*Doherty*, 2016]. Mathematically it is:

$$\min_{K,S_s} \sum_{i=1}^{n} [w_i(h(\mathbf{K}, \mathbf{S_s})_i - h_i)]^2 \tag{4.5}$$

where

w_i is the residual weight given by the expected standard deviation of the data measurement uncertainty [m]

h_i is the i^{th} observed hydraulic head [m]

$h(\mathbf{K}, \mathbf{S_s})_i$ is the i^{th} simulated hydraulic head with the vector of current parameters [m]

$\mathbf{K}$ is a vector of current hydraulic conductivity estimates [m/min]

$\mathbf{S_s}$ is a vector of current specific storage estimates [m^{-1}]

n is the number of observations

Looking at equation 4.5, it can be seen that the ratio of weight values between individual observations is of more importance than the actual value of the weight. Because the individual observations all have identical expected measurement uncertainty, I assign all observations a weight of one.

The convergence criteria for the inversion requires that the three lowest values of Φ are within a relative distance of 0.01, the change in parameters between successive iterations is 0.01, or three consecutive optimization iterations elapse with no Φ reduction. If PEST determines convergence because three iterations elapse with no Φ reduction, I restart the inversion using the best estimates and allow the inversion to converge using one of the other convergence criteria to ensure that estimated parameters do not represent a failure of the optimization algorithm.

Analytical parameter estimation efforts provided the initial parameter estimates for the numerical parameter estimation. Each conceptual model starts with homogeneous parameters with each hydrostratigraphic unit assigned values of $\mathbf{K} = 1.3 \times 10^{-4}$ [m/min] and $\mathbf{S_s} = 4.15 \times 10^{-8}$ [m^{-1}]. The analytical inversion using the Theis solution provided estimates of T and S; therefore, I divided the estimated parameter values by the model thickness (6000 m) and apply the appropriate unit conversions to get $\mathbf{K}$ [m/min] and $\mathbf{S_s}$ in [m^{-1}].

4.4.6. Results

4.4.6.1. Zoned Heterogeneous Porous Media

Table 4 shows parameter estimates and 95% confidence intervals for heterogeneous porous media with increasing geologic complexity of the conceptual models. Increasing geologic complexity beyond two hydrologic zones significantly increases estimated parameter uncertainty, primarily across shallower geologic units. Estimated specific storage order of magnitude indicates Brady is showing confined behavior across all models.

Table 4: Estimated model parameters and 95% confidence intervals obtained through inversion of pressure data using a conceptual model of heterogeneous porous media. Parameter subscript indicates hydrologic zone number. Units of hydraulic conductivity are m/s and units of specific storage are m^{-1}.

2 Hydrologic Zones			
K_1	7.2×10^{-4}	1.9×10^{-4}	2.7×10^{-3}
K_2	1.1×10^{-6}	7.9×10^{-7}	1.6×10^{-6}
Ss_1	4.8×10^{-11}	2.4×10^{-16}	9.8×10^{-6}
Ss_2	2.5×10^{-6}	1.1×10^{-6}	5.6×10^{-6}
3 Hydrologic Zones			
K_1	2.5×10^{-6}	8.2×10^{-24}	4.6×10^{13}
K_2	6.8×10^{-4}	1.9×10^{-4}	2.4×10^{-3}
K_3	1.4×10^{-6}	6.7×10^{-7}	1.6×10^{-6}
Ss_1	1.6×10^{-8}	5.2×10^{-38}	1.0×10^{0}
Ss_2	5.9×10^{-9}	1.4×10^{-12}	2.5×10^{-5}
Ss_3	2.8×10^{-6}	1.1×10^{-6}	7.0×10^{-6}
5 Hydrologic Zones			
K_1	5.3×10^{-6}	7.7×10^{-11}	3.7×10^{-1}
K_2	1.0×10^{-2}	8.2×10^{-3}	1.3×10^{-2}
K_3	5.5×10^{-7}	5.7×10^{-8}	5.3×10^{-6}
K_4	2.3×10^{-7}	2.1×10^{-11}	2.5×10^{-3}
K_5	5.6×10^{-9}	2.8×10^{-14}	1.1×10^{-3}
Ss_1	8.1×10^{-8}	1.1×10^{-15}	1.0×10^{0}
Ss_2	1.8×10^{-7}	3.9×10^{-10}	8.4×10^{-5}
Ss_3	6.4×10^{-7}	9.6×10^{-8}	4.3×10^{-6}
Ss_4	1.0×10^{-4}	8.2×10^{-7}	1.3×10^{-2}
Ss_5	8.2×10^{-9}	2.2×10^{-11}	3.1×10^{-6}

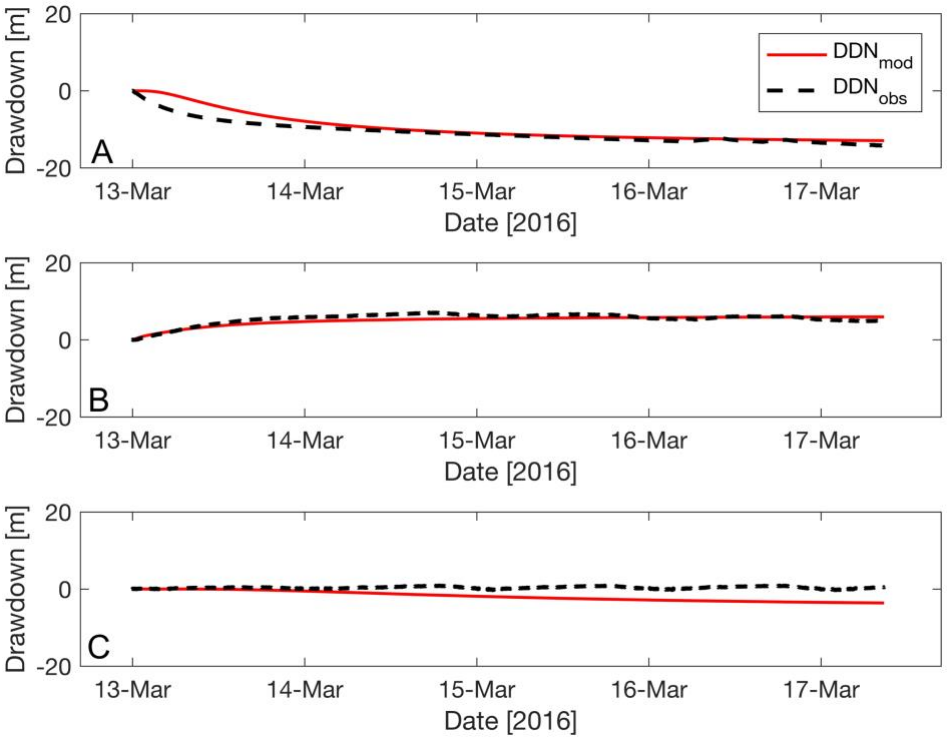

Figure 27: Modeled data fit at wells A) 56A-1, B)81B-1, and C) SP-2 using optimal parameters.

Figure 27 shows modeled data fit for a heterogeneous porous media model with two hydrologic zones. 56A-1 shows good data fit at intermediate and late times, while predicting a slower pressure changed than observed at early times. Mean absolute error (MAE) at individual wells and Φ remain consistent with two and three hydrologic zones, while vastly improving with geologic complexity increasing to five hydrologic zones (Table 5). Geologic complexity beyond five hydrologic zones risks overfitting observed data and non-linearly increases parameter estimation time; therefore, this analysis does not consider further geologic complexity.

Table 5: Mean absolute error at each observation well and objective function value for optimal parameter estimates with increasing geologic complexity.

2 Hydrologic Zones			
Well	56A-1	81B-1	SP-2
MAE [m]	1.2	0.5	1.9
Φ [m^2]	54.7		
3 Hydrologic Zones			
Well	56A-1	81B-1	SP-2
MAE [m]	1.4	0.6	1.8
Φ [m^2]	54.7		
5 Hydrologic Zones			
Well	56A-1	81B-1	SP-2
MAE [m]	0.2	0.5	0.3
Φ [m^2]	3.1		

4.4.6.2. Faults Within Homogeneous Porous Media

Table 6 shows parameter estimates and 95% confidence intervals for groundwater flow models using fractures within a homogeneous porous media matrix conceptual model with zone 1 representing the reservoir rock and zone 2 representing the faults. Estimates of hydraulic conductivity for the reservoir rock are two orders of magnitude larger than those for the faults, indicating that individual faults potentially act as barriers to groundwater flow (Table 6). Specific storage estimates are within ranges expected for confined aquifer conditions in all models (Table 7).

Figure 28 shows observed and modeled pressure changes with optimal parameters for the model with 19 modeled faults. Simulated pressure changes provide best data fit at intermediate and late times, with decreased fit observed during early times at wells 56A-1. Simulated pressure curves show best fit at late times with decreased fit during early and intermediate times at 81B-1. SP-2 shows good fit at early time with fit decreasing throughout the remainder of the time series (Figure 28).

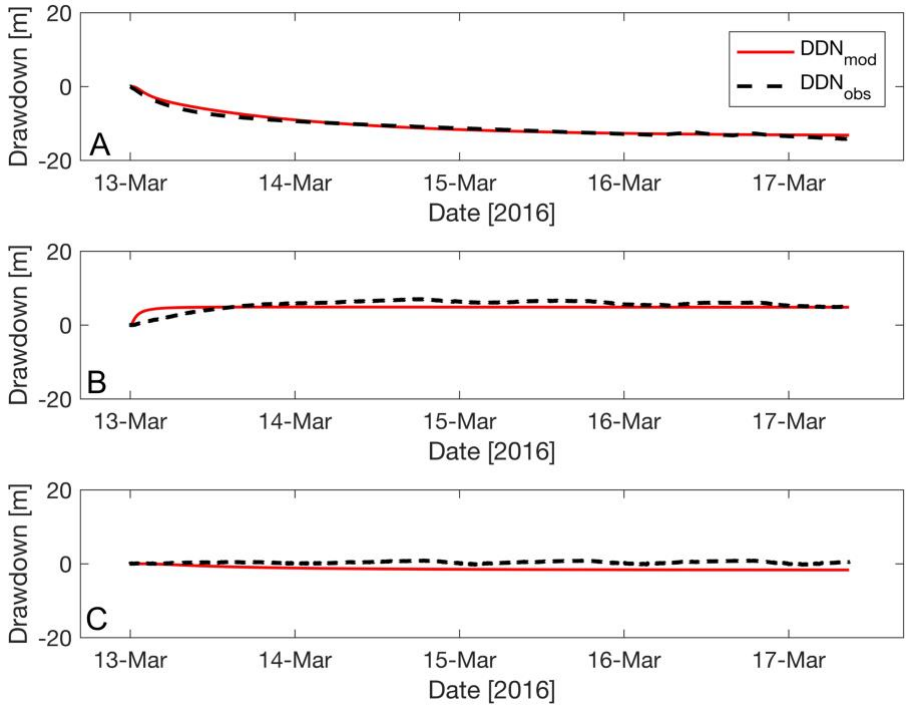

Figure 28: Modeled data fit at wells A) 56A-1, B)81B-1, and C) SP-2 using optimal parameters.

MAE and Φ provide a direct comparison of data fit among remaining models with decreasing number of fractures. Table 7 shows that including all 64 identified faults in the flow model provides the best data fit, with MAE and Φ increasing as the number of modeled faults decreases. Decreasing the number of modeled faults from 64 to 18 shows that despite increasing misfit, MAE is only marginally above the expected data measurement error of $\pm$ 0.7 m drawdown, indicating that groundwater flow is likely occurring along some smaller subset of faults (Table 7). Decreasing the number of modeled faults from 19 to 16 creates a marked increase in MAE and Φ.

Table 6: Estimated model parameters and 95% confidence intervals obtained through inversion of pressure data using a conceptual model of identified faults within a homogeneous porous media. Parameter subscript indicates hydrologic zone number. Units of hydraulic conductivity are m/s and units of specific storage are m^{-1}.

All Faults (64 Faults)			
	Parameter Estimate	Lower Limit	Upper Limit
K_{rock}	1.5×10^{-4}	1.2×10^{-5}	2.0×10^{-3}
K_{fault}	1.6×10^{-6}	1.3×10^{-6}	1.9×10^{-6}
Ss_{rock}	4.0×10^{-4}	4.0×10^{-5}	4.1×10^{-3}
Ss_{fault}	1.2×10^{-6}	7.3×10^{-7}	2.0×10^{-6}
Primary, Secondary, and Tertiary Faults (28 Faults)			
	Parameter Estimate	Lower Limit	Upper Limit
K_{rock}	1.8×10^{-3}	1.2×10^{-3}	2.8×10^{-3}
K_{fault}	8.5×10^{-7}	7.0×10^{-7}	1.0×10^{-6}
Ss_{rock}	5.3×10^{-9}	4.3×10^{-9}	6.4×10^{-9}
Ss_{fault}	1.5×10^{-6}	8.1×10^{-7}	2.7×10^{-6}
Primary and Secondary Faults (18 Faults)			
	Parameter Estimate	Lower Limit	Upper Limit
K_{rock}	4.3×10^{-3}	1.9×10^{-5}	1.0×10^{0}
K_{fault}	1.0×10^{-6}	8.1×10^{-7}	1.3×10^{-6}
Ss_{rock}	8.6×10^{-6}	4.7×10^{-7}	1.6×10^{-4}
Ss_{fault}	5.6×10^{-7}	1.1×10^{-7}	2.8×10^{-6}
Primary Faults (15 Faults)			
	Parameter Estimate	Lower Limit	Upper Limit
K_{rock}	6.3×10^{-4}	4.8×10^{-9}	8.3×10^{1}
K_{fault}	7.0×10^{-7}	1.1×10^{-7}	4.4×10^{-6}
Ss_{rock}	8.2×10^{-7}	1.2×10^{-160}	1.0×10^{0}
Ss_{fault}	5.0×10^{-7}	1.2×10^{-8}	2.1×10^{-5}

Table 7: Mean absolute error at each observation well and objective function value for optimal parameter estimates showing increasing model misfit as the number of modeled faults decreases.

All Faults (64 Faults)			
Well	56A-1	81B-1	SP-2
MAE [m]	0.7	0.8	0.7
Φ [m^2]	12.6		
Primary, Secondary, and Tertiary Faults (28 Faults)			
Well	56A-1	81B-1	SP-2
MAE [m]	0.7	0.9	1.5
Φ [m^2]	30.1		
Primary and Secondary Faults (18 Faults)			
Well	56A-1	81B-1	SP-2
MAE [m]	0.6	1.0	1.3
Φ [m^2]	23.9		
Primary Faults (15 Faults)			
Well	56A-1	81B-1	SP-2
MAE [m]	2.5	2.1	2.4
Φ [m^2]	129.6		

Figure 29 shows steady-state reservoir hydraulic head distribution – simulating normal plant operations – in plan view at an elevation of 1050 masl with optimal parameters using a conceptual model of 18 faults within a homogeneous porous medium. MODPATH simulations show advective flow paths through the aquifer system, illustrated by red lines with arrows indicating flow direction. Simulated flow paths follow identified fault traces throughout the reservoir from injection well 18D-31 (Figure 29) to the SW constant head boundary and the capture zone created by the deeper production well 47C-1 (Figure 29). Figure 30 shows a strike-parallel cross-section along A - A' with red lines representing advective flow from well 18D-31 to the SW constant head boundary and an intermediate capture zone created by well 47C-1.

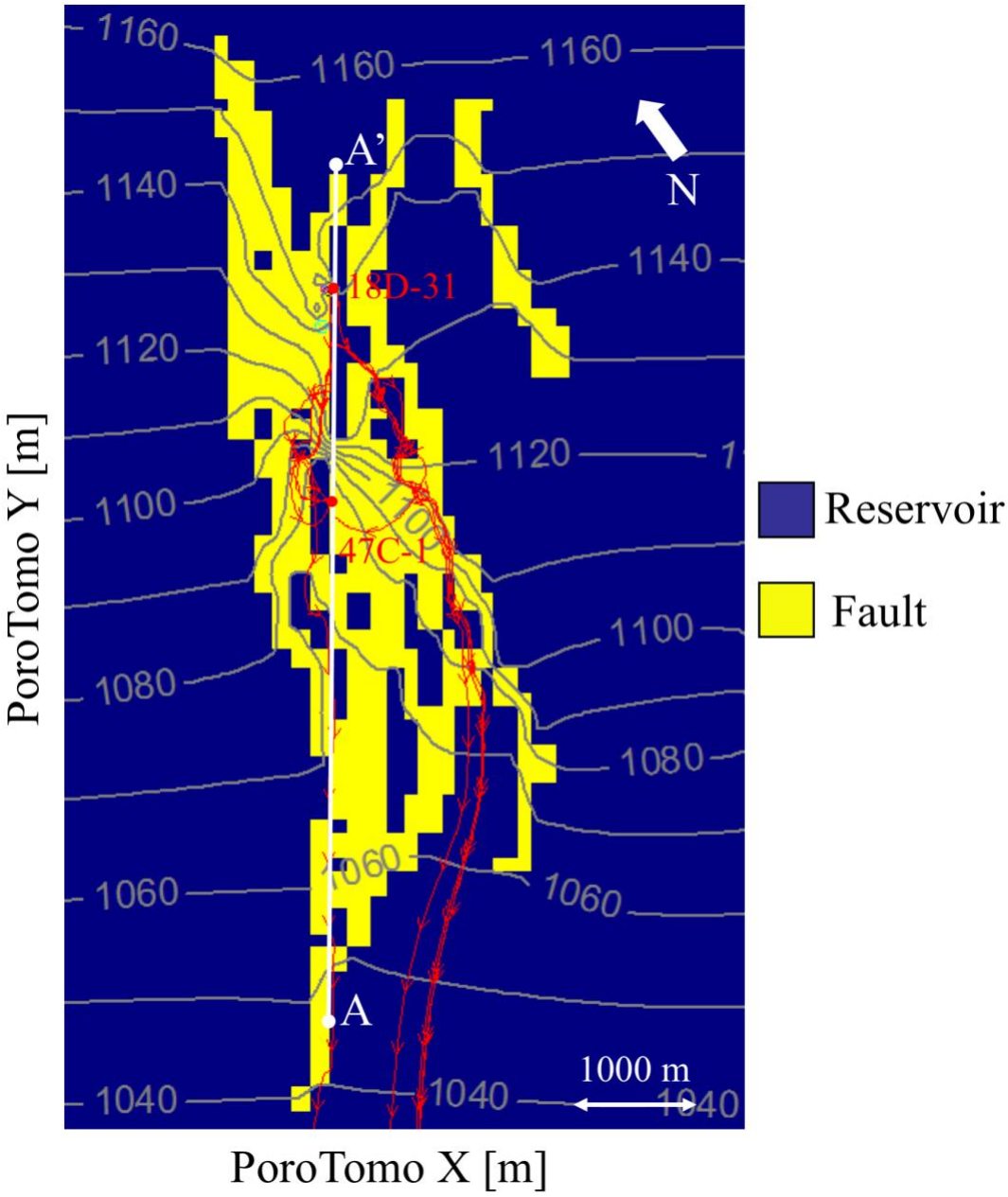

Figure 29: Steady-state hydraulic head distribution and advective flow paths using estimated parameters. Gray lines represent equipotentials. Red lines represent advective flow paths. Well 47C-1 projected up from depth to show location along section line.

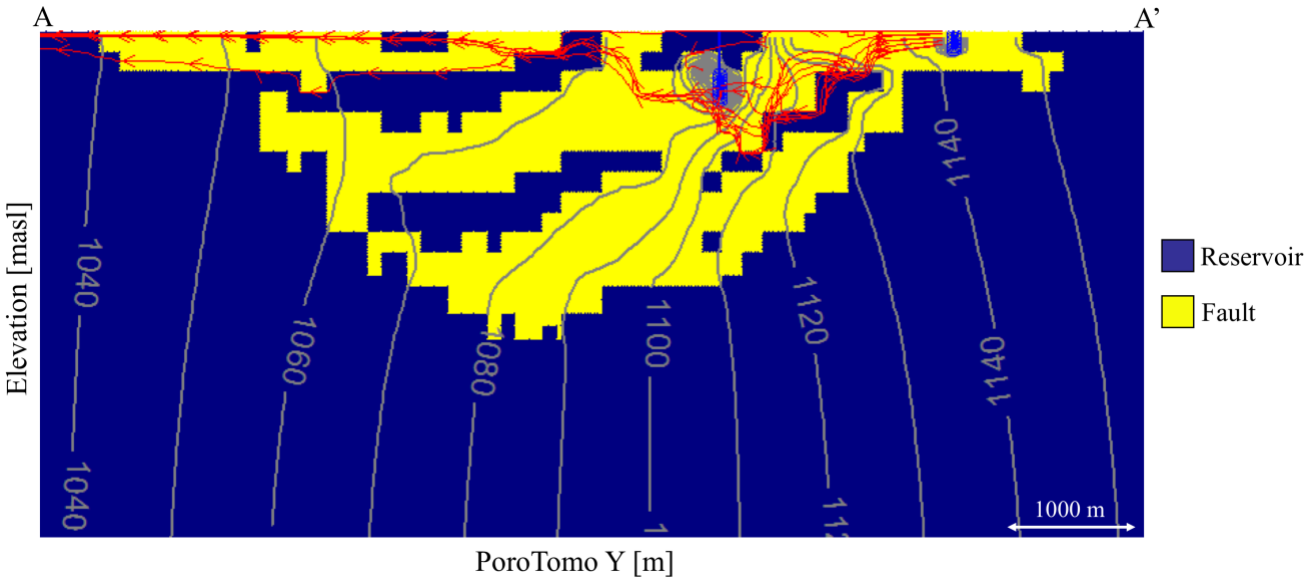

Figure 30: Strike-parallel cross section showing advective flow paths from injection well 18D-31 to production well 47C-1 and SW constant head boundary.

4.4.6.3. Faults Within Heterogeneous Porous Media

Table 8 shows estimated parameters and associated 95% confidence intervals for groundwater flow models using the conceptual model of faults within a heterogeneous porous media matrix, with zone 1 representing sedimentary units, zone 2 representing volcanic units, and zone 3 representing individual faults. Estimated fault hydraulic conductivity is two orders of magnitude lower than that of the volcanic zone and four orders of magnitude lower than that of the sedimentary zone. Specific storage estimates are within ranges expected for confined aquifer conditions in all models (Table 8). Increasing the heterogeneity of the reservoir rock from the conceptual model discussed above increased parameter uncertainty, primarily in the hydrologic zone representing sedimentary lithologies (Table 8).

Figure 31 shows observed and modeled pressure changes with optimal parameters for the model including 18 modeled faults. Simulated pressure changes provide best data

fit during early and late times, with degraded fit during early times at wells 56A-1 and 81B-1. SP-2 shows overall good fit at early times with decreasing data fit beginning at intermediate times and continuing through the time series.

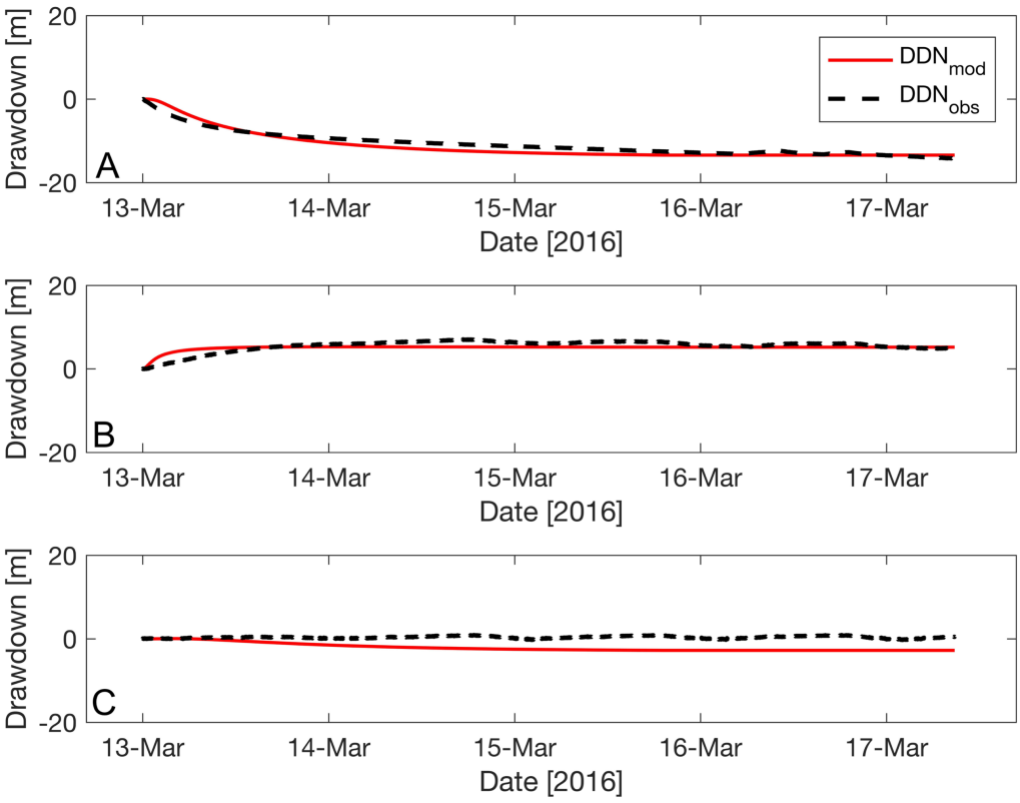

Figure 31: Modeled data fit at wells A) 56A-1, B)81B-1, and C) SP-2 using optimal parameters.

Table 9 shows that including all 64 identified faults in the flow model provides the best data fit, with MAE and Φ increasing as the number of modeled faults decreases. Decreasing the number of modeled faults from 64 to 18 shows that despite increasing data misfit, MAE is slightly above the expected data measurement error of $\pm$ 0.7 m drawdown at wells 81B-1 and 56A-1, indicating that groundwater flow is likely occurring along some smaller subset of faults. As seen above, decreasing the number of modeled faults from 18 to 15 produces a significant increase in MAE and Φ.

Table 8: Estimated model parameters and 95% confidence intervals obtained through inversion of pressure data using a conceptual model of georeferenced faults within a heterogeneous porous media. Parameter subscript indicates hydrologic zone number. Units of hydraulic conductivity are m/s and units of specific storage are m^{-1}.

All Faults (64 Faults)			
	Parameter Estimate	Lower Limit	Upper Limit
K_{sed}	4.1×10^{-2}	1.8×10^{-50}	9.4×10^{46}
$K_{volcanic}$	2.6×10^{-4}	4.2×10^{-6}	1.6×10^{-2}
K_{fault}	1.8×10^{-6}	1.0×10^{-6}	3.0×10^{-6}
Ss_{sed}	7.0×10^{-8}	1.2×10^{-300}	1.0×10^{0}
$Ss_{volcanic}$	4.7×10^{-5}	7.0×10^{-8}	3.1×10^{-2}
Ss_{fault}	1.5×10^{-6}	6.6×10^{-7}	3.3×10^{-6}
Primary, Secondary, and Tertiary Faults (28 Faults)			
	Parameter Estimate	Lower Limit	Upper Limit
K_{sed}	4.2×10^{-9}	4.7×10^{-40}	3.8×10^{22}
$K_{volcanic}$	4.3×10^{-4}	1.9×10^{-4}	1.0×10^{-3}
K_{fault}	1.4×10^{-6}	6.9×10^{-7}	3.0×10^{-6}
Ss_{sed}	2.0×10^{-4}	1.3×10^{-46}	1.0×10^{0}
$Ss_{volcanic}$	3.7×10^{-9}	4.3×10^{-27}	1.0×10^{0}
Ss_{fault}	1.8×10^{-6}	3.8×10^{-7}	8.3×10^{-6}
Primary and Secondary Faults (18 Faults)			
	Parameter Estimate	Lower Limit	Upper Limit
K_{sed}	6.8×10^{-8}	2.0×10^{-59}	2.3×10^{44}
$K_{volcanic}$	4.5×10^{-4}	1.6×10^{-4}	1.2×10^{-3}
K_{fault}	1.3×10^{-6}	7.3×10^{-7}	2.2×10^{-6}
Ss_{sed}	5.4×10^{-7}	1.6×10^{-116}	1.0×10^{0}
$Ss_{volcanic}$	1.2×10^{-7}	4.7×10^{-35}	1.0×10^{0}
Ss_{fault}	1.5×10^{-6}	1.8×10^{-8}	1.3×10^{-5}
Primary Faults (15 Faults)			
	Parameter Estimate	Lower Limit	Upper Limit
K_{sed}	1.8×10^{-4}	8.6×10^{-13}	1.4×10^{8}
$K_{volcanic}$	1.2×10^{-3}	7.8×10^{-18}	1.8×10^{11}
K_{fault}	6.4×10^{-7}	4.9×10^{-8}	8.3×10^{-6}
Ss_{sed}	1.6×10^{-6}	1.6×10^{-306}	1.0×10^{0}
$Ss_{volcanic}$	2.8×10^{-5}	8.7×10^{-13}	1.0×10^{0}
Ss_{fault}	1.9×10^{-7}	2.8×10^{-10}	1.3×10^{-4}

Table 9: Mean absolute error at each observation well and objective function value for optimal parameter estimates showing increasing model misfit as the number of modeled faults decreases.

All Faults (64 Faults)			
Well	56A-1	81B-1	SP-2
MAE [m]	0.8	0.7	1.4
Φ [m^2]	22.3		
Primary, Secondary, and Tertiary Faults (28 Faults)			
Well	56A-1	81B-1	SP-2
MAE [m]	0.9	0.8	1.9
Φ [m^2]	42.6		
Primary and Secondary Faults (18 Faults)			
Well	56A-1	81B-1	SP-2
MAE [m]	1.0	0.9	1.9
Φ [m^2]	38.4		
Primary Faults (15 Faults)			
Well	56A-1	81B-1	SP-2
MAE [m]	2.8	2.4	1.7
Φ [m^2]	127.6		

Figure 32 shows steady-state reservoir hydraulic head distribution – simulating normal plant operations – in plan view at an elevation of 1050 masl with optimal parameters using a conceptual model of 18 faults inside a heterogeneous porous media. MODPATH simulations show advective flow paths through the aquifer system, indicated by red lines with arrows indicating flow direction. Simulated flow paths follow identified fault traces throughout the reservoir from injection well 18D-31 (Figure 32). Most flow paths terminate at the SW constant head boundary, with one flow path captured by deeper production well 47C-1. Figure 33 shows a strike parallel cross-section along A - A' with red lines representing advective flow from well 18D-31 to the SW constant head boundary and an intermediate capture zone created by well 47C-1.

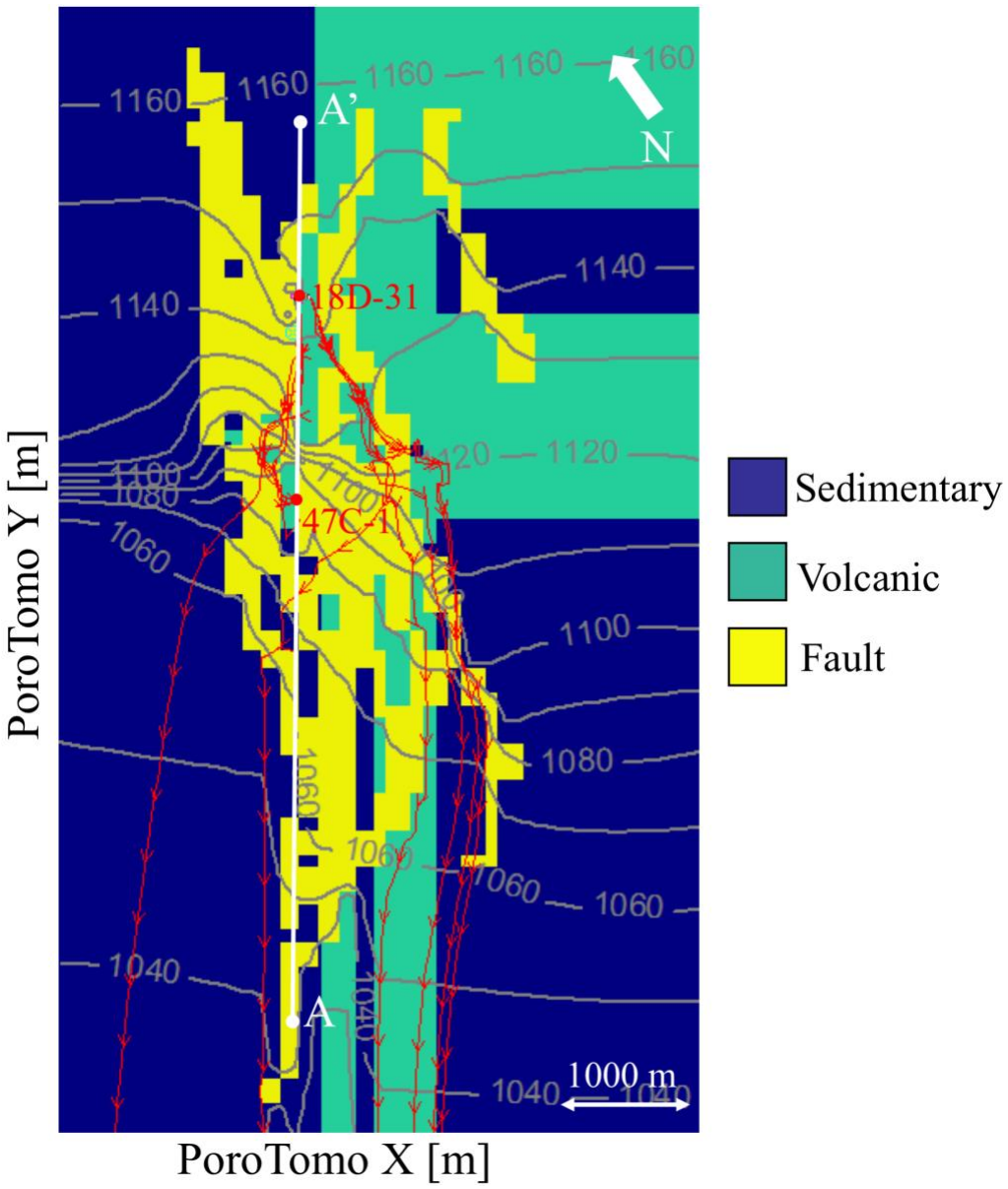

Figure 32: Steady-state hydraulic head distribution and advective flow paths using estimated parameters. Gray lines represent equipotentials. Red lines represent advective flow paths. Well 47C-1 projected up from depth to show location along section line.

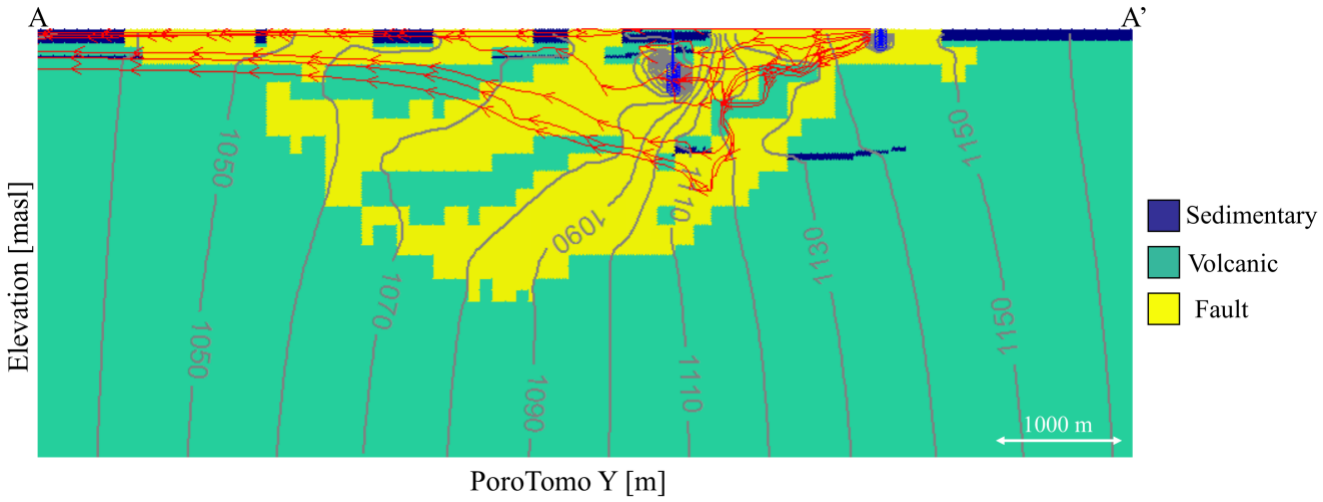

Figure 33: Strike-parallel cross section showing advective flow paths from injection well 18D-31 to production well 47C-1 and SW constant head boundary.

4.4.6.4. Faults and Damage Zone Within Homogeneous Porous Media

Table 10 shows estimated hydraulic properties and associated 95% confidence intervals for groundwater models with identified faults surrounded by a damage zone within a homogeneous porous media matrix. Zone 1 represents the homogeneous reservoir matrix, zone 2 represents identified faults, and zone 3 represents the damage zone surrounding the faults.

Estimated hydraulic conductivity with the model including only identified primary faults in the modeling domain indicates a low conductivity fault core surrounded by a damage zone with a conductivity that is five orders of magnitude greater than that of the fault core (Table 10). Parameter estimation produces an intermediate hydraulic conductivity value, three orders of magnitude greater than that of the faults, for the reservoir (Table 10). This estimated hydraulic conductivity distribution is consistent with the distribution pictured in Figure 25. Consistent with other specific storage estimates

across multiple conceptual models, specific storage estimates for this model indicate the confined conditions at Brady (Table 10).

Increasing the number of faults included in the modeling domain produced hydraulic conductivity estimates consistent with a low conductivity damage zone surrounding a fault core with a conductivity that is two orders of magnitude higher (Table 10). However, given the large uncertainty associated with the hydraulic conductivity estimates, indicated by the 95% confidence interval, specific conclusions cannot be drawn for the group of models with greater than 15 faults.

Figure 34 shows observed and modeled pressure changes with optimal parameters for the model including 15 modeled faults. Simulated pressure changes provide best data fit during late times, with decreased data fit during early and intermediate times at well 56A-1. SP-2 shows overall good fit at early times with decreasing data fit continuing through the time series, while 81B-1 shows good data fit throughout the entire time series (Figure 34).

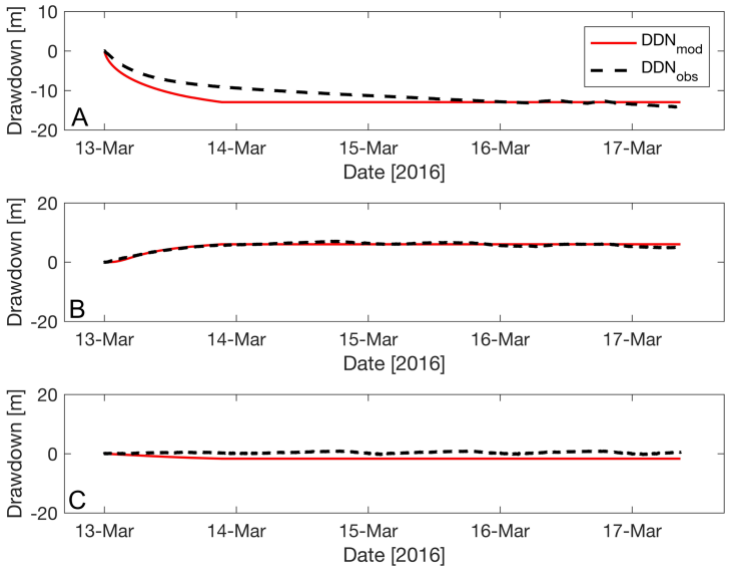

Figure 34: Modeled data fit at wells A) 56A-1, B)81B-1, and C) SP-2 using optimal parameters.

Table 10: Estimated model parameters and 95% confidence intervals obtained through inversion of pressure data using a conceptual model of a low conductivity fault core surrounded by a higher conductivity damage zone within a homogeneous porous media reservoir. Parameter subscript indicates hydrologic zone number. Units of hydraulic conductivity are m/s and units of specific storage are m^{-1}.

All Faults (64 Faults)			
	Parameter Estimate	Lower Limit	Upper Limit
K_{rock}	1.3×10^{-3}	2.3×10^{-10}	7.2×10^{5}
K_{fault}	1.7×10^{-5}	2.7×10^{-14}	1.0×10^{4}
K_{damage}	9.4×10^{-7}	1.3×10^{-15}	7.0×10^{2}
Ss_{rock}	6.4×10^{-8}	5.0×10^{-76}	1.0×10^{0}
Ss_{fault}	1.2×10^{-7}	1.1×10^{-39}	1.0×10^{0}
Ss_{damage}	5.1×10^{-7}	2.5×10^{-17}	1.0×10^{0}
Primary, Secondary, and Tertiary Faults (28 Faults)			
	Parameter Estimate	Lower Limit	Upper Limit
K_{rock}	3.2×10^{-3}	1.7×10^{-18}	5.8×10^{12}
K_{fault}	2.2×10^{-5}	3.1×10^{-10}	1.5×10^{0}
K_{damage}	6.1×10^{-7}	2.9×10^{-10}	1.3×10^{-3}
Ss_{rock}	1.3×10^{-7}	9.9×10^{-10}	1.5×10^{-5}
Ss_{fault}	2.4×10^{-7}	4.9×10^{-21}	1.0×10^{0}
Ss_{damage}	1.6×10^{-7}	1.7×10^{-12}	1.6×10^{-2}
Primary and Secondary Faults (18 Faults)			
	Parameter Estimate	Lower Limit	Upper Limit
K_{rock}	1.2×10^{-3}	1.9×10^{-24}	7.1×10^{17}
K_{fault}	1.4×10^{-5}	3.1×10^{-11}	6.7×10^{0}
K_{damage}	1.1×10^{-6}	3.7×10^{-12}	3.0×10^{-1}
Ss_{rock}	2.0×10^{-8}	9.8×10^{-181}	1.0×10^{0}
Ss_{fault}	5.5×10^{-7}	6.8×10^{-14}	1.0×10^{0}
Ss_{damage}	2.9×10^{-7}	1.5×10^{-7}	5.6×10^{-7}
Primary Faults (15 Faults)			
	Parameter Estimate	Lower Limit	Upper Limit
K_{rock}	4.8×10^{-4}	8.8×10^{-19}	2.6×10^{13}
K_{fault}	2.7×10^{-7}	3.1×10^{-8}	2.4×10^{-6}
K_{damage}	4.4×10^{-2}	4.5×10^{-5}	4.0×10^{1}
Ss_{rock}	1.1×10^{-7}	2.6×10^{-22}	1.0×10^{0}
Ss_{fault}	2.3×10^{-6}	7.6×10^{-8}	1.0×10^{0}
Ss_{damage}	8.1×10^{-7}	1.4×10^{-8}	4.8×10^{-5}

Table 11 shows MAE at each observation well and Φ for models with decreasing number of identified faults in the model domain. In contrast to conceptual models including only faults within the reservoir, model misfit decreases as the number of modeled faults and associated damage zone decreases (Table 11). Models containing 18 or more faults produced data misfit greater than expected data measurement error by more than a factor of two. The model with the fewest number of included faults shows a drastic improvement in data misfit with Φ decreasing by more than a factor of three and a significant decrease in MAE at wells 56A-1 and 81B-1 (Table 11).

Table 11: Mean absolute error at each observation well and objective function value for optimal parameter estimates showing decreasing model error as the number of modeled faults decreases.

All Faults (64 Faults)			
Well	56A-1	81B-1	SP-2
MAE [m]	3.2	2.3	1.8
Φ [m^2]	142.8		
Primary, Secondary, and Tertiary Faults (28 Faults)			
Well	56A-1	81B-1	SP-2
MAE [m]	2.7	2.4	1.9
Φ [m^2]	144.4		
Primary and Secondary Faults (18 Faults)			
Well	56A-1	81B-1	SP-2
MAE [m]	4	2	1.4
Φ [m^2]	181.8		
Primary Faults (15 Faults)			
Well	56A-1	81B-1	SP-2
MAE [m]	1.4	0.4	1.4
Φ [m^2]	27.2		

Figure 35 shows steady-state reservoir hydraulic head distribution – simulating normal plant operations – in plan view at an elevation of 1050 masl using optimal parameters using a conceptual model of 16 faults surrounded by a damage zone within a homogeneous porous media. MODPATH simulations show advective flow paths through

the aquifer system, indicated by red lines with arrows indicating flow direction. Simulated flow paths follow identified fault traces throughout the reservoir from injection well 18D-31 (Figure 35). Most flow paths terminate at the SW constant head boundary, with one flow path captured by deeper production well 47C-1. Figure 36 shows a strike parallel cross-section along A - A' with red lines representing advective flow from well 18D-31 to the SW constant head boundary and an intermediate capture zone created by well 47C-1.

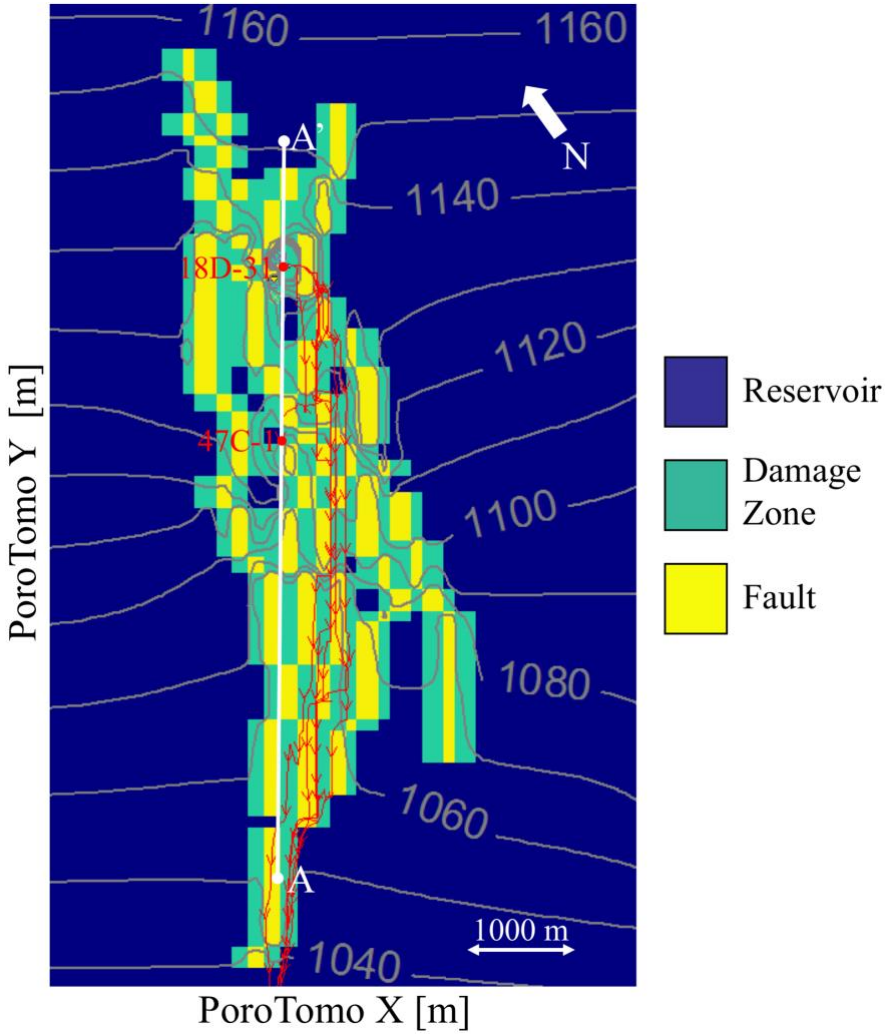

Figure 35: Steady-state hydraulic head distribution and advective flow paths using estimated parameters. Gray lines represent equipotentials. Red lines represent advective flow paths. Well 47C-1 projected up from depth to show location along section line.

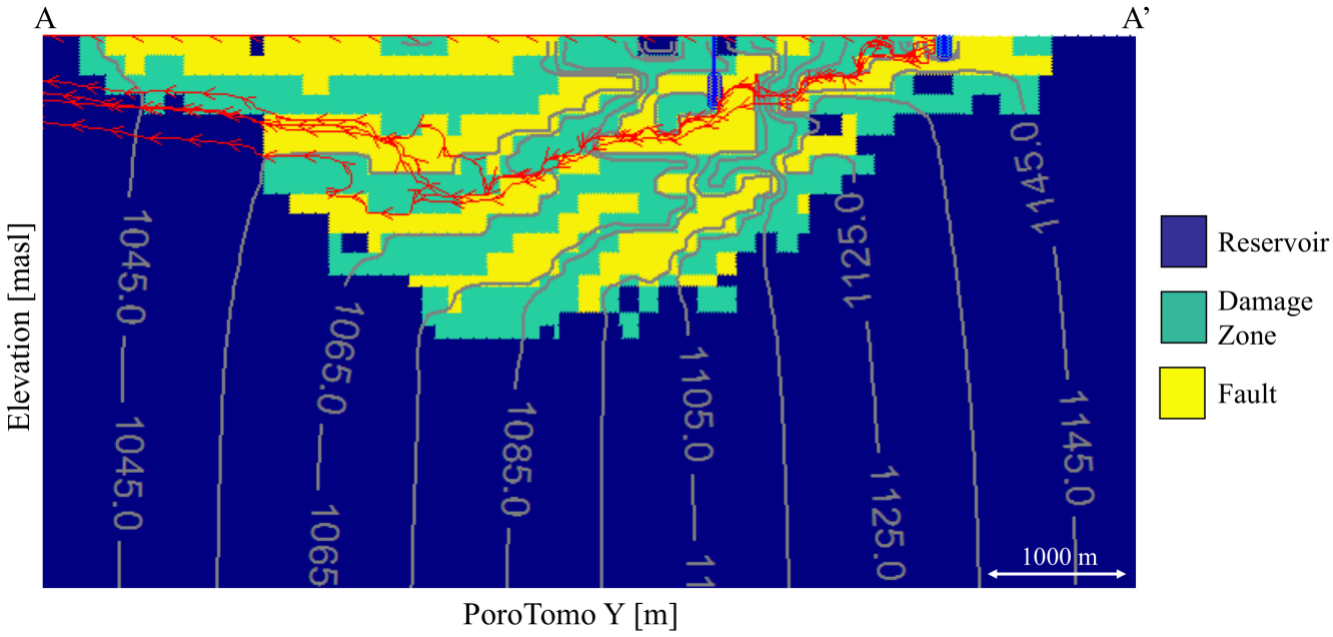

Figure 36: Strike-parallel cross section showing advective flow paths from injection well 18D-31 to production well 47C-1 and SW constant head boundary.

4.4.7. Discussion

The purpose of this numerical modeling was to determine a range of conceptual models that explain observed pressure responses at Brady during the PoroTomo field experiment using a zoned parameter estimation approach and to understand controls on groundwater flow throughout the Brady reservoir. Of the 15 conceptual models tested, 10 provided reasonable fits to observed pressure data. For the purposes of this analysis, MAE $\leq$ 1.4 m and $\Phi \leq 55$ m^2 is considered a reasonable fit, which are both approximately twice the expected data measurement error.

While there are a large number of conceptual models tested that provide reasonable fits to observed data, inversion results highlight the data sparsity at Brady and point to a need for more parameter constraints during inversion with increased geologic complexity. Across all conceptual models, increasing the geologic complexity beyond

two hydrologic zones produces parameter estimates with large uncertainty (i.e., 95% confidence intervals). The largest uncertainty exists in sedimentary geologic units found at depths similar to injection wells and well 18B-31. I attribute the large uncertainty observed in these shallower units to the fact that there is only one observation point at these depths recording reservoir pressure responses, which is not enough to provide adequate parameter constraints with increasing geologic complexity.

Jolie et al. [2015] developed an extensive 3-D fault model of the Brady reservoir, identifying and modeling 64 faults. Through inversion of collected pressure data, this modeling effort determined that not all of these faults are hydraulically active, that is, there is a critical subset of faults channeling fluids throughout the reservoir. While not every permutation was tested, this modeling effort indicates that the number of hydraulically active faults in the reservoir is on the order of 15 – 20.

Feigl and PoroTomo Team [2017] conceptualize that faults in the Brady reservoir channel fluids from the shallow reservoir to the deep reservoir where the water is heated by surrounding reservoir rock. Hydraulic conductivity estimates for conceptual models incorporating faults report estimated fault conductivities to be orders of magnitude lower than the surrounding reservoir rock, suggesting faults may be acting as a barrier to flow; however, advective transport simulations created using MODPATH demonstrate planar groundwater flow paths following fault traces. Simulated flow paths and parameter estimates are consistent with conceptual models reported by *Bense et al.* [2013], who discuss faults showing a conduit-barrier behavior where a low permeability fault core is surrounded by a high permeability damage zone creating fault-parallel groundwater flow,

consistent with observations at Brady and the conceptualization discussed by *Feigl and PoroTomo Team* [2017].

While a wide range of tested conceptual models provide reasonable fits to observed pressure data, when considering field observations, such as microseismicity, ground subsidence, and hydrothermal deposits, purely porous media and faults within a homogeneous reservoir do not provide the necessary complexity. Heterogeneous porous media conceptual models do not account for the spatial distribution of observed subsidence between injection and production wells at Brady, nor do they account for the linear surficial hydrothermal deposits following surface fault traces. Conceptual models incorporating faults within a homogeneous porous medium do not adequately explain spatial and temporal patterns observed in seismicity throughout Brady described by *Davatzes et al.* [2013] and *Cardiff et al.* [2018].

Given the field observations and observed pressure responses during the PoroTomo experiment, the most reasonable conceptual model incorporates identified faults within a heterogeneous porous medium. The lack of observed microseisimic events at shallower depths near injection wells, which intersect known faults, indicates shallow faults do not achieve the critical stress needed for slip. A combination of porous media flow in conjunction with fault-driven flow could explain the lack of pressure increases to the point of producing microseismic events.

CHAPTER 5

THERMAL SUSTAINABILITY

As discussed in earlier chapters, defining sustainability in the most general sense focuses on using a geothermal resource in a manner such that current energy needs are satisfied without comprising the ability of future populations to meet their energy needs [*Gro Harlem Brundtland et al.*, 1987]. *Axelsson et al.* [2005] quantifies sustainable geothermal development by defining a maximum production level, below which geothermal energy at a constant level can be maintained for a period of 100 – 300 years. This maximum production level is specific to individual reservoirs and selected production strategies; therefore, it is not a generalizable quantity. Ultimately, in this context, the sustainability of a geothermal reservoir is determined by comparing the rate of energy extraction to the rate of heat input from deep reservoirs, an energy flux that is poorly known without deep subsurface investigations.

While the definition put forth by *Axelsson et al.* [2005] provides a quantifiable manner by which to determine the sustainability of geothermal energy as a renewable resource, it does not consider economic factors that investors and operators use to determine production strategies and rates. Through the use of synthetic numerical simulations, *Lovekin* [2000] demonstrated that while larger capacity geothermal plants with aggressive production strategies show diminishing energy production over time, they benefit from economies of scale and provide a larger discounted return on investment (DROI) when compared to smaller capacity geothermal power plants with a constant energy production.

Given the increased present worth and DROI, many companies pursue aggressive production strategies when exploiting geothermal reservoirs. As such, the utility of a production strategy aimed at 100 – 300 year sustainability may not be financially feasible, especially if parasitic power losses are required to pump water from the reservoir. Often, operators become interested in decision making based on a range of reservoir lifetime projections under specified operating conditions based on reservoir characterization and numerical modeling simulations.

The remainder of this chapter focuses on simulated reservoir lifetime scenarios, which inform decisions operators must make during daily operations. To create these thermal lifetime scenarios, I developed a simple model that simulates reservoir temperature evolution, reservoir pressures, and power production in this reservoir under specified operating conditions and reservoir properties commonly determined during initial reservoir characterization. While the geometry and reservoir characterization results are loosely based on Brady, this modeling effort is not meant to serve as a predictor of reservoir lifetime for that specific geothermal system. Instead, the work in this chapter is meant to investigate, in a general sense, the contributors to financial sustainability of a geothermal reservoir over time and the impact of critical reservoir properties on this financial sustainability.

5.1. Thermal Sustainability Model

Building on the reservoir characterization efforts at Brady discussed in previous chapters, I developed a numerical model to simulate temperature evolution and power

generation of a synthetic geothermal reservoir through time. Reservoir geometry and physical properties are loosely based on Brady geometry and reservoir characterization results.

5.1.1. Conceptual Model

The developed model simulates thermal front movement through horizontal fractures connecting a perfectly re-circulating well doublet. Figure 37 shows the synthetic reservoir in cross-section with an example of two horizontal fractures connecting the injection and production well. The reservoir is simplified to consist of perfectly impermeable host rock, with a set of n different fractures each of the same aperture b. Hot water is removed from production wells at a specified volumetric flow rate (Q) and a temperature ($T(t)$) as dictated by thermal front movement. Cold water re-injection at a specified temperature (T_{inj}) occurs at the injection well a distance (L) from the production well. When a reservoir containing more than one fracture is considered, the total volumetric flow rate is assumed to be divided equally among the fractures.

While not fully consistent with actual geothermal operations, Q remains constant for the duration of the simulated time period. In reality, production and injection rates vary through time in response to water temperature entering the power plant, with the goal of maximizing water intake temperature, and therefore, energy production. To ensure mass balance through the system and simplify computations, $Q_{inj} = -Q_{prod}$, where positive Q indicates water injection into the aquifer.

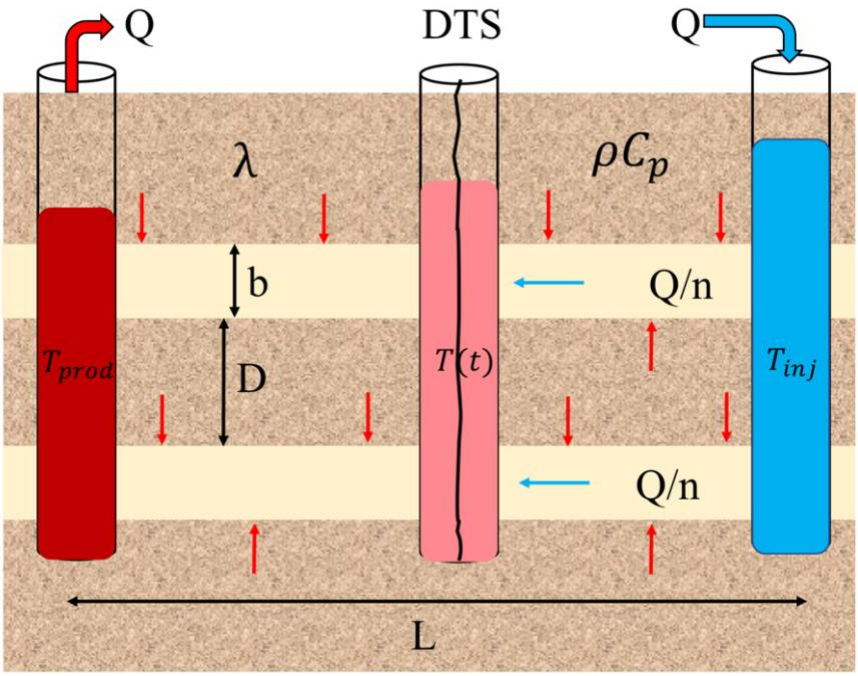

Figure 37: Conceptual model of a geothermal system consisting of a well doublet with a pumping well removing hot water and injection well re-injecting cold water after thermal energy is removed.

Consistent with geothermal power plant operations, injection water temperature (T_{inj}) remains constant throughout the simulations. Prior to production, the reservoir is assumed to be isothermal at a specified temperature, which represents the undisturbed steady-state reservoir temperature. In contrast, production water temperature ($T(t)$) decreases as a function of time, as the cold-water injection front moves from the injection well to the production well. Later sections discuss the methodology for determining production well temperatures through time.

Modeled fractures maintain a constant aperture (b) and extend horizontally through the reservoir connecting the injection and production wells. Given a lack of characteristic aperture data in the literature, fracture aperture is calculated using the cubic law given by equation 5.1

$$b = \left(\frac{12T\mu}{\rho_w g n}\right)^{\frac{1}{3}} \quad (5.1)$$

where:

b is fracture aperture in m

T is transmissivity in m^2/s

μ is dynamic viscosity in kg/(m s)

n is number of fractures in reservoir

This assumes that preliminary hydraulic characterization efforts have been conducted and plant operators have a sense of reservoir transmissivity and the number of fractures important for fluid and heat transport.

5.1.2. Mathematical Model

Simulated net power production through time provides a proxy to increase understanding the financial sustainability of a reservoir. I used a simple model that simulates the maximum power production from the reservoir at discrete times (which is dependent on the evolution of the temperature of extracted water) and power inputs required to extract water from the reservoir (which are dependent on head differences within the reservoir), using simple analytical approaches.

5.1.2.1. Power Computations

Net power production (P_{net}), the difference in generated power ($P_{produced}$) and parasitic power loss ($P_{consumed}$), provides the metric that determines the reservoir's financial sustainability. The reservoir is considered to be financially sustainable (i.e.,

profitable) while $P_{net} \geq 0$ MW, as this is the time when power production is greater than any parasitic power losses required to operate the plant. While all power plants have an installation capacity which limits their production, for the purposes of this analysis the model assumes an infinite power capacity.

$$P_{net} = P_{produced} - P_{consumed} \tag{5.1}$$

$$P_{produced} = Q\rho_w Cp_w \Delta T(t)\gamma_{plant} \tag{5.2}$$

$$P_{consumed} = Q\rho_w g\Delta h\gamma_{pump} \tag{5.3}$$

where:

Q is the volumetric flow rate in m^3/s

$\Delta T(t)$ is the water temperature difference in production and injection wells °C

Cp_w is the specific heat capacity of water in J / (kg °C)

ρ_w is density of water in kg/m^3

γ_{plant} is power plant energy conversion efficiency as a proportion of total water thermal energy

γ_{pump} is pump efficiency

g is acceleration due to gravity in m/s^2

Δh is the hydraulic head difference between the injection and production wells in m

Geothermal plant efficiency is affected by many factors, including turbine efficiency, generator efficiency, and heat losses occurring in the pipe during movement from production wells to the power plant [*Zarrouk and Moon*, 2014]. This simplified

model assumes that plant operators have an understanding of total power plant efficiency and does not consider individual efficiency factors.

Equation 5.3 shows that parasitic power loss considers the amount of power required to pump water from production wells due to the head difference between injection and production wells and frictional head losses occurring as water moves through pipes. This power loss calculation represents the minimum power necessary to overcome the head differences in a reservoir by pumping water from the production well.

5.1.2.2. Fracture Fluid Temperature Model

I simulated water temperature at the production well using the analytical solution developed by *Bödvarsson and Tsang* [1982]. This analytical solution simulates cold water front movement away from the injection well through horizontal fractures, assuming that flow within the fracture is steady and purely radial while the surrounding reservoir rock is considered impermeable. Horizontal heat conduction in the reservoir is neglected, and resistance to heat transfer between the reservoir and water is assumed to be negligible so that water temperature at the center of the fracture is in equilibrium with the rock/water interface [*Bödvarsson and Tsang*, 1982]. In the Laplace domain, the following expression gives water temperature (u) within the fracture:

$$u = \frac{1}{p}\exp\left(\frac{\left[\theta p + 2\sqrt{p}\,tanh\left(\sqrt{p}\right)\right]\xi}{2+\theta}\right) \tag{5.4}$$

$$\theta = \frac{\rho_f Cp_f b}{\rho_r Cp_r D} \tag{5.5}$$

$$\rho_f Cp_f = \eta\rho_w Cp_w + (1-\eta)\rho_r Cp_r \tag{5.6}$$

$$\xi = \frac{\lambda \pi r^2 (2+\theta)}{QD\rho_w Cp_w} \tag{5.7}$$

where:

p is the Laplace parameter

θ is a dimensionless energy potential given by equation 5.5

b is the fracture aperture in m

D is the fracture half-spacing in m

ξ is a dimensionless distance given by equation 5.7

λ is the thermal conductivity in W / (m °C)

η is the porosity

$\rho_f Cp_f$ is the fracture volumetric heat capacity in J / (m^3 °C)

$\rho_r Cp_r$ is the reservoir rock volumetric heat capacity in J / (m^3 °C)

A numerical algorithm developed by *De Hoog et al.* [1982] inverts for the Laplace parameter that simulates non-dimensional water temperature ($T_D(t)$) in the time domain. Rearranging equation 5.8 provides simulated temperature of water extracted at the production well as a function of time

$$T_D(t) = \frac{T(t) - T_0}{T_{inj} - T_0} \tag{5.8}$$

where:

T_0 is initial production well water temperature in °C

T_{inj} is the injection water temperature in °C

$T(t)$ is production well water temperature at a given time °C

5.1.2.3. Hydraulic Power Losses

Parasitic power losses are related to head differences between the injection and production wells. To simulate these head differences, I employed a simple analytical solution (Equation 5.9) derived by *Haitjema* [1995] that simulates the discharge potential throughout the reservoir created by an injection and production well-doublet.

$$\Phi(x,y) = \frac{Q}{4\pi}\ln\left(\frac{\left(x - x_{prod}\right)^2 + \left(y - y_{prod}\right)^2}{\left(x - x_{inj}\right)^2 + \left(y - y_{inj}\right)^2}\right) + \Phi_0 \tag{5.9}$$

$$h(x,y) = \frac{\Phi}{T} \tag{5.10}$$

where:

$\left(x_{prod}, y_{prod}\right)$ are the spatial coordinates of the production well in m

$\left(x_{inj}, y_{inj}\right)$ are the spatial coordinates of the injection well in m

(x,y) are the spatial coordinates of the point of interest in the reservoir in m

Φ_0 is a specified discharge potential at a specified point in the reservoir in m^2/s

T is reservoir transmissivity in m^2/s

Hydraulic head ($h(x,y)$) is simulated at the borehole walls of the injection and production wells using equations 5.9 and 5.10, with the assumption that this is representative of the head within the borehole. Equation 5.11 gives the total head difference (Δh) used to determine the parasitic power loss (Equation 5.3).

$$\Delta h = \left(h_{inj} - h_{prod}\right) + h_{loss} \tag{5.11}$$

The Darcy-Weisbach equation (5.12) calculates frictional head losses (h_{loss}) as water moves through pipes [*Hibbeler*, 2014].

$$h_{loss} = f\left(\frac{L}{2r}\right)\left(\frac{V^2}{g}\right) \tag{5.12}$$

where:

f is the friction factor [-]

L is pipe length in m

r is pipe inner radius in m

V is water velocity in m/s

The friction factor (f) is commonly determined using a Moody Diagram or some other variation. Multiple expressions have also been developed to calculate the friction factor. I used the Colebrook Equation (5.13) to estimate f [*Hibbeler*, 2014].

$$\frac{1}{\sqrt{f}} = -2\ln\left(\frac{\frac{\epsilon}{D}}{3.7} + \frac{2.51}{Re\sqrt{f}}\right) \tag{5.13}$$

Because equation 5.13 is not an explicit expression for f, I took an iterative approach to determine f by using the Matlab library function, *fminearch*, to minimize the difference between the left and right sides of the Colebrook equation.

$$Re = \frac{\rho_w V D}{\mu} \tag{5.14}$$

where:

ϵ is the pipe roughness coefficient in m

Re is the dimensionless Reyonlds number

μ is dynamic viscosity in kg/(m s)

5.2. Simulated Power Production

To understand the effects of reservoir parameters on the financial sustainability of the synthetic reservoir, I conducted a sensitivity analysis, varying reservoir parameters individually by $\pm$ 20 % and simulation net power production over a 30-year time period. This is a common time period for studies of geothermal reservoir performance from an economical perspective. While longer simulations covering longer periods of time may be informative, they are not necessarily realistic as they go beyond the lifetime of power production equipment (e.g., pumps, turbines, generators, etc…) and do not account for the current environment of rapid technological advancement improving power production efficiencies. Similarly, in most exploited geothermal reservoirs, changes to operations and infrastructure are common beyond a 30-year timeframe.

Table 12: Reservoir property inputs used to simulate net geothermal power production in a synthetic reservoir over a period of 30 years.

Thickness	500 [m]	$\boldsymbol{\lambda}$	0.03 [W/(m ℃)]
$\boldsymbol{n}$	20	$\boldsymbol{\rho_r}$	2500 [kg/m^3]
$\boldsymbol{L}$	2000 [m]	$\boldsymbol{Cp_r}$	1000 [J/(kg ℃)
$\boldsymbol{\rho_w}$	1000 [kg/m3]	$\boldsymbol{T_{inj}}$	80℃
$\boldsymbol{Cp_w}$	4000 [J/(kg ℃)]	$\boldsymbol{T_0}$	175℃
$\boldsymbol{T}$	0.013 [m^2/s]	$\boldsymbol{\epsilon}$	4.5 x 10^{-5} [m]
$\boldsymbol{Q}$	0.5 [m^3/s]	$\boldsymbol{\gamma_{pump}}$	1%
$\boldsymbol{\mu}$	2.5 x 10^{-4} [kg/(m s)]	$\boldsymbol{\gamma_{plant}}$	10%

Table 12 shows the input parameters used in the following temperature and net power production simulations. The simulations assume that a power plant has been established at the reservoir, initial reservoir characterization has been conducted, and power production is underway. Parameters such as λ, ρC_p, T, T_0, and γ_{plant} would come from initial reservoir characterization and early production data, whereas production rates

and injection temperature are specified based on reservoir conditions and the type of energy extraction system installed (i.e., single flash, dual flash, binary). Pipe roughness factors (ϵ) are tabulated across many fluid mechanics textbooks, websites dedicated to engineering information, and throughout the literature. Tables in *Hibbeler* [2014] provide the chosen roughness coefficient for new commercial steel. The roughness coefficient remains constant throughout these simulations; however, this coefficient will increase during plant operations as geothermal brine causes scaling along the pipe.

Water density is temperature and pressure dependent; therefore, it likely changes with temperature and pressure decreases with power production. Despite this expected change, water density is held constant throughout the simulation. Figure 38 shows that while water density changes early time power production by approximately 1 MW, late time power production converges to approximately equivalent values across a range of reasonable density values.

To ensure that the most cost prohibitive scenario is considered, I chose a 1% efficiency for pumps that remove water from the production well, move water through the power plant to the injection well, and then re-inject water at the injection well. This efficiency accounts for a greater power input requirement than power provided by the pumps. Figure 39 shows that the difference between a perfectly efficient pump and the chosen 1% efficient pump differs by approximately 0.5 MW, implying pump efficiency exerts minimal impacts on parasitic power losses and reservoir financial sustainability.

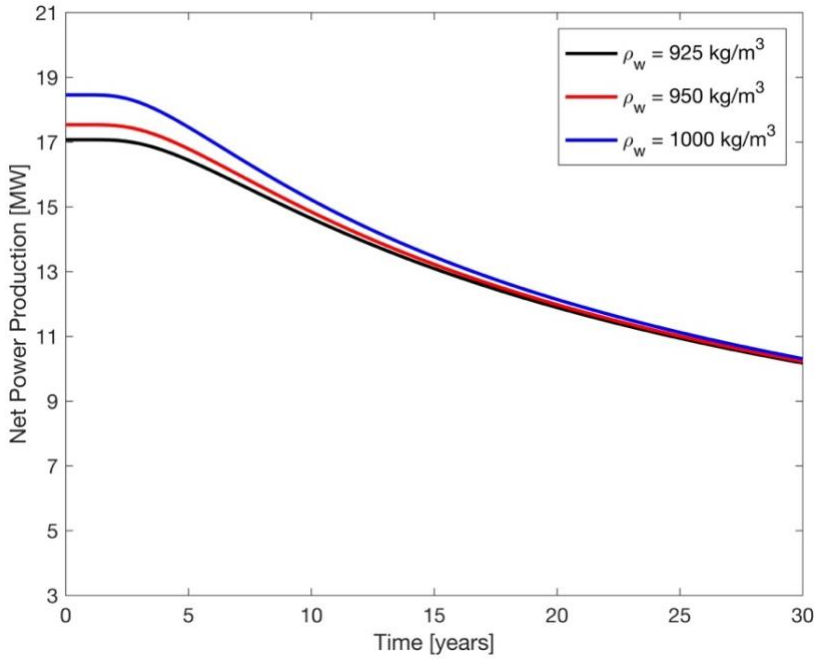

Figure 38: Net power production through time showing changes in power production across a reasonable range of water density values.

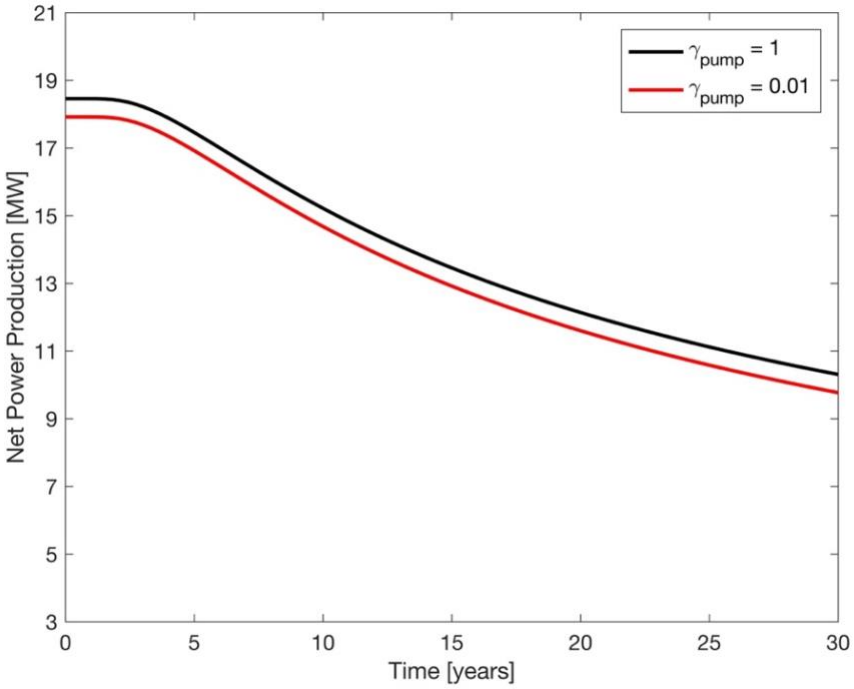

Figure 39: Net power production with perfectly efficient and 1% efficient pumps that move water throughout the power plant illustrating the minimal impact that pump efficiency has on parasitic power losses and overall reservoir financial sustainability.

5.2.1. Reservoir Thermal and Hydraulic Properties

Thermal conductivity controls the ease with which heat diffuses through the reservoir against a temperature gradient. Figure 40 shows changes in thermal drawdown and simulated net power production over a period of 30 years in response to increases and decreases in base case thermal conductivity. Increasing and/or decreasing thermal conductivity by 20% shows no effect on early time net power production or water temperature; however, later time net power production differs by less than 1 MW and water temperature varies by 3°C in both directions (Figure 40).

Declines in net power production and thermal begin earlier with lower thermal conductivity, whereas higher thermal conductivity shows a later onset of decline (Figure 40). Despite the difference in timing of thermal drawdown and power production decline, the rate of the decline remains constant with changes in thermal conductivity. Net power production remains > 0 MW throughout the 30-year simulation period, with 15 MW being the minimum simulated net power production (Figure 40).

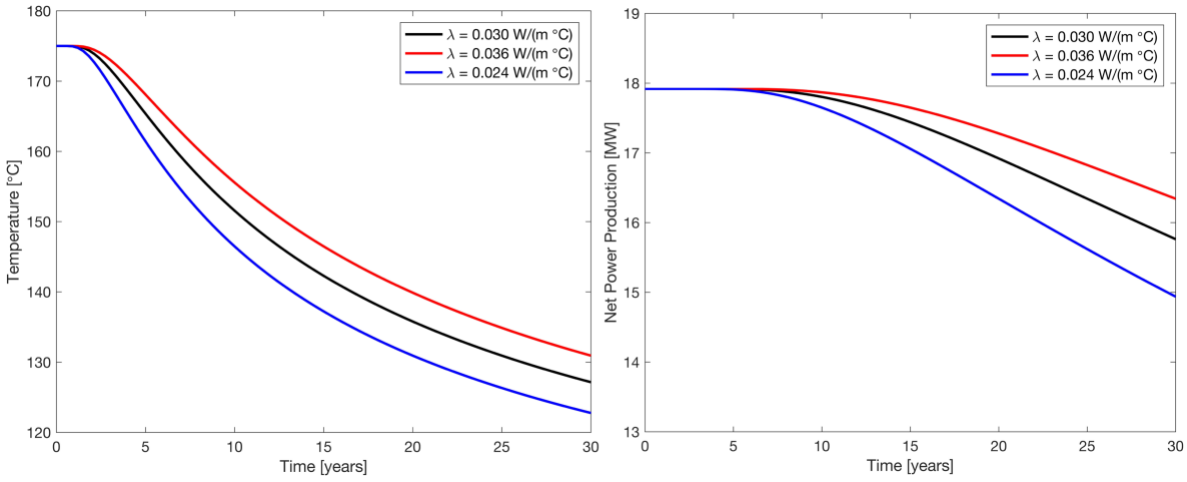

Figure 40: Simulated thermal drawdown (left) at a point midway between injection and production wells and simulated net power production (right) for a period of 30 years with variable thermal conductivity values.

Volumetric heat capacity quantifies the amount of energy input or loss required to change a unit reservoir volume by 1℃. Figure 41 shows simulated thermal drawdown and net power production with volumetric heat capacity increased and decreased by 20% from the base case value given in Figure 41. Changing volumetric heat capacity has no effect on early time power production or water temperature; however, late time water temperature varies by 3°C and power production differs from the base case parameter values by less than 1 MW in either direction (Figure 41).

Declines in power production and water temperature begin later with an increased volumetric heat capacity, whereas power production and water temperature decline onsets occur earlier with the lower volumetric heat capacity value (Figure 41). Simulated net power production remains > 0 MW throughout the entire simulation period, and the minimum simulated power production is approximately 9 MW.

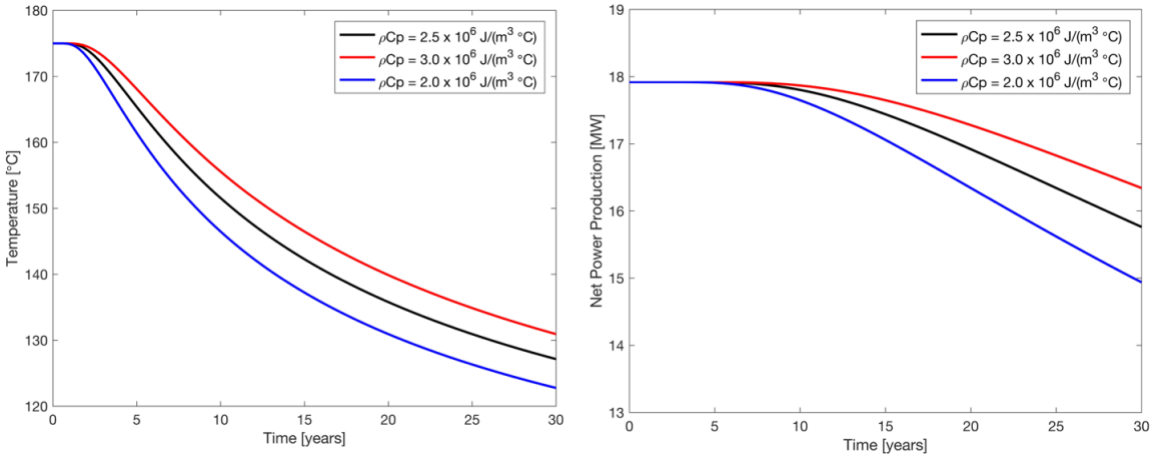

Figure 41: Simulated thermal drawdown (left) at a point midway between injection and production wells, and simulated net power production (right) for a period of 30 years with variable volumetric heat capacity values.

Like hydraulic conductivity, transmissivity ($T = Kb$) is a measure of how easily water moves through, in this case, fractures within a geothermal reservoir. Figure 42 shows thermal drawdown and simulated power production over a period of 30 years in

the synthetic reservoir with transmissivity increased and decreased by one order of magnitude from the base case transmissivity (Table 12). Because hydraulic conductivity varies over a wide range of magnitudes, changing transmissivity by 20% was not a large enough change to understand its effect on power production. Given that fracture aperture is calculated for a given transmissivity, I allowed aperture to vary with changes in transmissivity to maintain internal consistency.

Changes in transmissivity do not change the timing or rate of water temperature or power production decline throughout the simulation. Simulated production curves mirror each other, with a vertical shift up or down depending on the transmissivity used for the simulation (Figure 42). Water temperature remains identical across all three values of transmissivity considered; however, net power production shows wide variation at the end of 30 years with a 6 MW minimum and 18.5 MW maximum power production (Figure 42).

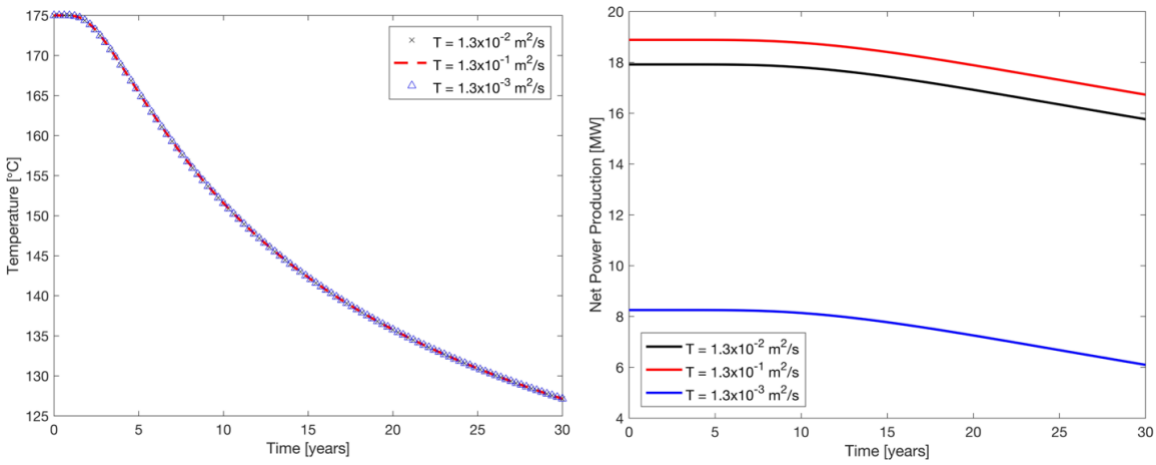

Figure 42: Simulated thermal drawdown (left) at a point midway between injection and production wells and simulated net power production (right) over a period of 30 years with transmissivity varying over two orders of magnitude.

5.2.2. Reservoir Fracture Properties

While many geothermal reservoirs occupy highly faulted and fractured areas, not all faults are critical for water and heat transport. Figure 43 shows simulated thermal drawdown and power production for a 30-year period with the number of fractures used for heat transport changed by 20% from the base case in both directions. Because transmissivity is held constant as the number of fractures vary, by necessity fracture aperture will vary as the number of fractures are changed to maintain the base case transmissivity value. Increasing and decreasing the number of fractures available for heat transport from the base case scenario increases and decreases power production by approximately 2 MW and water temperature by 9 °C, respectively, at the end of the 30-year simulation period.

Increasing the number of fractures also increases the time before the onset of decreased power production and decreases the rate at which power production decreases compared to the base case scenario (Figure 43). In contrast, decreasing the number of fractures decreases the amount of time before power production begins to decline and increases the rate at which power production declines (Figure 43).

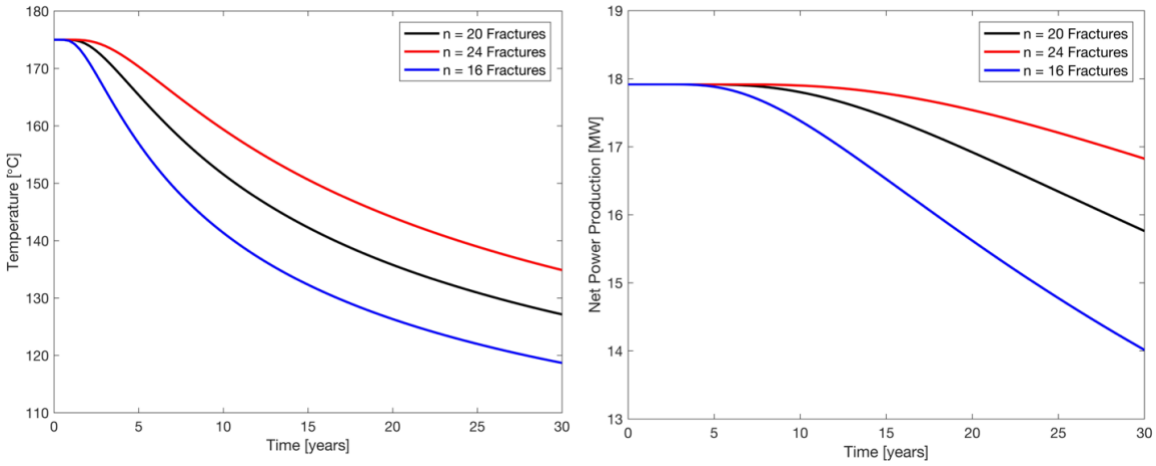

Figure 43: Simulated thermal drawdown (left) at a point midway between injection and production wells and simulated net power production (right) for a period of 30 years with variable number of fractures in the reservoir.

5.3. Discussion

Figure 43 shows the least thermal drawdown and highest sensitivity to increased net power production at the end of the 30-year simulation in the scenario with the most fractures. Increased power production and decreased thermal drawdown occur as a result of two things. First, increasing the number of fractures increases the water-rock contact area available for heat transfer. Second, fluid velocity through individual fractures decreases as the number of fractures increases; therefore, there is an increase in residence time of water in the fractures allowing increased heat transfer. This, of course, assumes the total volumetric flow rate is divided evenly among individual fractures.

This increased sensitivity to the number of fractures is consistent with the study performed by *Li et al.* [2016], which found greatest net present value in simulations that contained the most number of stimulations. While their study targets enhanced

geothermal systems (EGS), their result is consistent in that the number flow paths (i.e., fractures) increases as the number of the enhanced flow paths increases.

Figure 42 shows the increased sensitivity net power production exhibits in response to changes in transmissivity; however, thermal drawdown displays no sensitivity to transmissivity changes assuming Q is held constant. Thermal drawdown changes in response to changing transmissivity would occur as a result of individual fracture aperture changes. Given that water temperature shows no sensitivity to transmissivity, parasitic power consumption controls the changes seen in net power production. Varying transmissivity over two orders of magnitude varies the head gradient between injection and production wells, and thus input power required to pump water for energy production and then pump the cooled water for re-injection.

As the ratio of thermal conductivity and volumetric heat capacity (i.e., thermal diffusivity) provides the primary control on heat diffusion through the reservoir, it is expected that varying either parameter by the same amount would yield identical thermal front and power production curves as illustrated in Figure 40 and Figure 41. Lab studies show that expected values of thermal diffusivity show little variability within a given rock type; therefore, it is reasonable to assume a homogenous thermal conductivity in a given lithology for modeling and prediction purposes [*Robertson*, 1988]. Given the low sensitivity of power production to thermal properties and low variability in thermal properties in a given lithology, monitoring temperature at a central point, as seen at Brady and simulated here, likely is useful for providing evidence of thermal breakthrough over time and further characterizing the expected number of fractured flow paths.

One possible critique of this analysis is that the chosen thermal conductivity is lower than reported lab values. The chosen input value for this parameter represents a bulk thermal conductivity that is representative of what plant operators would acquire through thermal characterization efforts. This bulk value averages the thermal conductivity of reservoir rocks as well as any fluids (gas being considered a fluid in non-water dominated systems) present within the system. *Clauser and Huenges* [2013] have shown that thermal conductivity shows a marked decrease with increasing volumetric water content due to fluids having larger thermal conductivity values, which become averaged in bulk measurements. They also go further to show that thermal conductivity exhibits a temperature dependence, decreasing with increasing temperature, which is consistent with previous lab results reported by *Robertson* [1988].Given these results, I argue that the chosen thermal conductivity for this analysis is reasonable and provides reasonable power production simulations.

While these simulations demonstrate reservoir sensitivity to common physical properties, it should be noted that this model as a predictive tool most appropriately simulates geothermal systems that have been producing for a period of time, such as Brady, and reservoir lifetime is becoming a concern. Geothermal systems in the exploration or early production stage that are subject to more aggressive non-constant production strategies could benefit from this model by using it to determine where exploration and characterization efforts are best focused to enhance the financial sustainability of the reservoir.

CHAPTER 6

CONCLUSIONS

6.1. Conclusions

This thesis presented an analytical model that simulates power production through time to predict thermal, and thus financial, sustainability of a geothermal reservoir. Chapters 3 and 4 presented thermal and hydraulic characterization results using data collected during an extensive field experiment at an active geothermal site. These characterization efforts and the estimated reservoir properties they produce mirror the data analysis that future plant operators may undertake to determine input parameters for the power production model presented in Chapter 5. A sensitivity analysis was conducted using the developed power production model to understand what reservoir properties exert the largest controls on reservoir performance over a period of 30 years.

Thermal characterization results show low variability in thermal diffusivity estimates within individual lithologic units. These findings are consistent with lab measured thermal properties reported by *Clauser and Huenges* [2013] and *Robertson* [1988], which state that expected values for thermal properties for specific rock types vary over a small range. This result illustrates that treating individual rock units with homogeneous thermal properties in simple analytical models is appropriate. Considering the more applied aspect of these findings, the low variability of thermal properties indicates that applying thermal characterization results across a reservoir using spatially sparse data is likely sufficient for predicting future reservoir performance.

The hydraulic characterization presented in Chapter 4 illustrated that the confidence intervals obtained through linearized error analysis produce near infinite parameter uncertainty with conceptual models including more than two hydrologic zones. The parameters with the largest uncertainty occur in shallower hydrologic zones where pressure responses are recorded in only one observation well. This uncertainty points to the need for additional stress periods, hence a different reservoir response, during inversion, and more pressure observation locations.

Sensitivity analysis conducted in Chapter 5 showed that transmissivity exerts a large control on pressure differences between the injection and production wells, which is the main input when determining a geothermal plant's parasitic power losses. Figure 42 shows the effect of varying transmissivity by one order of magnitude and highlights the anticipated effect on net power production simulations. Given that hydraulic conductivity, and thus transmissivity, varies over many orders of magnitude, these simulations point to the need for reduced hydraulic conductivity uncertainty obtained through inversion of pressure data.

The Brady geothermal field has 64 identified faults that have been cataloged and presented in an extensive 3-D modeling effort [*Jolie et al.*, 2015]. The range of conceptual models used for hydraulic characterization that incorporate faults into the model domain point to a small subset of those faults that are hydraulically active. This is a critical result as the sensitivity analysis presented in Chapter 5 shows that the number of hydraulically active faults in a reservoir produces the largest effect on thermal drawdown, which is in agreement with an optimization study and sensitivity analysis conducted by *Li et al.* [2016].

6.2. Future Work

The results of the sensitivity analysis point to the need for increased focus on understanding how many fractures or faults within a reservoir are hydraulically active and, thus, critical for heat transport. This result indicates the need to prioritize understanding the number of hydraulic pathways during initial exploration or ongoing characterization efforts. As conventional tracer testing only gives an indication of connectivity between wells and driller's logs only identify the number of faults and/or fractures present intersected by a given well, a significant challenge for future researchers is methods development aimed at delineating the number of fast flow pathways within a reservoir. Techniques for imaging tracer movements – such as combined tracer-geophysical experiments – represent one possible approach to constraining this critical parameter.

A promising area for future work lies in reducing estimated hydraulic conductivity uncertainty. This could be achieved by extending the current groundwater flow models by adding a third stress period that would simulate the pressure response during increased infield injection. Due to poor record keeping of injection flow rates, mass balance issues arose during analysis of the pumping data during this portion of the PoroTomo field experiment, representing a major problem with this approach. The mass balance discrepancy encountered during data analysis points to the need for more careful flow rate monitoring during geothermal operations.

Future studies looking to minimize parameter uncertainty during inversion should thoughtfully consider instrument placement during experiment planning. This study

would have benefitted from pressure data in one additional observation well at depths accessed by injection wells. As well drilling and pressure sensors built to withstand harsh conditions at geothermal sites are costly investments, adequate data coverage will continually present a challenge during reservoir characterization efforts. The challenge presented by data sparsity could be circumvented by expanding the hydraulic characterization presented in Chapter 4 by incorporating past hydraulic conductivity estimates into the current groundwater flow models as pilot points. These pilot points would serve as an additional constraint along with observed pressure responses during inversion.

The power production model presented in Chapter 5 defines the financial sustainability of a geothermal reservoir as the point at which net power production equals 0, as this is the point when parasitic power and produced power are equal; however, this is an oversimplified view of the financial sustainability of these systems. This limitation in the model can be addressed in future work by using current market values to determine income from power sold and costs incurred from power consumption. Simple models could also be added to consider annual operating and maintenance costs. These additions would quantify the current model in a financial sense and provide added benefit to the financial sustainability discussion.

The developed analytical model simulates power production assuming a constant production rate through time, making it a useful tool for established geothermal fields where reservoir lifetime is becoming a concern. This model could be extended to simulate other more aggressive initial production strategies, diminishing with time, consistent with analyses presented by *Lovekin* [2000]. This added flexibility would allow

for longer-term predictions of reservoir performance under various operating conditions, allowing operators to decide the optimal production strategy to pursue.

Monitoring temperature in geothermal fields is commonly conducted at discrete times by lowering and raising a probe through the borehole. The thermal characterization presented in Chapter 3 illustrates the utility of deploying fiber-optic distributed temperature sensing (DTS) technology to record reservoir temperature more continuously. One drawback to this technology is signal degradation, thus accuracy, of the instrument due to long term exposure in harsh environments. Future work during initial site exploitation could investigate ways to incorporate these cables into well casings as a means of instrument protection following the work of *Reinsch et al.* [2013]. Increasing use of this technology would also benefit from future work aimed at innovative shielding materials that serve as a protective barrier following initial investigations by *Reinsch and Henninges* [2010].

REFERENCES

Ali, S., J. Akerley, E. Baluyut, M. Cardiff, N. Davatzes, K. Feigl, W. Foxall, D. Fratta, R. Mellors, and P. Spielman (2016), Time-series analysis of surface deformation at Brady Hot Springs geothermal field (Nevada) using interferometric synthetic aperture radar, *Geothermics*, *61*, 114-120.

Anderson, M. P., W. W. Woessner, and R. J. Hunt (2015), *Applied groundwater modeling: simulation of flow and advective transport*, Academic press.

Aster, R. C., B. Borchers, and C. H. Thurber (2011), *Parameter estimation and inverse problems*, Academic Press.

Axelsson, G. (2010), Sustainable geothermal utilization–Case histories; definitions; research issues and modelling, *Geothermics*, *39*(4), 283-291.

Axelsson, G., V. Stefánsson, G. Björnsson, and J. Liu (2005), Sustainable management of geothermal resources and utilization for 100–300 years, paper presented at Proceedings World Geothermal Congress.

Bense, V., T. Gleeson, S. Loveless, O. Bour, and J. Scibek (2013), Fault zone hydrogeology, *Earth-Science Reviews*, *127*, 171-192.

Bense, V., T. Read, O. Bour, T. Le Borgne, T. Coleman, S. Krause, A. Chalari, M. Mondanos, F. Ciocca, and J. Selker (2016), Distributed Temperature Sensing as a downhole tool in hydrogeology, *Water Resources Research*, *52*, 9259 - 9273.

Bodvarsson, G. (1972), Thermal problems in the siting of reinjection wells, *Geothermics*, *1*(2), 63-66.

Bödvarsson, G. S., and C. F. Tsang (1982), Injection and thermal breakthrough in fractured geothermal reservoirs, *Journal of Geophysical Research: Solid Earth*, *87*(B2), 1031-1048.

Cardiff, M., et al. (2018), Geothermal production and reduced seismicity: Correlation and proposed mechanism, *Earth and Planetary Science Letters*, *482*, 470-477.

Clauser, C., and E. Huenges (2013), Thermal Conductivity of Rocks and Minerals, in *Rock Physics & Phase Relations*, edited.

Coleman, T. I. (2016), PoroTomo DTS Raw Data, edited, https://gdr.openei.org/submissions/853.

Coleman, T. I., B. L. Parker, C. H. Maldaner, and M. J. Mondanos (2015), Groundwater flow characterization in a fractured bedrock aquifer using active DTS tests in sealed boreholes, *Journal of Hydrology*, *528*, 449-462.

Davatzes, N. C., K. L. Feigl, R. J. Mellors, W. Foxall, H. F. Wang, and P. Drakos (2013), Preliminary investigation of reservoir dynamics monitored through combined surface deformation and micro-earthquake activity: Brady's geothermal field, Nevada, paper presented at Proceedings of the Thirty-Eighth Workshop on Geothermal Reservoir Engineering, Stanford, California.

De Hoog, F. R., J. Knight, and A. Stokes (1982), An improved method for numerical inversion of Laplace transforms, *SIAM Journal on Scientific and Statistical Computing*, *3*(3), 357-366.

Doherty, J. (2016), PEST: Model Independent Parameter Estimation Part 1, edited, pp. 1 - 366, Watermark Numerical Computing.

Ettinger, T., and J. Brugman (1992), Brady Hot Springs geothermal power plant, *Geothermal Res. Council Bull*, *21*(8), 258-260.

Faulds, J. E., L. J. Garside, and R. Chaney (2003), *Preliminary geologic map of the Desert Peak-Brady geothermal fields, Churchill County, Nevada*, Nevada Bureau of Mines and Geology.

Faulds, J. E., I. Moeck, P. Drakos, and E. Zemach (2010a), Structural assessment and 3D geological modeling of the Brady's geothermal area, Churchill county (Nevada, USA): A preliminary report, paper presented at 35 th Workshop on Geothermal Reservoir Engineering, Stanford University, Stanford, California.

Faulds, J. E., M. Coolbaugh, V. Bouchot, I. Moek, and K. Oguz (2010b), Characterizing structural controls of geothermal reservoirs in the Great Basin, USA, and Western Turkey: Developing successful exploration strategies in extended terranes, paper presented at World Geothermal Congress 2010.

Faulds, J. E., M. F. Coolbaugh, D. Benoit, G. Oppliger, M. Perkins, I. Moeck, and P. Drakos (2010c), Structural controls of geothermal activity in the northern Hot Springs Mountains, western Nevada: The tale of three geothermal systems (Brady's, Desert Peak, and Desert Queen), *Geothermal Resources Council Transactions*, *34*, 675-683.

Feigl, K. L., and PoroTomo Team (2017), Overview and Preliminary Results from the PoroTomo project at Brady Hot Springs, Nevada: Poroelastic Tomography by Adjoint Inverse Modeling of Data from Seismology, Geodesy, and Hydrology, paper presented at Proceedings, 42nd Workshop on Geothermal Reservoir Engineering, Stanford University, Stanford, California.

Foxall, W. (2016), PoroTomo Subtask 3.1 Meq Relocations & 3D Velocity Models 30 June 2015, edited.

Franco, A., and M. Vaccaro (2014), Numerical simulation of geothermal reservoirs for the sustainable design of energy plants: a review, *Renewable and Sustainable Energy Reviews*, *30*, 987-1002.

Freifeld, B. M., S. Finsterle, T. C. Onstott, P. Toole, and L. M. Pratt (2008), Ground surface temperature reconstructions: Using in situ estimates for thermal conductivity acquired with a fiber-optic distributed thermal perturbation sensor, *Geophysical Research Letters*, *35*.

Gringarten, A., P. Witherspoon, and Y. Ohnishi (1975), Theory of heat extraction from fractured hot dry rock, *Journal of Geophysical Research*, *80*(8), 1120-1124.

Gro Harlem Brundtland, Mansour Khalid, Susanna Agnelli, Saleh Abdulrahman Al-Athel, Pablo Gonzalez Casanova, and L. M. Padika (1987), Our Common Future: Report of the World Commission on Environment and Development, Oxford.

GTO, D. (2016), 2015 Annual Report Geothermal Technologies Office, 30 pp, U.S. Department of Energy.

Haitjema, H. M. (1995), *Analytic element modeling of groundwater flow*, San Diego : Academic Press, [1995] ©1995.

Hibbeler, R. C. (2014), *Fluid Mechanics* 1st ed., 928 pp., Pearson Prentice Hall, New York.

Hurwitz, S., and M. Manga (2017), The Fascinating and Complex Dynamics of Geyser Eruptions, *Annual Review of Earth and Planetary Sciences*, *45*, 31-59.

Ikeda, N., K. Uogata, S. Kawazoe, and K. Haruguchi (2000), Delineation of fractured reservoir by transient temperature analysis using fiber optic sensor, paper presented at Proceedings World Geothermal Congress, May.

Jolie, E., I. Moeck, and J. E. Faulds (2015), Quantitative structural–geological exploration of fault-controlled geothermal systems—A case study from the Basin-and-Range Province, Nevada (USA), *Geothermics*, *54*, 54-67.

Krieger, Z., and E. Sponsler (2002), Improvement to the Brady geothermal project to compensate for decline in resource performance, *TRANSACTIONS-GEOTHERMAL RESOURCES COUNCIL*, 735-738.

Laboso, R. C., and N. C. Davatzes (2016), Fault-Controlled Damage and Permeability at the Brady Geothermal System, Nevada, USA, paper presented at Proceedings of the 41st Workshop on Geothermal Reservoir Engineering, Stanford, California.

Leaf, A. T., D. J. Hart, and J. M. Bahr (2012), Active thermal tracer tests for improved hydrostratigraphic characterization, *Ground Water*, *50*, 726-735.

Li, T., S. Shiozawa, and M. W. McClure (2016), Thermal breakthrough calculations to optimize design of a multiple-stage Enhanced Geothermal System, *Geothermics*, *64*, 455-465.

Lovekin, J. (2000), The economics of sustainable geothermal development, *TRANSACTIONS-GEOTHERMAL RESOURCES COUNCIL*, 113-118.

Miller, D. E., et al. (2018), DAS and DTS at Brady Hot Springs: Observations about Coupling and Coupled Interpretations, paper presented at Proceedings of the Forty-Third Workshop on Geothermal Reservoir Engineering, Stanford, California.

Patterson, J. R., M. Cardiff, T. Coleman, H. Wang, K. L. Feigl, J. Akerley, and P. Spielman (2017), Geothermal reservoir characterization using distributed temperature sensing at Brady Geothermal Field, Nevada, *The Leading Edge*, *36*(12), 1024a1021-1024a1027.

Read, T., V. Bense, O. Bour, T. Le Borgne, N. Lavenant, R. Hochreutener, and J. Selker, S (2015), Thermal-Plume fibre Optic Tracking (T-POT) test for flow velocity measurement in groundwater boreholes, *Geoscientific Instrumentation, Methods and Data Systems*, *4*, 161-175.

Read, T., O. Bour, V. Bense, T. Le Borgne, P. Goderniaux, M. Klepikova, R. Hochreutener, N. Lavenant, and V. Boschero (2013), Characterizing groundwater flow and heat transport in fractured rock using fiber-optic distributed temperature sensing, *Geophysical Research Letters*, *40*, 2055-2059.

Reinsch, T., and J. Henninges (2010), Temperature-dependent characterization of optical fibres for distributed temperature sensing in hot geothermal wells, *Measurement Science and Technology*, *21*(9), 094022.

Reinsch, T., J. Henninges, and R. Ásmundsson (2013), Thermal, mechanical and chemical influences on the performance of optical fibres for distributed temperature sensing in a hot geothermal well, *Environmental earth sciences*, *70*(8), 3465-3480.

Robertson, E. C. (1988), Thermal properties of rocks*Rep. 88-441*, 106 pp, US Geological Survey.

Rybach, L., and M. Mongillo (2006), Geothermal sustainability-a review with identified research needs, *GRC Transactions*, *30*, 1083-1090.

Sakaguchi, K., and N. Matsushima (2000), Temperature logging by the distributed temperature sensing technique during injection tests, paper presented at Proceedings World Geothermal Congress, May.

Sellwood, S. M., D. J. Hart, and J. M. Bahr (2015), An in-well heat-tracer-test method for evaluating borehole flow conditions, *Hydrogeology Journal*, *23*, 1817-1830.

Siler, D. L., N. H. Hinz, J. E. Faulds, and J. Queen (2016), 3D analysis of geothermal fluid flow favorability; Bradys, Nevada, USA, paper presented at Proceedings, forty-first workshop on geothermal reservoir engineering. Stanford: Stanford University.

Theis, C. V. (1935), The relation between the lowering of the Piezometric surface and the rate and duration of discharge of a well using ground-water storage, *Eos, Transactions American Geophysical Union*, *16*(2), 519-524.

Zarrouk, S. J., and H. Moon (2014), Efficiency of geothermal power plants: A worldwide review, *Geothermics*, *51*, 142-153.

APPENDIX A

LIST OF ACCOMPANYING MATERIAL ON DVD

A.1 – Thermal Characterization

Read me file describing contents
Collected borehole DTS temperature in .mat format
Heat transfer code with necessary supporting functions in .m format

A.2 – Hydraulic Characterization

Read me file describing contents
Siler lithology identifiers and lithology grouping for porous media models
Groundwater flow models described in thesis in .gwv format
MODFLOW cell center locations in PoroTomo coordinate system in .csv format
Well coordinates in .csv format
Observation well pressure data
Fault location files in [UTM X, UTM-Y, Z] format
Earth lithology coordinates from Siler geologic model in [UTM X, UTM Y, Z] format
Matlab script to generate conceptual models

A.3 – Geothermal Sustainability

Read me file describing contents
Power production model and necessary supporting functions

PDF copy of thesis

DVD is available in C.K. Leith Library of Geology and Geophysics